# INVESTIGATION OF GLACIAL DYNAMICS IN LAMBERT GLACIAL BASIN

# USING SATELLITE REMOTE SENSING TECHNIQUES

A Dissertation

by

JAEHYUNG YU

Submitted to the Office of Graduate Studies of
Texas A&M University
in partial fulfillment of the requirements for the degree of

DOCTOR OF PHILOSOPHY

December 2005

Major Subject: Geography

# INVESTIGATION OF GLACIAL DYNAMICS IN LAMBERT GLACIAL BASIN

# USING SATELLITE REMOTE SENSING TECHNIQUES

A Dissertation

by

JAEHYUNG YU

Submitted to the Office of Graduate Studies of
Texas A&M University
in partial fulfillment of the requirements for the degree of

DOCTOR OF PHILOSOPHY

Approved by:

| | |
|---|---|
| Chair of Committee, | Hongxing Liu |
| Committee Members, | Andrew G. Klein |
| | Vatche P. Tchakerian |
| | Mahlon Kennicutt |
| Head of Department, | Douglas Sherman |

December 2005

Major Subject: Geography

# ABSTRACT

Investigation of Glacial Dynamics in Lambert Glacial Basin Using

Satellite Remote Sensing Techniques.

Jaehyung Yu, B.S., Chungnam National University;

M.S., Chungnam National University

Chair of Advisory Committee: Dr. Hongxing Liu

The Antarctic ice sheet mass budget is a very important factor for global sea level. An understanding of the glacial dynamics of the Antarctic ice sheet are essential for mass budget estimation. Utilizing a surface velocity field derived from Radarsat three-pass SAR interferometry, this study has investigated the strain rate, grounding line, balance velocity, and the mass balance of the entire Lambert Glacier – Amery Ice Shelf system, East Antarctica.

The surface velocity increases abruptly from 350 m/year to 800 m/year at the main grounding line. It decreases as the main ice stream is floating, and increases to 1200 to 1500 m/year in the ice shelf front. The strain rate distribution defines the shear margins of ice flows. The major ice streams and their confluence area experience the most severe ice deformation. The width of the shear margin decreases as it flows downstream except for the convergent areas with tributary glaciers. The grounding line for the main ice stream and the boundary of Amery Ice Shelf and surrounding tributary glaciers is delineated.

The total basal melting is estimated to be 87.82 ± 3.78 Gt/year for the entire Amery Ice Shelf. Compared with the ice flux (16.35 ± 3.11 Gt/year) at the ice shelf front, basal melting is apparently the dominant discharging process of the system. The melting rate for the Amery Ice Shelf decreases rapidly from the grounding zone (21.64 ± 2.17 m/year) to the ice shelf front (-0.95 ± 0.14 m/year).

The Lambert Glacial Basin contributes the total ice mass of 95.64 ± 2.89 Gt/year to the ocean, which is equivalent to increasing the global sea level by 0.24 mm/year. Considering 90.54 ± 1.55 Gt/year of snow accumulation, the entire Lambert Glacier – Amery Ice Shelf system is slightly negatively imbalanced at -5.09 ± 3.46 Gt/year. Although the entire system is estimated to have a slight negative mass balance, three sub-glacial systems have a net positive mass balance due to a relatively high snow accumulation rate or relatively slow ice motion. Considering the large mass loss in West Antarctica, it is believed that the overall mass budget in Antarctica is negative based on this research.

# DEDICATION

I want to dedicate this dissertation to my parents. My parents, Mr. Hwang Yu and Ms. Inja Joo, have been the greatest supporters and believers in me. Their endless love has provided the safest shelter for me to take a rest. Their guidance has built my confidence to handle any difficulties. They have been and will be the greatest heroes and role models to me forever.

# ACKNOWLEDGMENTS

I would like to express my deepest appreciation to my advisor, Dr. Hongxing Liu. His efforts to make me a real researcher cannot be expressed in words. He has always provided immeasurable inspiration on this research. He sometimes has taught me like a tutor, and sometimes he has been the scariest critic of my research output. His guidance, expertise, insights and passion for research have strongly inspired this research. He also has shown how true research should be carried out through relentless efforts. Even the biggest obstacles in this research have been doable with him. He has motivated and encouraged me to get my confidence back when I had difficulties. I thank him so much for being my advisor.

I wish to express my sincere gratitude to my committee members. Dr. Vatche Tchakerian has been most helpful as a geomorphologist and as a mentor. He has always provided sincere advice whenever I had to make a decision. I feel privileged to have had him on my committee. Dr. Andrew Klein has provided enormously valuable comments and input in this study. His effort in the review of my dissertation has made it more valuable. He has taught me how a scholar should approach and solve problems. I deeply appreciate his help on this research. Dr. Malhorn Kennicutt has supplied a solid and respectable sounding board. He has provided important insights and perspectives in this research despite his busy schedule.

Special thanks are extended to my family in the Knowledge Engineering Lab. Dr. Robert Coulson has opened up the new world of GIS. His passion for research taught me the attitude of a scholar. His support has widened my specialties and helped me to

concentrate on this research without financial difficulties. Dr. Maria Tchakerian has been a supervisor and a good friend. Ms. Audrey Bunting has carefully helped me with financial matters.

I would also like to acknowledge my colleagues. I thank Lei Wang for being my best friend. Our sharing of knowledge, happiness, and worries has been a great help to me through this research. His gifted programming skills have helped me. Without his help, this research would have been more difficult and taken longer. Mathew Clemonds has provided valuable help on technical difficulties with software. Weiming Lin has always cheered me up when I was having difficulties. The fellowship of my friends has made my life enjoyable.

Finally, I want to thank my wonderful family. My lovely wife, Hyunsook Kim, has been the energy in my life since the first time I met her. Without her love, understanding, and support, I would not have been able to finish this dissertation. She has not only been a loving wife who is always there for me, but also she is my best friend who always kept me going. She is, and will be, the energy of my life and the greatest love in my heart. My sweetest daughter, Angeline Eunsoo Yu, has been the greatest joy of my life. All the stresses and the worries disappear with her smile. Watching her new accomplishments and growth have provided me with joy and happiness. I will dedicate my life to making her happy. My wife and my daughter mean everything to me. My family has been an inspiration, a foundation, and a rock. I love you.

**TABLE OF CONTENTS**

# LIST OF FIGURES

FIGURE                                                                                                          Page

# LIST OF TABLES

## CHAPTER I

## INTRODUCTION

### 1.1. Background

The global warming and sea level rise are critical issues to science communities as well as general public because of its possible consequence on everyday human life. Especially, the Antarctic ice sheet is extremely sensitive to both atmospheric and oceanic environmental changes. As an immense reservoir, it contains over 70% of Earth's fresh water. Of particular importance is the possibility of a significant rise in global sea level brought on by a change in the mass balance of the ice sheet under the influence of global warming, or by the surging and collapse of a major ice drainage basin (Mercer 1978, Bindschadler 1991, Rott *et al.* 1996).

Based on previous sea level change measurements, the Antarctic ice sheet contributed 0.0 to 0.5 mm/yr in sea level rise over the $20^{th}$ century (Intergovernmental Panel on Climate Change 2001). Melting all the ice contained in Antarctic ice sheets would raise sea level by 60 m (IPCC 2001). In the last 7 years, the picture of a slowly changing Antarctic ice sheet has radically altered. It is now realized that ice shelf basal melting may account for up to one third of the loss from the grounded ice; extensive, rapid thinning is occurring in one part of the West Antarctic ice sheet interior; and the collapse of the Antarctic Peninsula ice shelves is accelerating the discharge of grounded

_____

This dissertation follows the style of *International Journal of Remote Sensing*.

ice. These discoveries inject a new sense of urgency into gaining a better understanding of the evolution of the ice sheet (The International Council for Science committee on Antarctic Research 2002).

Recent advances in the determination of the mass balance of polar ice sheets show that the West Antarctic ice sheet is probably thinning overall with a loss of $-48\pm14$ $km^3$/year. The mass balance of West Antarctic ice sheet shows bimodal mass imbalance distribution with thickening in the east and thinning in the north (Rignot and Thomas 2002). In addition, new discoveries by satellite interferometry have shown that the ice previously thought to be accumulating in the interior of East Antarctica is likely to be small, but whether the interior is gaining or losing mass can not yet be determined with the value of $22\pm23$ $km^3$/year. Considering mass loss in West Antarctica, the overall mass budget in Antarctica is believed to be negative (Rignot and Thomas 2002).

The Lambert Glacier basin, located in East Antarctica, is the largest glacial basin in the world with a width of about 1300 km, a length of 1450 km, and an ice thickness up to 4000 m (Lythe *et al.* 2001) (Figure 1.1). Because of its size, the Lambert Glacial Basin plays a fundamental role in the glacial dynamics and mass budget of East Antarctica in response to present and future climate changes.

Pioneering work on the Lambert Glacial Basin was carried out by the Australian National Antarctic Research Expeditions (ANARE) during 1962-65 (Budd, 1966), 1968-71 (Budd *et al.* 1982), and 1989-95 (Higham *et al.* 1997). Based on the information collected by these expeditions, several research attempts have been made to assess the

dynamic behavior and total mass budget of the Lambert Glacial Basin (e.g. Budd 1966, Allison 1979, McIntyre 1985, Higham *et al.* 1997).

Due to logistical and technical difficulties in this remote region, ground-based measurements ice velocity, ice thickness and snow accumulation rates are sparse and mainly confined to transverse routes, with large portions of the interior region having no data collected. As a result, these previous analyses have been seriously limited. Early mass-budget estimates reported by Allison (1979) and McIntyre (1985) vary widely. Supporting evidence for surging has been offered for the Lambert Glacier-Amery Ice Shelf System (Allison 1979), but other investigators have argued against surging for this system (McIntyre 1985, Radok *et al.* 1987, Hambrey and Dowdeswell 1994).

Following successful completion of the RADARSAT-1 Antarctic Mapping Mission (AMM-1) from September to October, 1997 (Jezek 1998) and the Antarctic Mapping Mission 2 (AMM-2) from October to December, 2000 (Jezek 2002), 25 m resolution Radarsat-1 SAR data is available for the entire Lambert Glacial Basin. With a 24-day orbit cycle and 6 days of repeat-pass acquisitions a substantial volume of interferometric SAR (InSAR) data was acquired during these two missions. Interferometric synthetic aperture radar has now become a well-established means of collecting ice-velocity measurements with high resolution and high accuracy (Joughin *et al.* 2000).
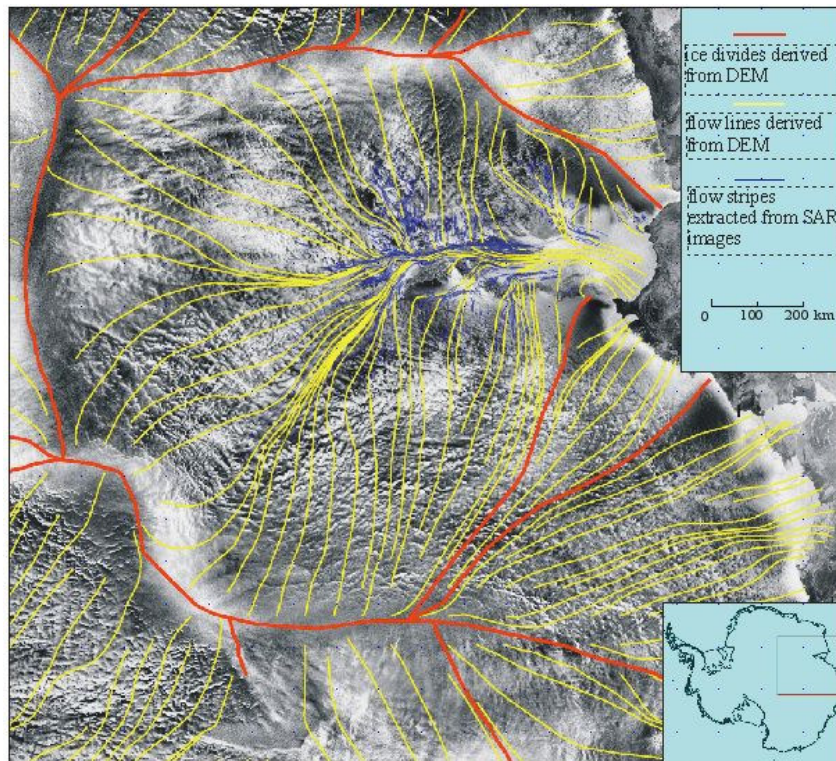
Figure 1.1 Ice divides and flow lines overlaid in SAR image mosaic of the Lambert Glacial Basin, Antarctica.

Using radar remote sensing techniques, there have been advanced studies of mass balance, ice velocity, and the grounding line of the Lambert Glacial Basin area (Wingham *et al.* 1998, Vaughan *et al.* 1999, Fricker *et al.* 2000, Gray *et al.* 2002, Rignot 2002, Young and Hyland 2002, Joughin 2002, Rignot and Thomas 2002). Those include mass balance studies using ERS-1 and ERS-2, and mass balance and ice velocity studies using RADARSAT-1.

Based on ERS-1 radar altimeter data and *in situ* velocity measurements at ground stations, Fricker *et al.* (2000) obtained positive balance fluxes for the upstream region of

Lambert Glacier-Amery Ice Shelf drainage system. Vaughan *et al.* (1999) derived a surface accumulation map for Antarctica at 10 km resolution. Wingham *et al.* (1998) also reported positive mass accumulation rate by calculating elevation change from 1992 to 1996 using ERS-1 and ERS-2 altimeter data.

By using SAR interferometry and speckle tracking, Rignot (2002) and Rignot and Thomas (2002) concluded substantial losses for the Lambert glacier. Ice velocity maps were created by a number of research groups for the portion of Lambert Glacial Basin and the Amery Ice Shelf for mass balance and strain rate calculation (Rignot 2002, Rignot and Thomas 2002, Joughin 2002, Young and Hyland 2002).

Rignot (2002) calculated the velocity at the grounding line and the mass balance for the part of the Lambert Glacial Basin using speckle tracking methods for the region. Joughin (2002) completed a two-dimensional ice velocity map using combined InSAR and speckle tracking. Fricker *et al.* (2000) calculated the mass balance of the Lambert Glacier-Amery Ice Shelf System with ERS radar altimeter DEM and in-situ surface velocity data using the balance flux concept. Young and Hyland (2002) derived the surface velocity and strain rates over the Amery Ice Shelf using the speckle tracking method.

However, these previous velocity and mass balance studies covered only portions of the Lambert Glacial Basin and had limited accuracy. With newly acquired InSAR pairs available in three pass interferometry, a higher accuracy velocity field can be extracted. The three pass SAR interferometry over the study area will result in ice dynamic analysis with higher accuracy including application of the mass balance, strain

rate, balance flux, and grounding line position. In terms of data quality, InSAR pairs from the newly processed ascending and descending orbits from AMM-2 will give the best possible improvement on the velocity measurements because the three pass interferometry can remove the topographic information using one pair of InSAR pair and the secondr pair can be used for calculating surface movement. The best topographic data available for previous studies was ERS radar altimetry data, which has significant limitations in steep and mountainous areas. The recent GLAS/ICESat laser altimetry data will be utilized for drainage basin delineation and ice divide extraction. In addition, the accurate height information can provide useful information for ice thickness calculations in addition to identification of floating ice.

As mentioned earlier, the mass balance of the Antarctic Ice Sheet plays important role in global sea level rise, and it is still unclear the mass balance of East Antarctica is gaining or losing the mass. The mass balance and glacier dynamics of the Lambert Glacial Basin is, therefore, very important in determining the mass balance of East Antarctica as well as global sea level contribution from Antarctic Ice Sheet since it can provide essential clue on the mass balance and sea level contribution of East Antarctica. It is expected that this study will to our knowledge of this glacier system in detailed structure of mass balance of the Lambert Glacial Basin and, eventually, in the impact of Antarctic Ice Sheet on global sea level rise.

## 1.2. Research scope and objectives

The study aims to provide the answers for the following questions:

- What is the mass balance status of the Lambert Glacial Basin?

- Does the mass balance of the Lambert Glacial Basin affect global sea level rise?

- What are the internal mass balance structure of the Lambert Glacial Basins and its contribution of sub-systems?

- What are the characteristics of glacial dynamics in the Lambert glacier system? To answer the research questions, the following tasks are carried out:

- Calculate the strain rate distribution over the entire Lambert Glacial Basin based on Radarsat InSAR velocity information.

- Delineate and refine the grounding line position of the Amery Ice Shelf by utilizing InSAR coherence images and the vertical velocity component from InSAR.

- Delineate the basin boundary and ice divides from InSAR derived ice motion direction information and direction information derived from OSU DEM and ICESat laser altimetry.

- Calculate the mass imbalance distribution over the glacial basin using balance velocity and ice depth averaged velocity from InSAR.

- Calculate the mass balance and ice discharges of all ice streams in the Lambert Glacier – Amery Ice Shelf system, and estimate basal melting along the Amery Ice Shelf from the grounding line to the ice shelf front.

- Derive the net mass balance field over the glacier basin to provide ice thickening and thinning information utilizing the newly derived ice velocity data in GIS environment.

These specific tasks will be the main components in explaining the current state of ice dynamics and mass balance of the Lambert Glacier-Amery Ice Shelf System.

**1.3. Lambert Glacier-Amery Ice Shelf System**

The Lambert Glacier-Amery Ice Shelf System is located between latitudes 67ºS and 75ºS and longitudes 68ºE and 75ºE, and is the largest glacier-ice shelf system in the world. The Lambert Glacier-Amery Ice Shelf System is defined as "the area where snow precipitates and ice are drained and discharged through the Amery Ice Shelf. The Lambert Glacier-Amery Ice Shelf System covers about 13 % of the grounded Antarctic ice sheet (Allison 1979), whereas the Amery Ice Shelf front comprises approximately 1.7% of the total Antarctic coastline (Giovinetto and Bently 1985). Therefore the Lambert Glacier-Amery Ice Shelf System is dynamic and important in mass balance and ice dynamics studies of the Antarctic ice sheet.

The Lambert Glacier-Amery Ice Shelf System consists of eight structurally defined ice streams (Hambrey and Dowdeswell 1994) (Figure 1.2). Flowing northward of the system, three major ice streams, the Lambert, Mellor, and Fisher Glaciers are flowing through the center of the system resulting in a confluence zone that becomes the main ice stream discharging to Amery Ice Shelf and is named Lambert Glacier (Figure 1.2). A number of other tributary ice streams join the main stream of Amery Ice Shelf from both the east and west; notably Charybdis Glacier, the tributary glacier from the Price Charles Mountains, and the tributary glacier from the northeast   Mawson Escarpment (Figure 1.2).
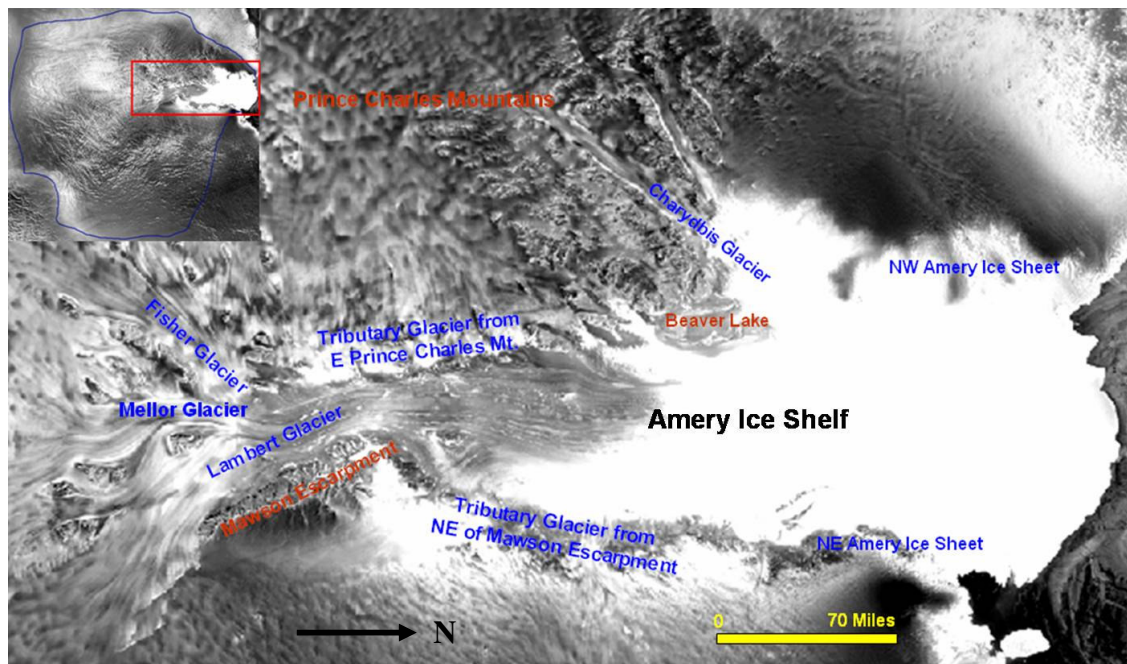
Figure 1.2 Major ice streams and land marks of the Lambert Glacier-Amery Ice Shelf system.

## 1.4. Organization of the research

The research background and objectives have been presented in the preceding sections. Chapter II begins with an overview of two-dimensional surface velocity extraction techniques, including SAR interferometry and speckle tracking. The theoretical background and the details of the processing components are then discussed. Then the two-dimensional surface velocity field extraction method, and the mosaic and calibration of the velocity fields is discussed. This is followed by a general description and discussion of the two-dimensional velocity field of Lambert Glacier Basin to explain its application in this study.

In chapter III, the grounding line delineation and location is examined. Principal methods to delineate the grounding line including InSAR coherence images and vertical velocities are discussed. Previous studies of grounding lines for the study area are summarized and the newly delineated grounding line and its location is discussed. The result of grounding line delineation is validated through comparison with previous studies as concluding this chapter.

Chapter IV examines the strain rate of main ice streams of the Lambert Glacier-Amery Ice Shelf System. This chapter begins with a brief description of previous studies of strain rates for the study area. The strain rate calculation method using x directional and y directional velocity fields from SAR interferometry is explained. The final section presents discussions on the newly created strain rate map.

Chapter V investigates the balance velocity and its application for determining the mass balance of the Lambert Glacier-Amery Ice Shelf System. Previous methods and the newly developed flow direction and flux distribution method are introduced. The balance velocity distribution and its comparison with previous methods are discussed. The chapter concluded with the mass imbalance distribution of grounded ice streams.

Chapter VI presents the basin scale glacial mass balance calculation methods and previous studies for Lambert Glacier Basin. The sub-basins are delineated using a Digital Elevation Model, ICESat laser altimetry data, and direction information from SAR interferometry. The basin and sub-basin scale mass balance of the Lambert Glacier-Amery Ice Shelf System is presented. Finally, basal melting of Amery Ice Shelf is discussed.  Then, the result comparison with a previous study is discussed. In addition,

the methodology and algorithm for GIS based net mass calculation is presented. The net mass balance distribution over the main ice streams of the Lambert Glacier-Amery Ice Shelf is discussed. This chapter concludes with discussions on ice thickening and thinning, and their relationship with surface features.

The final chapter summarizes the research findings and presents conclusions and implications derived from this study.

CHAPTER II

DERIVATION OF SURFACE VELOCITY FIELD

**2.1. Velocity measurement techniques**

Knowledge of ice flow velocity and strain rate is important in assessing ice mass balance and in understanding the flow dynamics of ice streams. The ice flow direction and magnitude are instrumental in the re-distribution of ice mass within the drainage basin. When ice thickness and accumulation rates are known, ice velocities can be used in a direct calculation of the mass balance or can be compared with balance velocities to assess the state of equilibrium of any ice mass (Paterson 1994).

Speckle tracking of repeat-pass complex radar images (Gray *et al.* 1998, Gray *et al.* 2001, Rignot 2002, Young and Hyland 2002), and SAR interferometry (Goldstein *et al.* 1993, Joughin *et al.* 1996, Kowk and Fahnestock 1996, Rignot 2002, Joughin 2002) have been proven to produce a reliable two-dimensional surface velocity field in for ice sheets. The analysis in this study relies primarily on a combination of speckle tracking and interferometric SAR techniques.

The Canadian Radarsat-1, launched on November 4, 1995, is equipped with a C-band Synthetic Aperture Radar (SAR) capable of acquiring high resolution (25 m) images of Earth's surface day or night and under all weather conditions. Because of its enhanced flexibility to collect data using a variety of swath widths, incidence angles and spatial resolutions, RADARSAT-1 can be maneuvered in orbit to rotate the normally right-looking SAR to a left-looking mode. This 'Antarctic Mode' provides means for the

first time of nearly instantaneous, high-resolution views of the entirety of Antarctica. The first Antarctic Mapping Mission (AMM-1) began on September 9, 1997 and was successfully concluded on October 20, 1997 to create the first, high resolution, radar image of the continent. The second, AMM-2 began on September 3, 2000 and was successfully concluded on November 17, 2000 to compare the data with AMM-1 and to obtain as much surface velocity data on the ice sheet as possible (Jezek 1998, Jezek 2002).

The AMM-1 and AMM-2 missions provided a wealth of data for InSAR based process of Antarctica. However, many of the problems with this InSAR data set relate to its 24 day repeat cycle which is a long period to make interferometric measurements of an ice sheet. Reasonable correlation levels can usually be obtained in low-accumulation areas. In many high-accumulation areas, interferometry over 24 days will often fail (Joughin 2002).

A 24 day repeat cycle provides a strong sensitivity to displacement, with one interferometric fringe roughly equivalent to 1 m a$^{-1}$ of horizontal ice motion perpendicular to the satellite track. This yields good accuracy in slow-moving areas, where the phase can successfully be unwrapped. In fast-moving areas, however, phase unwrapping is much more difficult, in many cases, no phase measurement can be made. Thus, with conventional 24 day interferometry, velocity estimation is largely limited to slow-moving areas. For the fast moving areas, speckle tracking takes advantage of the ability to determine with sub-pixel accuracy the displacements between scenes in an interferometric pair using the cross-correlation function of the speckle patterns, which

are sharply peaked. Because matches are based on speckle rather than visible features, speckle tracking, like conventional interferometry, is limited by temporal and other sources of decorrelation (Joughin 2002).

For the most of ice dynamics and mass balance analysis, this study mainly uses the surface velocity field created by Byrd Polar Research Center at Ohio State University from the AMM-2 three-pass InSAR data. As a co-project with the Ohio State University, this study acquired the most advanced and updated surface velocity data for the first time among the many institutions. In addition, this study developed a new algorithm for mosaic and calibration of the surface velocity information for neighboring InSAR frames.

This chapter briefly summarizes the SAR interferometry based surface velocity extraction methods. New techniques for mosaicing and calibration of the surface velocity information for neighboring frames or orbits is introduced. The two dimensional surface velocity field of Lambert glacier – Amery Ice Shelf system from the Ohio State University is discussed and its application for this study concludes this chapter.

## 2.2. SAR interferometry

The repeat-pass interferometric SAR data consists of two or more complex radar images for the same scene acquired by a SAR sensor in a precise repeat orbit. The scene is imaged from almost the same geometry, but with slightly different positions and aspect angles during different passes of the spacecraft. The phase unwrapping method and speckle tracking method represents two different schemes to measure surface

displacements based on the repeat-pass InSAR data. Along with the known time span of the repeat cycle, the derived surface displacements can be converted to the measurements for surface motion speed and direction.

The phase unwrapping method measures the phase differences between the complex radar images. If the ground is not seriously disturbed between passes, two complex radar images can be correlated to form an interferogram. The phase measured from the interferogram includes contributions from both the topography effect and the surface motion effect. Using a digital elevation model, the topography-induced phase can be removed, resulting in fringe patterns solely due to surface motion. When more than two passes of SAR data are available, differential interferometry can be used to separate the surface motion component from the topography component by a double difference technique (Kwok and Fahnestock 1996, Joughin *et al.* 1996a). After performing the phase unwrapping operation, the absolute phase measurements can be converted to surface displacements in the radar line-of-sight (LOS) direction. The accuracy of the resulting displacement measurement at each pixel is highly accurate, at a fraction of the radar signal c-band wavelength. Under the assumption that the ice flow vector is parallel to the ice surface, the radial LOS velocity can be projected into horizontal surface velocities with an estimate of the flow direction from a digital elevation model (DEM) (Kwok and Fahnestock 1997). With two InSAR pairs respectively from ascending and descending passes, three-dimensional surface displacements can be solved at an improved accuracy without using the surface parallel

flow assumption (Kwok and Fahnestock, 1996, Joughin *et al.* 1998, Mohr *et al.* 1998, Joughin 2002, Gray *et al.* 2005).

For one interferometric SAR pair, the surface motion induced phase component ($\Phi_m$) in the LOS direction can be expressed as (Zhao 2001):

$$\Phi_m = \Phi - \Phi_0 \qquad\qquad (2.1)$$

where $\Phi$ is the unwrapped phase after the removal of the topography effect, and $\Phi_0$ is an unknown constant phase, which is caused by the arbitrary selection of an initial start point for phase unwrapping. The surface motion velocity ($V_r$) in the range (cross-track) direction can be calculated by Equation (2):

$$V_r = \frac{\lambda}{4\pi T \sin(\beta + \alpha_r)}\Phi_m = \frac{\lambda}{4\pi T \sin(\beta + \alpha_r)}(\Phi - \Phi_0) \qquad (2.2)$$

where $\lambda$ is the wavelength of radar signal, $T$ is the time interval between acquisitions, $\beta$ is the incidence angle, and $\alpha_r$ is the surface slope angle in the range (cross-track) direction. The geometry parameters of interferometry are illustrated in Figure 2.1.
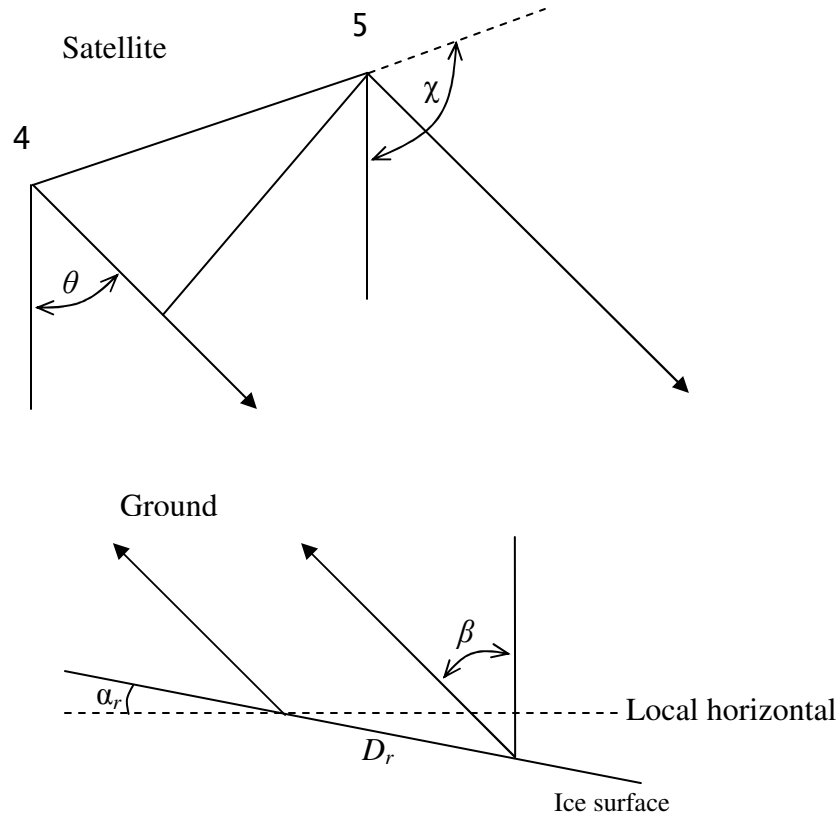
Figure 2.1 Geometry configuration of repeat-pass interferometry and terrain surface.

## 2.3. Speckle tracking

The speckle tracking method measures surface displacements by correlating and tracking the image speckle patterns between two repeat-pass acquisitions (Gray et al. 1998). A correlation matching algorithm is commonly used to obtain both azimuth (along-track) and range (across-track) direction offsets based on the coherent speckle pattern of small chips of the InSAR image pair. The cross-correlation can be performed using the real-valued amplitude images or the complex-valued radar images (Gray *et al.* 2001, Young

and Hyland 2002, Joughin 2002). For low-correlation regions, the cross-correlation surface from the complex-valued radar images is more strongly peaked, and hence more accurate matches can be achieved with a relatively small chip size. In regions with shear or steep topography, however, large phase gradients across the image chips often fail the match by reducing or eliminating the correlation peak. In such regions, the cross-correlation based on the amplitude radar images is unaffected by the phase gradients and can generate reliable offset estimates. Through oversampling of the correlation surface, the matching peak can be determined to a small fraction of a pixel spacing, resulting in accurate estimates of the surface displacements. It should be noted that the speckle tracking method does not depend on visible features in the images and is normally much more accurate than the feature retracking method, which depends on visible and identifiable features. The topography induced range offset component can be removed by using a digital elevation model. The range offset ($\delta_r$) after the removal of topography effect and azimuth offset ($\delta_a$) includes a non-motion component contributed by the imaging geometry (parallel baseline and orbit squint angle). The non-motion term in the range and azimuth offsets can be modeled using a linear model. The actual surface displacements in the range and azimuth direction can be computed by removing the modeled non-motion term as (Zhao 2001, Joughin 2002):

$$d_r = \delta_r - (a_0 + a_1 x + a_2 y) \tag{2.3}$$

$$d_a = \delta_a - (b_0 + b_1 x + b_2 y) \tag{2.4}$$

where $d_r$ and $d_a$ are respectively the surface displacements in the range and azimuth directions measured in pixel, $x$ and $y$ are the range and azimuth coordinates of the slant

range image, $a_0$, $a_1$, and $a_2$ are coefficients of the linear model, which account for the

non-motion term in range direction, and, $b_0$, $b_1$, and $b_2$ are coefficients of the linear

model, which account for the non-motion term in azimuth direction. Parameters $a_0$ and

$b_0$, are related to the parallel baseline, $a_1$ and $b_1$, are related to the orbit squint angle, and

$a_2$ and $b_2$, are related to the change of the orbit squint angle along the flight line. The

velocity components in the range ($V_r$) and azimuth ($V_a$) directions can be calculated from

the equations below:

$$V_r = \frac{d_r - B\cos(\chi - \theta)}{T\sin(\beta + \alpha_r)} \cdot S_r \qquad (2.5)$$

$$V_a = \frac{d_a}{T\cos(\alpha_a)} \cdot S_a \qquad (2.6)$$

where $B$ is the length of the base line, $\chi$ is the baseline angle, $\beta$ is the local incidence

angle, $\theta$ is the radar look angle, $\alpha_r$ and $\alpha_a$ are terrain slopes respectively in the range and

azimuth directions, $S_r$ and $S_a$ are pixel sizes respectively in range and azimuth directions,

and $T$ is the time interval between two image acquisitions. The definitions of the above

geometric parameters are illustrated in Figure 2.1. Since range pixel size is larger than

azimuth pixel size for a slant range SAR image and the range motion estimates are

affected by the baseline and topography, the range velocity estimates from the speckle

tracking method are much less accurate than the azimuth velocity estimates.

The two-dimensional horizontal velocity field ($\vec{V}$) can be expressed as:

$$\vec{V} = V_r\vec{r} + V_a\vec{a} \qquad (2.7)$$

where $V_r$ and $V_a$ are the magnitudes of the surface motion speed in the range and azimuth directions, and $\bar{r}$ and $\bar{a}$ are unit vectors in the range and azimuth directions. The surface motion speed (*s*) and direction ($\psi$) can be calculated by the following equations:

$$s = \sqrt{V_r{}^2 + V_a{}^2} \qquad\qquad (2.8)$$

$$\psi = \arctan\left(\frac{V_a}{V_r}\right) \qquad\qquad (2.9)$$

**2.4. Two dimensional surface velocity field**

The phase unwrapping method and speckle tracking method have their advantages and disadvantages (Joughin *et al.* 1999b, Gray *et al.* 2001, Zhao 2001, Joughin 2002). In fact, they are complementary each other. With one interferometric SAR image pair, the speckle tracking method can derive two-dimensional surface displacements in both range and azimuth directions, in contrast to the range-only displacement measurement of the phase unwrapping method. For the speckle tracking method, the accuracy requirements for orbit and topographic data are not as stringent as for phase unwrapping method.

In fast-moving areas, the high fringe rate of the interferogram may make the phase unwrapping impossible, or the interferogram may be unwrapped into several small and disconnected regions due to the patchy coherence. Since the speckle tracking method is less sensitive to decorrelation and does not require phase unwrapping, it is able to provide displacement measurements farther into the shear margins and across

areas with a higher strain rate. In comparison, the primary advantages of the speckle tracking method lie in its ability to estimate surface motion speed and direction with one interferometric data pair and its suitability in areas of high ice velocity and long orbit repeat cycles. The major disadvantage of the speckle tracking method is that its range direction displacement measurements have intrinsically lower resolution and inferior accuracy, compared with the differential phase-based measurements of the phase unwrapping method.

To make full use of the comparative advantages of both methods, the range motion component derived by the phase unwrapping method and the azimuth motion component derived by the speckle tracking method should be combined whenever possible (Gray *et al.* 2001, Zhao 2001, Joughin 2002). Coupling the speckle tracking method with the phase unwrapping method creates the two-dimensional horizontal surface velocity field with the best possible accuracy. When no differential phase measurements can be made, for instance, in the case of fast-moving areas or the InSAR data pair with a long temporal baseline, the speckle tracking method is the only possible approach to obtain the measurements of both the range and azimuth motion components.

## 2.5. Velocity mosaic and calibration

An InSAR image frame acquired by ERS-1, ERS-2 or Radarsat-1 SAR sensor normally covers a ground area of 100 km by 100 km. Many applications require surface velocity data over a wider area. Multiple InSAR image frames from the same or adjacent orbits are required to achieve a full coverage. Conventionally, InSAR image data were

processed separately frame by frame. As a consequence of independent processing, velocity measurements obtained from one InSAR image frame are generally different from those obtained from other adjacent InSAR frames for the overlapping region. When the velocity data derived from individual image frames are merged, inconsistency and discontinuity in the surface motion speed and direction between neighboring frames are bound to occur. In addition, no matter whether the phase unwrapping method or speckle tracking method is used, velocity control points are required to calibrate the relative surface displacements from the InSAR data to absolute velocity estimates. Commonly, rock outcrops are conveniently selected as zero velocity control points for this purpose. Such velocity control points may not be identified for some InSAR image frames, which preclude the derivation of absolute velocity information.

This study presents a simultaneous least-squares adjustment method for calibrating and merging surface motion measurements obtained from multiple InSAR image frames. Based on a limited number of velocity control points and a set of velocity tie points, this method simultaneously calibrates model parameters and determines surface displacement measurements for all frames in a strip or a block. With this method, the velocity discrepancies between adjacent image frames are minimized, and a seamless velocity mosaic can be produced. In addition, this method greatly relaxes the velocity control point requirements. For those frames devoid of velocity control points, absolute velocity measurements can still be derived by utilizing distant velocity control points in other image frames or by utilizing the flow direction constraints imposed by surface flow stripes.

**2.5.1. Mathematical formulation of observation equations**

The first step in a least-squares strip or block adjustment is to identify the underlying observation equations, along with the minimum number of constraints (control points) necessary to solve for the adjustment problem. In the simultaneous least-squares adjustment, this study incorporates the following types of constraints: velocity control points, flow direction control points, and velocity tie points. The goal of the simultaneous least-squares adjustment is to reduce the number of required control points to a minimum and to produce a consistent and seamless velocity mosaic within a strip or a block. This study derives and presents mathematical observation equations in two different cases, which are referred to as case 1 and case 2 in the following sections. In case 1, the speckle tracking method alone is used to derive both range and azimuth displacements for the two-dimensional velocity field. Case 1 fits situations where the surface motion is fast and/or the interferometric SAR pair has a long temporal baseline. In case 2, the range displacements derived from the phase unwrapping method are combined with the azimuth displacements derived from the speckle tracking method to calculate the two-dimensional velocity field. As discussed above, case 2 is suiTable for the slow moving areas.

**2.5.1.1. Observation equations for velocity control points**

In case1, surface velocity extraction using speckle tracking method, Equations (2.3) and (2.4) are used to calculate range and azimuth displacements. Six unknown parameters need to be determined, including $a_0,\ a_1,\ a_2.\ b_0,\ b_1,\ and\ b_2$. In case2, Equation (2.1) is

used to calculate range displacements while Equation (2.4) is still used to calculate azimuth displacements. There are four unknown parameters in Equations (2.1) and (2.4), including $\Phi_0$, $b_0$, $b_1$, and $b_2$ Once the four parameters are determined, the two-dimensional surface displacements can be calculated.

Velocity control points play an important role in calibrating the unknown parameters. A velocity control point is a feature with a known position and velocity. Namely, its range and azimuth coordinates and its surface displacements in both range and azimuth directions ($D_r$, $D_a$) during the orbit repeat cycle are known. For case 1, observation equations for a velocity control point can be derived from Equations (2.3) and (2.4) as:

$$a_0 + a_1 x + a_2 y = \delta_r - D_r \qquad (2.10)$$

$$b_0 + b_1 x + b_2 y = \delta_a - D_a \qquad (2.11)$$

For case 2, the azimuth observation equation for the velocity control point is the same as equation (2.11), and the range observation equation can be derived from Equation (2.1) as:

$$\Phi_0 = \Phi - \frac{4\pi D_r}{\lambda} \qquad (2.12)$$

In practice, features at rock outcrops are often selected as stationary velocity control points, and their surface displacements are set to zero, namely, $D_r=0$ and $D_a=0$. Non-stationary velocity control points can be acquired through *in situ* GPS measurements, but they are often unavailable. Each stationary or non-stationary velocity control point gives rise to two observation equations. The accurate determination of the

unknown parameters requires a least-squares calibration with redundant observations. In case 1, a minimum of 4 non-collinear velocity control points are required to calibrate the six unknown parameters $a_0$, $a_1$, $a_2$. $b_0$, $b_1$, and $b_2$ in observation equations (2.10) and (2.11). In case 2, at least 3 non-collinear velocity control points are required to calibrate the four unknown parameters $\Phi_0$, $b_0$, $b_1$, and $b_2$ in observation equations (2.11) and (2.12). The quality, number, and spatial distribution of the velocity control points influence the estimates of the unknown parameters and hence the accuracy of the surface displacements. If the velocity control points are well distributed in both the range and azimuth directions, the least-squares solution for the parameters would be more stable and reliable. A larger number of velocity control points can reduce the propagation of errors in the velocity control points.

### 2.5.1.2. Observation equations for flow direction control points

In some cases, no sufficient number of stationary or non-stationary velocity control points can be identified for the least-squares calibration of the unknown parameters. But, it may be possible to determine the ice flow direction at many locations using ice flow stripes visible on the SAR images. In this paper, the definition of velocity control points is extended by including the flow direction control points. A flow direction control point is a location whose flow direction angle ($\psi$) is known, but no information is available for the magnitude of flow speed. The flow direction control point defines a ratio of range motion and azimuth motion by the equation below:

$$\frac{V_a}{V_r} = \tan \psi \qquad\qquad (2.13)$$

where $V_r$ and $V_a$ are range and azimuth direction velocity components, and $\psi$ is the flow

directional angle.
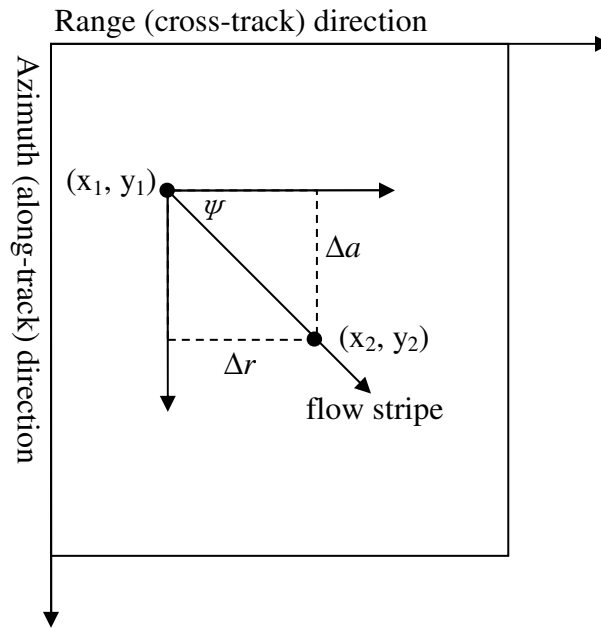


Figure 2.2 Acquisition of a flow direction control point based on an ice flow stripe.

A flow direction control point can be acquired by directly measuring the

orientation angle ($\psi$) of a flow stripe on a SAR image. Nevertheless, it is more

convenient and efficient in practice to measure the range and azimuth coordinates of the

end points $(x_1, y_1)$ and $(x_2, y_2)$ for a short straight segment along a flow stripe in the slant

range SAR image (Figure 2.2). By differencing the range and azimuth coordinates of the

27

two end points, we can obtain the range and azimuth offsets (Δr, Δa) along the flow stripe, which virtually define the flow directional angle.

For case 1, the measured range and azimuth offsets along a flow stripe can be expressed as:

$$k\Delta r = \delta_r - a_0 - a_1 x - a_2 y \qquad (2.14)$$

$$k\Delta a = \delta_a - b_0 - b_1 x - b_2 y \qquad (2.15)$$

where $k$ is a constant scaling factor, other parameters are the same as those in Equations (2.10) and (2.11). By dividing Equation (2.15) by Equation (2.14), we can cancel the scaling factor $k$ and obtain the following observation equation for a flow direction control point:

$$a_0 + a_1 x + a_2 y - \frac{\Delta a}{\Delta r}(b_0 + b_1 x + b_2 y) = \delta_a - \frac{\Delta a}{\Delta r}\delta_r \qquad (2.16)$$

For case 2, Equation (2.14) is replaced by the following equation:

$$k\Delta r = \frac{\lambda}{4\pi S_r}(\Phi - \Phi_0) \qquad (2.17)$$

By dividing Equation (2.15) by Equation (2.17), we can cancel the scaling factor $k$ and obtain the following observation equation for case 2:

$$\frac{\lambda\Delta a}{4\pi\Delta r}\Phi_0 - b_0 - b_1 x - b_2 y = \frac{\lambda\Delta a}{4\pi\Delta r}\Phi - \delta_a \qquad (2.18)$$

Compared with stationary and non-stationary velocity control points, flow direction control points impose relatively weaker constraints on the least-squares adjustment. Each flow direction control point can only provide one observation equation. In case 1, there are six unknown parameters in observation equation (2.16),

including $a_0$, $a_1$, $a_2$. $b_0$, $b_1$, and $b_2$. At least 7 non-parallel flow direction control points are required for the least-squares solution. In case 2, there are four unknowns in observation equation (2.18), including $\Phi_0$, $b_0$, $b_1$, and $b_2$. A minimum of 5 non-parallel flow direction control points are required for the least-squares solution for the unknown parameters. For the areas where no rock exposures can be found or no *in situ* velocity measurements are available, the flow stripes visible on SAR images can be used as flow direction control points to form observation equations for the least-squares adjustment. However, caution should be exercised when using flow stripes as direction controls. Although in most cases visible flow stripes indicate the present ice flow directions, they might be relic and hence do not represent current ice flow patterns in some rare situations (Casassa and Brecher 1993).

**2.5.1.3. Observation equations for tie points and simultaneous adjustment of multiple frames**

To obtain a full coverage of velocity measurements for a large area, multiple frames of interferometric SAR data sets from the same or adjacent orbits need to be processed. If interferometric data frames are processed independently, at least 4 non-collinear velocity control points or 7 non-parallel flow direction control points are required for each frame in case 1, and at least 3 non-collinear velocity control points or 5 non-parallel flow direction control points are required for each frame in case 2. If both velocity control points and flow direction control points are available, they can be combined to form the minimum number of observation equations required to calibrate the unknown parameters

for each frame. However, absolute velocity measurements cannot be derived for those frames where the number of available control points is fewer than the required minimum. The other serious problem is that, even with an adequate number of control points for each frame, velocity measurements calculated from neighboring frames often are different for overlapping areas. This is because the accuracy and spatial arrangement of control points vary from frame to frame. To eliminate velocity discontinuities and to relax the need for a certain number of control points for each frame, this study uses velocity tie points to stitch individual interferometric SAR frames together within a strip or a block. Instead of an independent least-squares calibration for a single interferometric SAR image frame at a time, this method simultaneously computes unknown parameters for all image frames in a strip or a block by linking individual image frames through tie points.

A tie point refers to the same ground feature that can be recognized in two overlapping images. For a tie point, its velocity can be derived from two different images. Logically, the velocity measurement for a tie point derived from one image frame should be exactly the same as that from the other image. This condition is used as a constraint to derive the observation equations for the tie points.
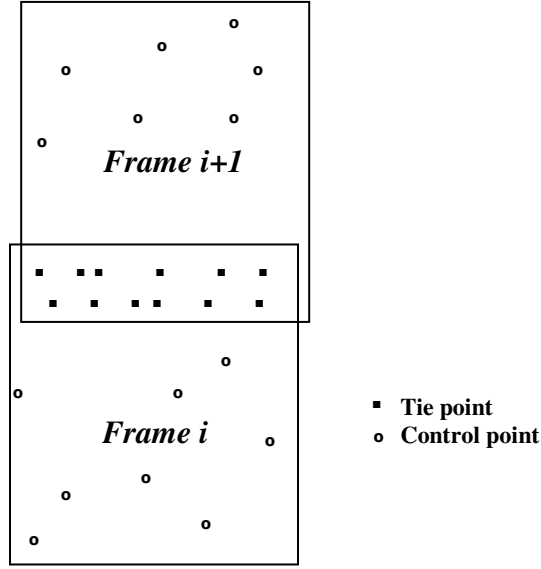
Figure 2.3 Strip adjustment of two consecutive frames with velocity control points and tie points.

As shown in Figure 2.3, tie points are located in the overlap area between two adjacent images $i$ and $i+1$. In case 1, we can write two equations for calculating the range and azimuth surface displacements of a tie point based on the first image frame ($i$) as follows:

$$d_r = \delta_r^i - (a_0^i + a_1^i x^i + a_2^i y^i) \tag{2.19}$$

$$d_a = \delta_a^i - (b_0^i + b_1^i x^i + b_2^i y^i) \tag{2.20}$$

where $x^i$ and $y^i$ are range and azimuth coordinates of the image frame $i$, $\delta_r^i$ and $\delta_a^i$ are the measured range and azimuth offsets of the tie point from the image frame $i$, and $a_0^i$, $a_1^i$, $a_2^i$, $b_0^i$, $b_1^i$, and $b_2^i$ are six unknown parameters for the image frame $i$.

Similarly, we can write two equations for the tie point based on the second image frame $(i+1)$ as follows:

$$d_r = \delta_r^{i+1} - (a_0^{i+1} + a_1^{i+1} x^{i+1} + a_2^{i+1} y^{i+1}) \qquad (2.21)$$

$$d_a = \delta_a^{i+1} - (b_0^{i+1} + b_1^{i+1} x^{i+1} + b_2^{i+1} y^{i+1}) \qquad (2.22)$$

where $x^{i+1}$ and $y^{i+1}$ are range and azimuth coordinates of the image frame $i+1$, $\delta_r^{i+1}$ and $\delta_a^{i+1}$ are the measured range and azimuth offsets of the tie point from the image frame $i+1$, and $a_0^{i+1}$, $a_1^{i+1}$, $a_2^{i+1}$, $b_0^{i+1}$, $b_1^{i+1}$, and $b_2^{i+1}$ are six unknown parameters for the image frame $i+1$.

By subtracting equation (2.21) from equation (2.19) and equation (2.22) from equation (2.20), we obtain two observation equations for a tie point in case 1:

$$a_0^i + a_1^i x^i + a_2^i y^i - a_0^{i+1} - a_1^{i+1} x^{i+1} - a_2^{i+1} y^{i+1} = \delta_r^i - \delta_r^{i+1} \qquad (2.23)$$

$$b_0^i + b_1^i x^i + b_2^i y^i - b_0^{i+1} - b_1^{i+1} x^{i+1} - b_2^{i+1} y^{i+1} = \delta_a^i - \delta_a^{i+1} \qquad (2.24)$$

In case 2, the azimuth observation equation for a tie point is the same as equation (24). Following Equation (1), we can write two equations to calculate the phase respectively from image frame $i$ and frame $i+1$ as:

$$\Phi_m = \Phi^i - \Phi_0^i \qquad (2.25)$$

$$\Phi_m = \Phi^{i+1} - \Phi_0^{i+1} \qquad (2.26)$$

where $\Phi^i$, $\Phi^{i+1}$ are the measured phases from image frame $i$ and image frame $i+1$, $\Phi_0^i$ and $\Phi_0^{i+1}$ are the unknown parameters respectively for image frame $i$ and image frame

*i+1*. Subtracting Equation (26) from Equation (25), we obtain the range observation equation for a tie point in case 2:

$$\Phi_0^i - \Phi_0^{i+1} = \Phi^i - \Phi^{i+1} \tag{2.27}$$

Observation equations for velocity control points, flow direction control points, and velocity tie points within a strip or a block can be integrated to perform a unified least-squares calibration of unknown parameters for all image frames. Assume that we have *n* velocity control points and *m* flow direction control points for image frame *i*, *p* velocity control points for image frame *i+1*, and *q* velocity tie points between image frame *i* and image frame *i+1*. Observation equations for a mixture of different types of control points and tie points can be written in a matrix format for case 1 as equation 2.28. Similarly, we can write the observation equations in matrix format for case 2 as equation 2.29.

$$
\begin{bmatrix}
1 & x_1^i & y_1^i & 0 & 0 & 0 & 0 & 0 & 0 & 0 & 0 & 0 \\
0 & 0 & 0 & 1 & x_1^i & y_1^i & 0 & 0 & 0 & 0 & 0 & 0 \\
. & & & . & & . & . & . & . & & & . \\
1 & x_n^i & y_n^i & 0 & 0 & 0 & 0 & 0 & 0 & 0 & 0 & 0 \\
0 & 0 & 0 & 1 & x_n^i & y_n^i & 0 & 0 & 0 & 0 & 0 & 0 \\
1 & 1 & 1 & -\dfrac{\Delta a_{n+1}^i}{\Delta r_{n+1}^i} & -\dfrac{\Delta a_{n+1}^i}{\Delta r_{n+1}^i}x_{n+1}^i & -\dfrac{\Delta a_{n+1}^i}{\Delta r_{n+1}^i}y_{n+1}^i & 0 & 0 & 0 & 0 & 0 & 0 \\
. & & . & & . & & . & . & . & & & . \\
1 & 1 & 1 & -\dfrac{\Delta a_{n+m}^i}{\Delta r_{n+m}^i} & -\dfrac{\Delta a_{n+m}^i}{\Delta r_{n+m}^i}x_{n+m}^i & -\dfrac{\Delta a_{n+m}^i}{\Delta r_{n+m}^i}y_{n+m}^i & 0 & 0 & 0 & 0 & 0 & 0 \\
0 & 0 & 0 & 0 & 0 & 0 & 1 & x_{n+m+1}^{i+1} & y_{n+m+1}^{i+1} & 0 & 0 & 0 \\
0 & 0 & 0 & 0 & 0 & 0 & 0 & 0 & 0 & 1 & x_{n+m+1}^{i+1} & y_{m+n+1}^{i+1} \\
. & & . & & . & & . & . & . & & & . \\
0 & 0 & 0 & 0 & 0 & 0 & 1 & x_{n+m+p}^{i+1} & y_{n+m+p}^{i+1} & 0 & 0 & 0 \\
0 & 0 & 0 & 0 & 0 & 0 & 0 & 0 & 0 & 1 & x_{n+m+p}^{i+1} & y_{n+m+p}^{i+1} \\
1 & x_{n+m+p+1}^i & y_{n+m+p+1}^i & 0 & 0 & 0 & -1 & -x_{n+m+p+1}^{i+1} & -y_{n+m+p+1}^{i+1} & 0 & 0 & 0 \\
0 & 0 & 0 & 1 & x_{n+m+p+1}^i & y_{n+m+p+1}^i & 0 & 0 & 0 & -1 & -x_{n+m+p+1}^{i+1} & -y_{n+m+p+1}^{i+1} \\
. & & . & & . & & . & . & . & & & . \\
1 & x_{n+m+p+q}^i & y_{n+m+p+q}^i & 0 & 0 & 0 & -1 & -x_{n+m+p+q}^{i+1} & -y_{n+m+p+q}^{i+1} & 0 & 0 & 0 \\
0 & 0 & 0 & 1 & x_{n+m+p+q}^i & y_{n+m+p+q}^i & 0 & 0 & 0 & -1 & -x_{n+m+p+q}^{i+1} & -y_{n+m+p+q}^{i+1}
\end{bmatrix}
\bullet
\begin{bmatrix}
a_0^i \\ a_1^i \\ a_2^i \\ b_0^i \\ b_1^i \\ b_2^i \\ a_0^{i+1} \\ a_1^{i+} \\ a_2^{i+1} \\ b_0^{i+1} \\ b_1^{i+1} \\ b_2^{i+1}
\end{bmatrix}
=
\begin{bmatrix}
\delta_{r_1}^i - D_{r_1}^i \\
\delta_{a_1}^i - D_{a_1}^i \\
... \\
\delta_{r_n}^i - D_{r_n}^i \\
\delta_{a_n}^i - D_{a_n}^i \\
\delta_{a_{n+1}}^i - \dfrac{\Delta a_{n+1}^i}{\Delta r_{n+1}^i}\delta_{r_{n+1}}^i \\
... \\
\delta_{a_{n+m}}^i - \dfrac{\Delta a_{n+m}^i}{\Delta r_{n+m}^i}\delta_{r_{n+m}}^i \\
\delta_{r_{n+m+1}}^{i+1} - D_{r_{n+m+1}}^{i+1} \\
\delta_{a_{n+m+1}}^{i+1} - D_{a_{n+m+1}}^{i+1} \\
... \\
\delta_{r_{n+m+p}}^{i+1} - D_{r_{n+m+p}}^{i+1} \\
\delta_{a_{n+m+p}}^{i+1} - D_{a_{n+m+p}}^{i+1} \\
\delta_{r_{n+m+p+1}}^i - \delta_{r_{n+m+p+1}}^{i+1} \\
\delta_{a_{n+m+p+1}}^i - \delta_{a_{n+m+p+1}}^{i+1} \\
... \\
\delta_{r_{n+m+p+1}}^i - \delta_{r_{n+m+p+1}}^{i+1} \\
\delta_{a_{n+m+p+1}}^i - \delta_{a_{n+m+p+1}}^{i+1}
\end{bmatrix}
\quad (2.28)
$$

$$
\begin{bmatrix}
1 & 0 & 0 & 0 & 0 & 0 & 0 & 0 \\
0 & 1 & x_1^i & y_1^i & 0 & 0 & 0 & 0 \\
. & . & . & . & . & . & . & . \\
1 & 0 & 0 & 0 & 0 & 0 & 0 & 0 \\
0 & 1 & x_n^i & y_n^i & 0 & 0 & 0 & 0 \\
\dfrac{\lambda \Delta a_{n+1}^i}{4\pi \Delta r_{n+1}^i} & -1 & -x_{n+1}^i & y_{n+1}^i & 0 & 0 & 0 & 0 \\
. & . & . & . & . & . & . & . \\
\dfrac{\lambda \Delta a_{n+m}^i}{4\pi \Delta r_{n+m}^i} & -1 & -x_{n+m}^i & y_{n+m}^i & 0 & 0 & 0 & 0 \\
0 & 0 & 0 & 0 & 1 & 0 & 0 & 0 \\
0 & 0 & 0 & 0 & 0 & 1 & x_{n+m+1}^{i+1} & y_{n+m+1}^{i+1} \\
. & . & . & . & . & . & . & . \\
0 & 0 & 0 & 0 & 1 & 0 & 0 & 0 \\
0 & 0 & 0 & 0 & 0 & 1 & x_{n+m+p}^{i+1} & y_{n+m+p}^{i+1} \\
1 & 0 & 0 & 0 & -1 & 0 & 0 & 0 \\
0 & 1 & x_{n+m+p+1}^i & y_{n+m+p+1}^i & 0 & -1 & -x_{n+m+p+1}^{i+1} & -y_{n+m+p+1}^{i+1} \\
. & . & . & . & . & . & . & . \\
1 & 0 & 0 & 0 & -1 & 0 & 0 & 0 \\
0 & 1 & x_{n+m+p+q}^i & y_{n+m+p+q}^i & 0 & -1 & -x_{n+m+p+q}^{i+1} & -y_{n+m+p+q}^{i+1}
\end{bmatrix}
\bullet
\begin{bmatrix}
\Phi_0^i \\
b_0^i \\
b_1^i \\
b_2^i \\
\Phi_0^{i+1} \\
b_0^{i+1} \\
b_1^{i+1} \\
b_2^{i+1}
\end{bmatrix}
=
\begin{bmatrix}
\Phi_1^i - \dfrac{4\pi D_{r_1}^i}{\lambda} \\
\delta_{a_1}^i - D_{a_1}^i \\
... \\
\Phi_1^i - \dfrac{4\pi D_{r_n}^i}{\lambda} \\
\delta_{a_n}^i - D_{a_n}^i \\
\dfrac{\lambda \Delta a_{n+1}^i}{4\pi \Delta r_{n+1}^i}\Phi_{n+1}^i - \delta_{a_{n+1}}^i \\
... \\
\dfrac{\lambda \Delta a_{n+m}^i}{4\pi \Delta r_{n+m}^i}\Phi_{n+m}^i - \delta_{a_{n+m}}^i \\
\Phi_{n+m+1}^{i+1} - \dfrac{4\pi D_{r_{n+m+1}}^{i+1}}{\lambda} \\
\delta_{a_{n+m+1}}^{i+1} - D_{a_{n+m+1}}^{i+1} \\
... \\
\Phi_{n+m+p}^{i+1} - \dfrac{4\pi D_{r_{n+m+p}}^{i+1}}{\lambda} \\
\delta_{a_{n+m+p}}^{i+1} - D_{a_{n+m+p}}^{i+1} \\
\Phi_{n+m+p+1}^i - \Phi_{n+m+p+1}^{i+1} \\
\delta_{a_{n+m+p+1}}^i - \delta_{a_{n+m+p+1}}^{i+1} \\
... \\
\Phi_{n+m+p+q}^i - \Phi_{n+m+p+q}^{i+1} \\
\delta_{a_{n+m+p+q}}^i - \delta_{a_{n+m+p+q}}^{i+1}
\end{bmatrix}
\qquad (2.29)
$$

In the matrix, the upper index of each variable refers to the frame number, while the lower index refers to the sequential identification number of control points and tie points. Totally, there are *2(n+k+p)+m* observation equations. We denote the design matrix on the left side of the equation (2.28) or (2.29) by *A*, the observation vector on the right side by *b*, and the vector of unknown parameters by *X*. Then, we have the generic form of the observation equations:

$$\mathbf{AX} = \mathbf{b} \tag{2.30}$$

The least-squares solution for the unknown parameters can be obtained by solving normal equations as follows (Mikhail and Ackermann 1976, Press *et al.* 1992, Mikhail *et al.* 2001):

$$\hat{\mathbf{X}} = (\mathbf{A}^{\mathrm{T}}\mathbf{A})^{-1}\mathbf{A}^{\mathrm{T}}\mathbf{b} \tag{2.31}$$

where $A^T$ is the transpose of the design matrix and $(A^TA)^{-1}$ is the inverse of the matrix of the normal equations. If the normal equations are close to singular or large round-off errors are involved, the singular value decomposition (SVD) method gives a more reliable solution to the least-squares problem (Press *et al.* 1992). The simultaneous least-squares adjustment is made so that the velocities of tie points fit together as well as possible, and the residual discrepancies at the velocity control points are as small as possible.

**2.5.2. Application results and surface velocity calculation of Lambert Glacier – Amery Ice Shelf**

The Lambert Glacier basin and the Amery Ice Shelf were imaged by the Radarsat-1 C-band sensor on September 24, 1997 with a nominal look angle of 27°. The same area was imaged again on October 18, 1997 during a repeat orbit. Figure 2.4 shows the

coverage of the interferometric SAR data. The image strip consists of 8 consecutive frames of interferometric SAR data pairs. Each frame covers a ground area of 100 km by 100 km, with about 10 km wide overlap between neighboring frames. Due to fast ice motion and relatively high relief, the conventional phase unwrapping method does not work well, and no reliable phase measurements can be made for this site. Therefore, the speckle tracking method is used to derive both the range and azimuth displacements. The cross-correlation is performed using the single look slant range amplitude images. This study experimented with different sizes for the match window. Larger window sizes generally produce more and stronger matches, but require greater spacing between adjacent velocity nodes to minimize the correlation of those surface displacement estimates. An amplitude match was accepted as a successful match based on an experimentally determined correlation threshold of 0.05. This study chose an optimal window size of 96 by 96 pixels, which produced a dense coverage of observations. The match only failed in the margins of the ice streams with high shear strain rate, in the central part of the confluence of the Lambert Glacier, the Mellor Glacier, and the Fisher Glacier, and in a small patch toward the front of the Amery Ice Shelf.

The correlation peak was determined by oversampling the correlation surface by a factor 10. The matched points were checked for outliers using a median operator. A match whose estimated range or azimuth offset differs from the median of its surrounding match points by a specified threshold value was flagged as an outlier and discarded. We interpolated good match points into a range offset grid and an azimuth offset grid with a spacing of 200 m. The topography induced component is removed

from the range offset grid by using the OSU Digital Elevation Model (DEM) (Liu *et al.* 1999).
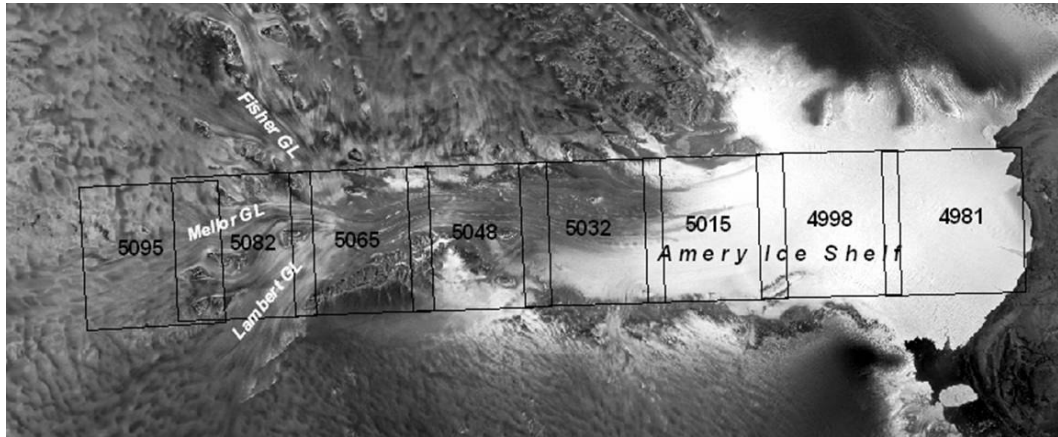


Figure 2.4 Data coverage of Radarsat interferometric data over the Lambert Glacier and the Amery Ice Shelf acquired in 1997.

First, this study uses frame 5095 and frame 5082 to demonstrate the advantages of simultaneous least-squares adjustment over independent frame-by-frame adjustment. Since no *in-situ* velocity measurements are available for this region, rock outcrops are identified and used as stationary velocity control points. This study identified 17 stationary velocity control points for frame 5082 and 16 stationary velocity control points for frame 5095, which are well distributed in both the range and azimuth directions. Following Equation (2.10) and Equation (2.11), 34 observation equations for frame 5082, and 32 observation equations for frame 5095 are written based on the control points. With overabundant observation equations, this study calibrated the

unknown parameters $a_0$, $a_1$, $a_2$. $b_0$, $b_1$, and $b_2$ respectively for frame 5082 and frame 5095 as shown in Table 2.1 using the calibrated parameters, the motion induced surface displacements in the range and azimuth directions were computed for each grid cell, and the surface velocity for each grid cell was then calculated by using Equations (2.5) and (2.6). In the calculation, the surface slopes along the range and azimuth directions were estimated by using the OSU Digital Elevation Model (DEM) (Liu *et al.* 1999).

Table 2.1 Comparison of model parameters of frames 5082 and 5095 calibrated by the frame-by-frame method and the simultaneous adjustment method.

| Model parameters | Frame-by-frame calibration | | Simultaneous calibration | |
|---|---|---|---|---|
|  | Frame 5095 | Frame 5082 | Frame 5095 | Frame 5082 |
| $a_0$ | -7.77726 | -1.22928 | -7.61446 | -1.25436 |
| $a_1$ | -0.000225 | -0.000278 | -0.000257 | -0.000267 |
| $a_2$ | -0.0000074901 | -0.0000143081 | -0.0000127392 | -0.0000154897 |
| $b_0$ | -88.9 | 412.4678 | -88.83 | 412.5 |
| $b_1$ | 0.0001488 | 0.0001197 | 0.0001361 | 0.0001225 |
| $b_2$ | 0.0000181 | 0.000001494 | 0.00001546 | 0.0000013 |

As shown in Figure 2.5, the spatial pattern of the derived speed appears consistent with glacial features and the flow directions agree well with ice flow stripes in

the scene. However, the merged velocity field has an obvious seam line (Figure 2.6a), which indicates a sudden change in velocity between frame 5082 and frame 5095. In fact, the average speed discrepancy between frames is about 6 m/year for the overlapping area.



(a)                                              (b)
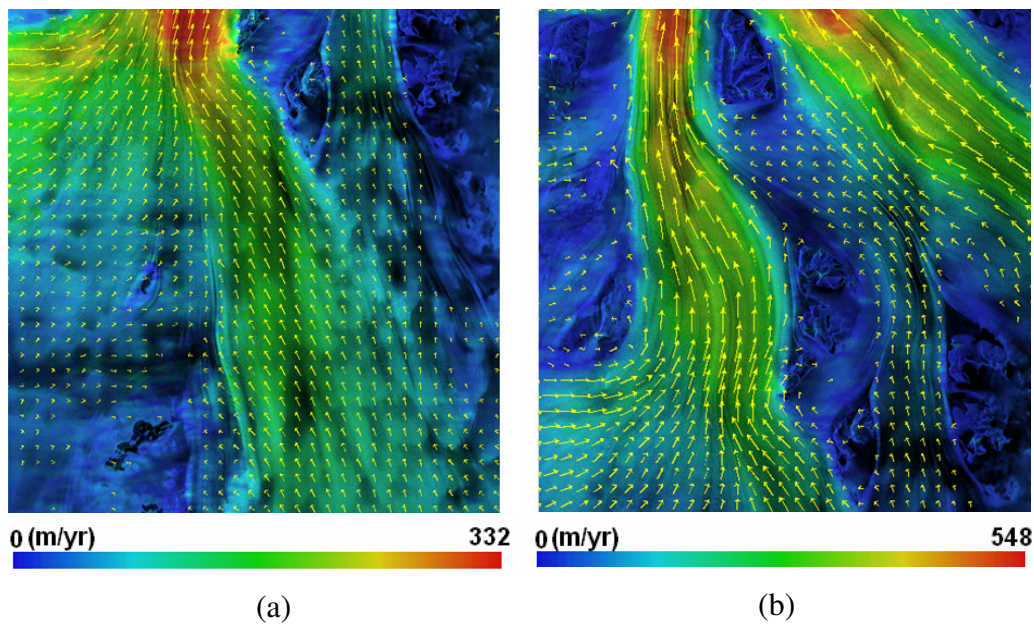
Figure 2.5 Two-dimensional velocity fields derived by the speckle tracking method. (a) frame 5082; (b) frame 5095.

With 30 tie points in the overlapping area between two frames, a simultaneous least-squares adjustment is performed. The tie points were initially determined by using ancillary information in the header files and then refined using the cross-correlation

matching with sub-pixel level accuracy. Following Equations (2.23) and (2.24), we obtained 60 observation equations for the tie points. By combining 17 stationary velocity control points from frame 5082, 16 stationary velocity control points frame 5095, and 30 tie points, 126 observation equations are obtained in a matrix format similar to Equation (2.28). The unknown parameters $a_0$, $a_1$, $a_2$. $b_0$, $b_1$, and $b_2$ for frame 5082 and frame 5095 were simultaneously computed based on the 126 observation equations, as shown in Table 1. The parameters calibrated by the simultaneous least-squares adjustment were used to re-compute the velocity fields for the two frames. The consistency of the estimated velocity between two frames was greatly improved. The velocity difference for each pixel in the 10 km wide overlapping area is calculated. The average velocity difference has been reduced from 6 m/year to 1.33 m/year, and the standard deviation of the velocity difference has also been reduced from 9.5 m/year to 4.6 m/year. Note that the standard deviation value mainly represents the effect of random noise, and the effect of the simultaneous least-squares adjustment on the reduction of the systematic bias is obviously greater than that of the random error. The simultaneous adjustment achieved a continuous transition of the velocity field between the two frames as evidenced by the seamless velocity mosaic in Figure 2.6b.
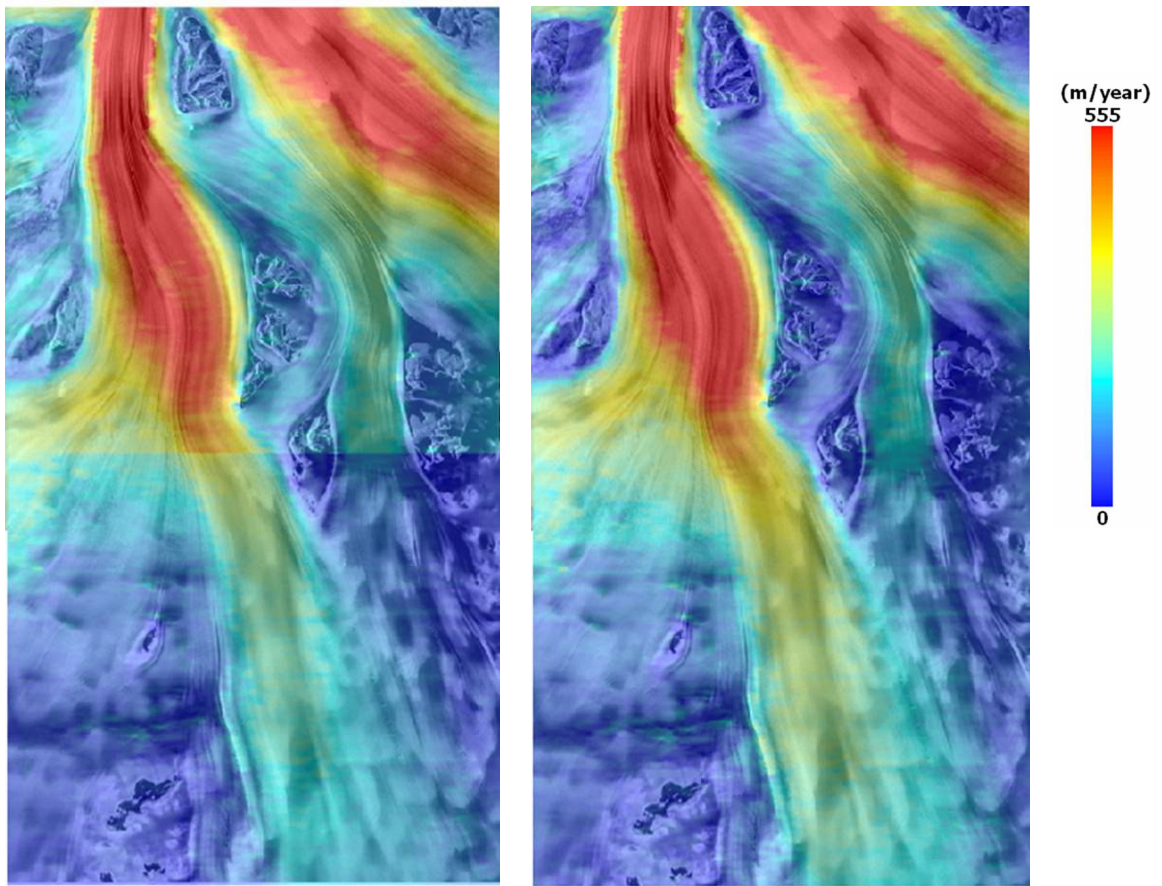
Figure 2.6 Velocity mosaic of frames 5082 and 5095. (a) processed by the frame-by-frame method; (b) processed by the simultaneous adjustment method.

The simultaneous least-squares adjustment method also eliminates the stringent requirement regarding velocity control points for each frame. To demonstrate this desirable property, we dropped the 17 stationary velocity control points for frame 5082, and only employed 16 stationary velocity control points for frame 5095 and 30 tie points. In the course of the simultaneous strip adjustment, the parameters $a_0$, $a_1$, $a_2$. $b_0$, $b_1$, and $b_2$ for frame 5082 were calculated based on the tie points and stationary velocity control points in the adjacent frame 5095. As shown in Table 2.2, the parameters

estimated for frame 5082 without using the velocity control points in this frame are very similar to those calculated by using the velocity control points in this frame. The average velocity difference for the entire frame is only 3.2 m/year, compared with the velocity estimates using velocity control points in frame 5082. This demonstrates that the simultaneous least-squares adjustment method is able to derive the velocity measurements for those frames without velocity control points. This is of particular importance for flat featureless snow surfaces such as portions of the Amery Ice Shelf covered by frames 4998 and 4981, where no rock exposures can be found and used as stationary velocity controls.

Table 2.2 Model parameters for frame 5095 derived respectively without using its own velocity control points and using flow direction control points.

| Model parameters | Without velocity control points from frame 5095 | Using flow direction control points in frame 5095 |
|---|---|---|
| $a_0$ | -7.53359 | -7.67819 |
| $a_1$ | -0.000278 | -0.00024 |
| $a_2$ | -0.0000131975 | -0.0000141040 |
| $b_0$ | -88.78 | -88.7485 |
| $b_1$ | 0.00013 | 0.0001405 |
| $b_2$ | 0.000007757 | -0.000005634 |

Figure 2.7 Flow direction control points identified for frame 5095 based on visible ice flow stripes.

Flow direction control points can be used alone or in conjunction with stationary velocity control points in the least-squares adjustment for solving the unknown parameters for a frame. To demonstrate this, 24 flow direction control points for frame 5095 are identified by drawing a line segment along the visible flow stripes on the slant range SAR image. The flow direction control points are shown in Figure 2.7 as line segments, and their positions are marked as circles in the middle of the line segments. Following Equation (2.16), 24 observation equations are established for the flow direction control points. As shown in Figure 2.7, the flow stripes used for flow direction

control have different orientations, which ensure linear independence between the observation equations. By using 24 observation equations derived only from the flow direction control points, we calibrated the parameters for frame 5095. As shown in Table 2.2, the parameter values of $a_0$, $a_1$, $a_2$. $b_0$, $b_1$, and $b_2$ calibrated from the flow direction control points are similar to those calibrated from the stationary velocity control points. The corresponding velocity difference is 8.1 m/year on average for the entire frame, compared with the results from the stationary velocity control points. It should be pointed out that the parameters calibrated by the stationary velocity control points have higher accuracy and should be used whenever they are available. Nevertheless, if stationary velocity control points cannot be identified, flow direction control points can be used instead to derive velocity estimates at a slightly lower but accepTable level of accuracy.

Table 2.3 The number of velocity control points and flow direction control points used in the unified least-squares adjustment of eight interferometric data frames over the Lambert Glacier and the Amery Ice Shelf.

| Frame | Stationary velocity control points | Flow direction control points |
|---|---|---|
| 5095 | 16 | 0 |
| 5082 | 17 | 0 |
| 5065 | 15 | 0 |
| 5048 | 18 | 0 |
| 5032 | 14 | 0 |
| 5015 | 3 | 14 |
| 4998 | 0 | 9 |
| 4981 | 0 | 6 |
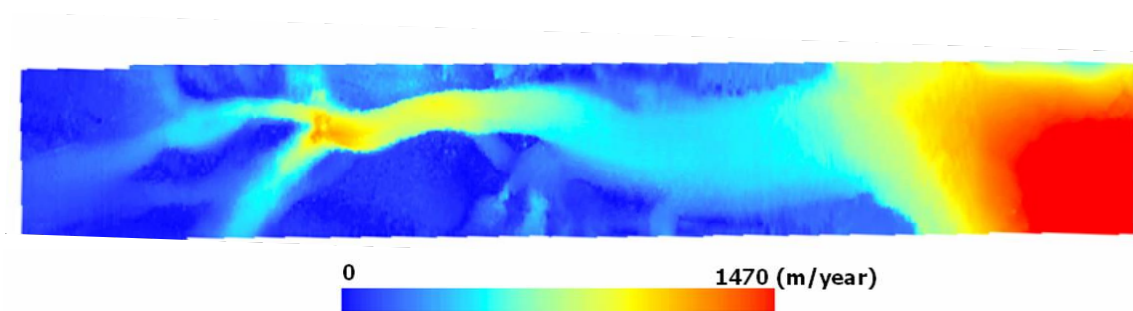


Figure 2.8 A seamless velocity mosaic over the Lambert Glacier and the Amery Ice Shelf derived by the unified least-squares adjustment.

To derive a seamless velocity mosaic for the entire strip, a unified simultaneous least-squares adjustment of the eight consecutive interferometric frames is performed by integrating stationary velocity control points, flow direction control points and tie points. As shown in Table 2.3, this study identified plenty of stationary velocity control points for the five frames on the left side of the strip, a few stationary velocity control points for frame 5015, and no stationary velocity control points for frame 4998 and frame 4981. Nevertheless, it was able to extract 9 flow direction control points for frame 4998 and 6 flow direction control points for frame 4981. This study identified 30 tie points for adjacent frames, resulting in 210 tie points for the entire strip in total. The combination of stationary velocity control points, flow direction control points and tie points from all frames creates observation equations in a similar matrix format as Equation (2.28). This study simultaneously computed the parameters for all eight frames and hence created a seamless velocity mosaic across the entire strip as shown in Figure 2.8. Ice surface velocity is shown as a color overlay. The lower speeds are represented with blue tones, changing to red for the highest speeds. Velocity varies considerably along the glacial floor and the ice shelf. It increases from the interior up to about 800 m/year at the confluence of the Lambert Glacier, the Mellor Glacier and the Fisher Glacier. Then, the velocity decreases to lower values of 300-350 m/year in the middle section and increases to a maximum of about 1470 m/year near the front of the Amery Ice Shelf.

**2.5.3. Discussion**

The observation equations contributed by tie points free us from the stringent need of velocity control points (stationary or non-stationary) and/or flow direction control points for each frame. The simultaneous strip or block adjustment solves one difficult practical problem: for some image frames we are unable to identify a sufficient number of velocity control points. By exploiting tie points in the strip or block adjustment, unknown parameters for those frames without velocity control points can be calibrated based on distant velocity control points in other image frames. In other words, velocity control points in one frame can contribute to the calibration of unknown parameters of other frames through tie points. The incorporation of constraints imposed by tie points also minimizes the discrepancies of velocity measurements derived from adjacent image frames for overlapping areas. The improved consistency makes it possible to create a seamless velocity mosaic. In addition, the integration of all velocity control points within a strip or a block will increase the redundancy of observation equations and constrain the propagation of errors in individual velocity control points.

**2.6. Surface velocity of the Lambert Glacial Basin**

Following the method described above, a two-dimensional surface velocity map is created along the orbit passing the confluence area of Lambert, Mellor and Fisher Glaciers to the discharging area of Amery Ice Shelf using the speckle tracking method (Figure 2.8). The two-dimensional surface velocity map of the study area from the three pass interferometry technique is processed and provided by Ohio State University

(Figure 2.9). The ascending and descending pass have been used for surface velocity extraction using InSAR data acquired from the Antarctic Mapping Mission 2 (AMM-2) in 2000 (Jezek, 2002). The 25 m resolution Radarsat-1 SAR data is available for the most of Lambert Glacial Basin–Amery Ice Shelf system with 24-day orbit cycles and 6 days of repeat-pass acquisitions.

The available velocity data covers about 90% of the Lambert Glacier–Amery Ice Shelf basin (Figure 2.9); though more important is that most of the main ice streams are covered, thereby enabling this study to investigate the dynamics of glacier systems such as strain rate, and ice thickening and thinning. Possible problems lie with error pixels in the process of phase unwrapping, and the discontinuous velocity variations on the border of orbits because of different processing parameters used for each orbit. In addition, the phase unwrapping process in a fast moving area leaves no velocity patches in the middle of the ice streams. As Figure 2.9 shows, there are many vertical stripes observed in the surface velocity which can cause discontinuous surface velocity variations which are more severe in low velocity areas in high elevation. The highest velocity of the original data set is unreasonably high (3791 m/year) because of error pixels. The south part of the upstream region contains many small patches that are mostly error pixels. Furthermore, no-data patches can be identified in the high surface velocity areas such as confluence area of Lambert, Mellor, and Fisher Glaciers and ice discharging area of Amery Ice Shelf front.

Figure 2.10 shows the speed error distributions of surface velocity derived from SAR interferometry. There are different error distributions between the orbits depending on the surface velocity extraction methods. If the velocity is extracted by phase unwrapping for range and by the offset method for the azimuth direction, it produces speed error ranges between 2 to 4 m/year, where as the offset method for both azimuth and range direction is in the error range of 7 to 16 m/year. However, if the phase unwrapping or the coregistration process is not successful, the maximum error is increased to 52 m/year. Although there are some portions that have error ranges more than 18 m/year, most of the ice streams are less than 8 m/year, except for no-data areas and some shear margins. Therefore, it is safe to say that the ice velocity data this research uses is trustable in terms of mass balance calculations and ice dynamic analysis in spite of the discontinuous velocity distribution between the orbits. This discontinuity may cause errors on the orbit boundaries for strain rate and ice thickening analysis; however, the output result of those analyses should be trustable since the calculation is relative to neighboring pixels which have continuous distributions within the orbit.
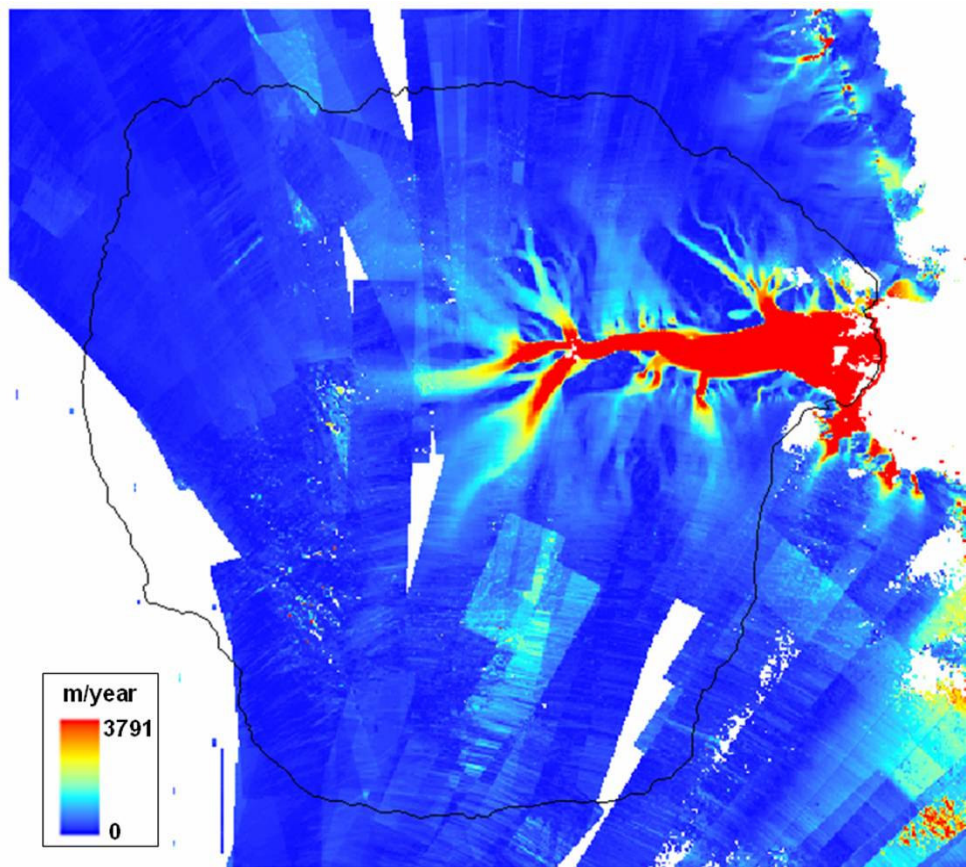
Figure 2.9 Original surface velocity derived from SAR interferometry by Ohio State University.
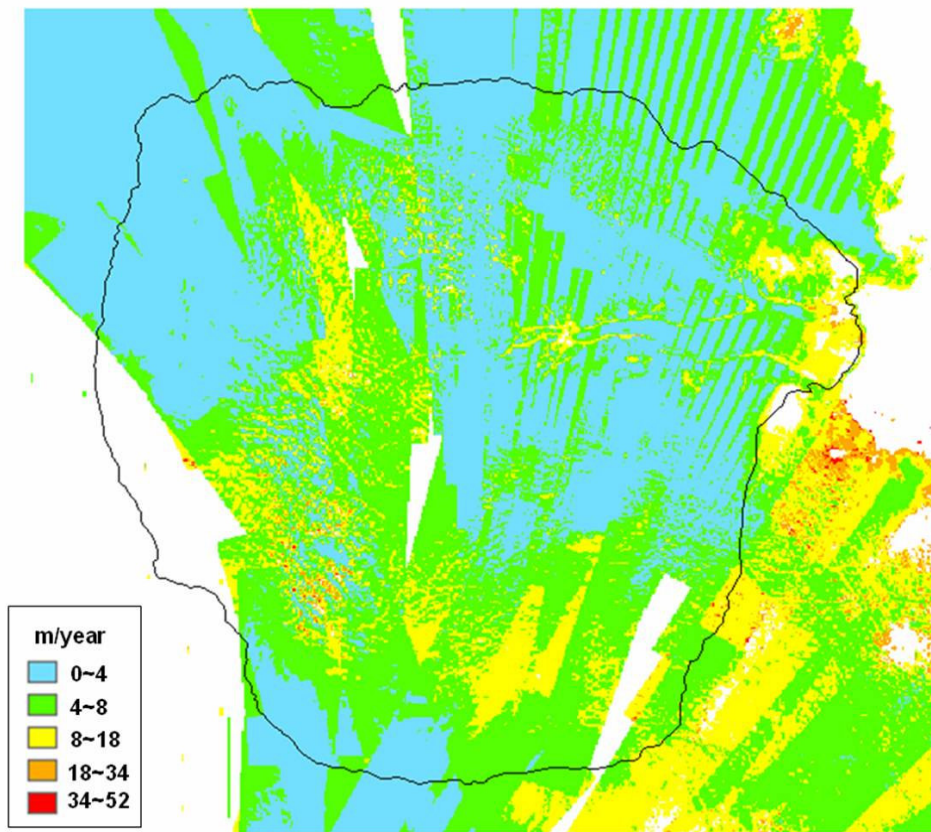
Figure 2.10 The error distribution of surface velocity field derived by the Ohio State University.

The problems of velocity error pixels and no-data pixels in the major ice stream can involve huge effects in ice dynamics analysis. To minimize the problem, a median filter with a 5 x 5 kernel was applied until the definite error pixels were removed. After three filtering passes, the most critical error pixels were removed without degrading the valid data points (Figure 2.11). The no-data pixels were interpolated by linear Triangulated Irregular Network (TIN) interpolation, except for the confluence region of Lambert, Mellor, and Fisher Glaciers where the surface velocity changes dramatically as

glacier dynamics change. In addition, the confluence region was considered as the grounding line position, and that is critical for the mass balance calculation since the flux gate should be located along the grounding line. The velocity field from speckle tracking mentioned in previous sub-chapters was used to fill out the gaps in the region.

As a result, the post processed 2 dimensional surface velocity filed was created (Figure 2.11). All the major ice streams and tributary ice streams are clearly distinguished, and the maximum ice velocity is decreased to 1516 m/year at the ice shelf front as the error pixels are removed. The general surface velocity increases as the glaciers merge into the confluence region, and the velocity increases abruptly at the region of 800 m/year. It decreases as it is floating as an ice shelf with the ranges of 300~400 m/year in the middle, and increases to 1200 ~ 1500 m/year in the ice shelf front area as the tributary glaciers merge and the main ice stream discharges into the ocean.

This velocity field is utilized for the ice dynamics and mass balance analysis as a core part. The strain rate is calculated based on velocity gradient in x and y direction in unit distance in Chapter III. The vertical velocity field from InSAR process is used for grounding line identification in Chapter IV. The mass imbalance is calculated by comparing balance velocity and the surface velocity field in Chapter V. The flow direction information from the surface velocity field is used for sub-basin delineation. The ice flux is calculated based on the surface velocity at flux gate for mass balance and basal melting calculation in Chapter VI.
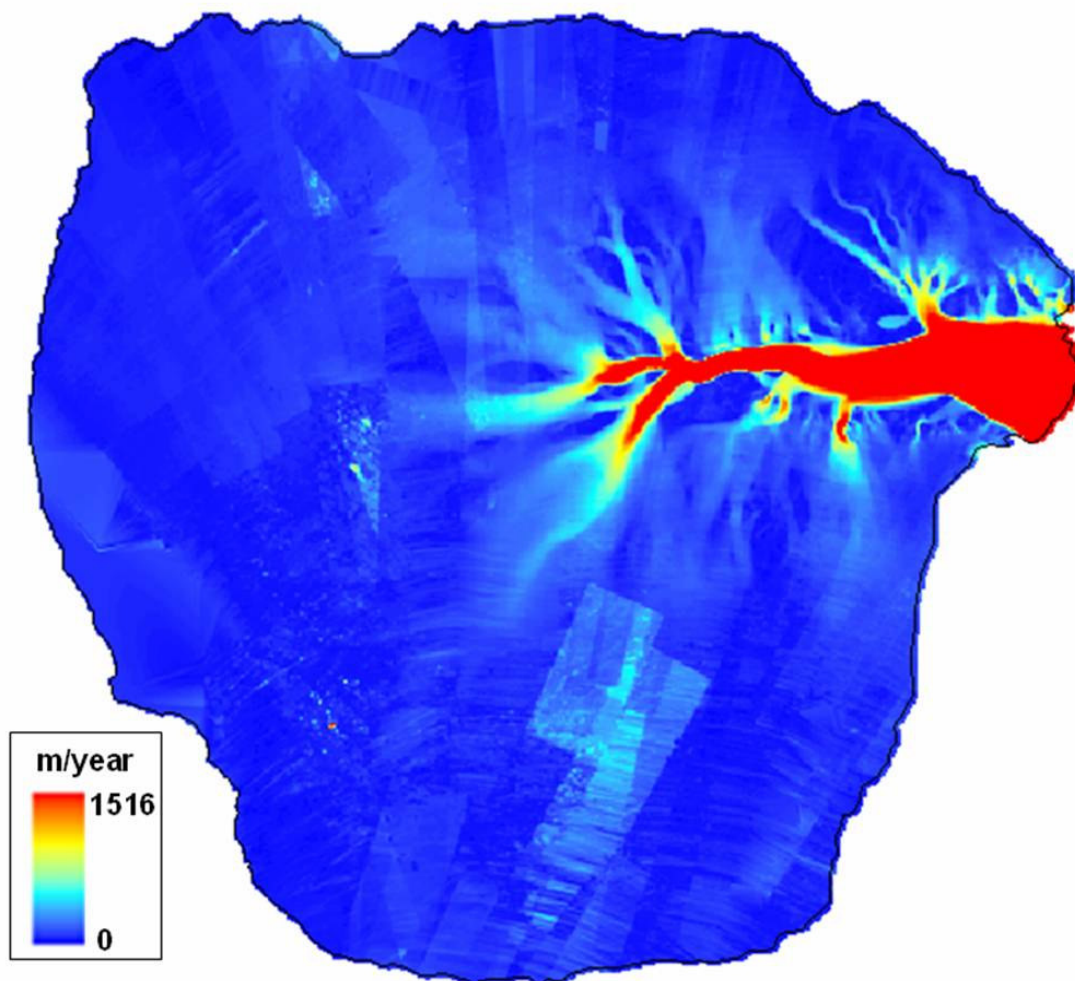
Figure 2.11 Post-processed surface velocity field of the Lambert Glacier – Amery Ice Shelf system.

## CHAPTER III

## STRAIN RATE ANALYSIS

### 3.1. Concept of strain rate

Strain rate is the main component used to explain large scale ice flow dynamics. The glacier flow manifests a relationship between the ice deformation (strain) and stress (force/unit area) that produces strain (Ritter *et al.* 1995). Especially, glacier flow deforms by shear stress when it flows by a function of glacier movement by internal deformation (shear stress) (Ritter *et al.* 1995). Until recent developments in the extraction of surface ice flow velocity using satellite remote sensing techniques, ice deformation was measured by field measurements implementing stake networks and surveying their deformation over a known time interval (Nye 1959, Zumberge *et al.* 1960, Drew and Whillans 1984, Thomas *et al.* 1984, MacAyeal 1985).

Since shear stress is directly related to surface velocity, the velocity at any depth along the central axis of ice can be estimated by assuming that the shear stress is proportional to depth and that the strain rate directly relates to that stress (Ritter *et al.* 1995). Therefore, it is safe to say the surface velocity is the sum total of strain rates for all the layers within the ice mass (Ritter *et al.* 1995). Therefore the strain rate can be calculated if the surface ice flow velocity is known.

From the velocity, strain rates in the longitudinal and transverse directions can be calculated. The surface stress field can be calculated from the surface strain rate using the Glenn's flow law of ice. Interferometrically derived surface velocity has become one

of the most effective tools for calculating strain rate distribution over an ice sheet (Yong and Hyland 2002, Forster *et al.* 1998, Pattyn and Derauw 2002). Forster *et al.* (1998) show that longitudinal strain rates along a flow line within the main ice stream can be calculated directly from the unwrapped phase with an accuracy of about 15%. This chapter first describes previous strain rate studies for the Lambert Glacier-Amery Ice Shelf System, then details strain rate calculation methodology using surface velocity information, and finally discusses the resulting strain rate of the Lambert Glacier-Amery Ice Shelf System.

There have been some studies on the strain rate of Amery Ice Shelf using field measurements and satellite techniques. However, the strain rate for the grounded ice of Lambert Glacier is not well known. Initial measurements of the velocity and strain-rate distribution on Amery Ice Shelf were obtained by surveys from electronic distance-measuring equipment and theodolite in 1968 and 1970 (Budd *et al.* 1982). The survey was carried out along a 260 km long profile aligned along the average flow direction of Amery Ice Shelf, and two transverse profiles; one across the shelf near the front, the other near the longitudinal profile. The velocities for tributary glaciers were measured at 11 points in the 1970s (Allison 1979). These surveys provided velocity values on the upper reaches of these glaciers. Global positioning systems have been utilized for velocity measurements in the 1990s (Manson *et al.* 2000).

However, the study of strain rate distribution for the entire Amery Ice Shelf has been unknown until Young and Hyland (2002) created a strain rate distribution method based on surface velocity as extracted by speckle tracking techniques. Using

RADARSAT-1 SAR interferometry pairs, they calculated the surface velocity and strain rate for Amery Ice Shelf within an accuracy of 8 m/year along-track, and 27 m/year across-track for the surface velocity. In addition to the transverse shear strain rate, longitudinal and transverse strain rate components were calculated over an 8 km distance scale. They found a systematic variation of strain rate over the ice shelf, and were successful in identifying shear stress margins where the strain rate exceeds $0.1$ $a^{-1}$. The strain rates are largest in the shear margins in the southern section of the shelf, and the middle stream shows the strain distribution of a distinct longitudinal pattern. However, their study was limited in the ice shelf area where velocities were sufficient to use from speckle tracking. This study overcomes the limitations of previous studies based on the analysis of not only ice shelf but also major and tributary glaciers discharging into Amery Ice Shelf.

## 3.2. Calculation method

The along-track and across-track displacements obtained from interferometry were interpolated in 400 m by 400 m. Since the velocity field still contains high-frequency noise associated with errors, the original velocity field is smoothed using a 5 by 5 cell size median filter until the error points are removed. Velocity gradients for strain rate calculations are considered constant within any window and are determined through a linear regression analysis of all x directional and y directional velocity values in that window with respect to the x and y direction (Pattyn and Derauw 2002). This study used a 9 by 9 window for the linear regression analysis of x and y directional velocity

gradients. To simplify the strain rate calculations, this study applied ice depth velocity average factor of 0.87 (Budd and Warner 1998) for grounded ice, and assumed that the strain rates calculated from ice depth average velocity represents the strain rate of the point.

If a stress is applied to a medium, the strain or deformation is expected to occur. If it considers infinitesimal displacements which the time required for the deformation is zero, the normal strain in the x direction at the point is defined as

$$\varepsilon_{xx} = Lim_{l \to 0} \frac{\Delta l}{l} \tag{3.1}$$

where $l$ is the length of a line drawn in the x direction, and $\Delta l$ is the elongation of that line., so $\Delta l / l$ is the elongation of the line per unit length. If end of the line l is moved a distance $\bar{x}$ in the x-direction, it's the other end moves a distance $\bar{x} + l(\partial \bar{x} / \partial x)$ in this direction, and the x-component of its new length is $l + \Delta l$, then the equation 3.1 is:

$$\varepsilon_{xx} = Lim_{l \to 0} \frac{\bar{x} + l(\partial \bar{x} / \partial x) - \bar{x}}{l} = \frac{\partial \bar{x}}{\partial x} \tag{3.2}$$

To obtain strain rate in a deforming ice mass, it is necessary to differentiate with respect to time. Thus, the normal strain rate in the x-direction is:

$$\dot{\varepsilon}_{xx} = \frac{d\varepsilon_{xx}}{dt} = \frac{d}{dt} \frac{\partial \bar{x}}{\partial x} \tag{3.3}$$

Velocity is defined as a change in distance with time. If $u$ is the velocity in the x direction, $u = d\bar{x} / dt$. Thus, we obtain:

$$\dot{\varepsilon}_{xx} = \frac{\partial u}{\partial x} \tag{3.4}$$

Since the major ice motion is in the x direction from the Mellor and Lambert glaciers to Amery Ice Shelf, the major strain components are the surface longitudinal strain rate $\dot{\varepsilon}_{xx}$, the surface transverse strain rate $\dot{\varepsilon}_{yy}$, and the surface lateral shear-strain rate $\dot{\varepsilon}_{xy}$, defined as

$$\dot{\varepsilon}_{xx} = \frac{\overline{\Delta V_x}}{\Delta X} \tag{3.5}$$

$$\dot{\varepsilon}_{yy} = \frac{\overline{\Delta V_y}}{\Delta Y} \tag{3.6}$$

$$\dot{\varepsilon}_{xy} = \frac{1}{2}\left(\frac{\overline{\Delta V_x}}{\Delta X} + \frac{\overline{\Delta V_y}}{\Delta Y}\right) = \frac{1}{2}\left(\dot{\varepsilon}_{xx} + \dot{\varepsilon}_{yy}\right) \tag{3.7}$$

where the overbar denotes the averaging over the window, and $\Delta V_x$ and $\Delta V_y$ denote velocity gradients within the unit distance of $\Delta X$ and $\Delta Y$ in x and y direction.

Since this study uses a 9 by 9 window for strain rate calculation, 81 observation equations for each x and y direction should be constructed to solve the equation as;

$$V_{x_1} = a_x + b_x x_1$$

$$\ldots \quad \ldots \tag{3.8}$$

$$V_{x_{81}} = a_x + b_x x_{81}$$

for x direction, where $a_x$ and $b_x$ denote coefficients for the x directional velocity gradient model. And the observation equations for the y directional model can be explained as the following;

$$V_{y_1} = a_y + b_y y_1$$

$$\ldots \quad \ldots \tag{3.9}$$

$$V_{y_{81}} = a_y + b_y y_{81}$$

where $a_y$ and $b_y$ denote coefficients for the y directional velocity gradient.

Each window has one matrix constructed for mathematic solutions in the x and y directions, respectively, and coefficients for each window are calculated as the window moves. The matrix model for i$^{th}$ window can stated be as the following,

$$\begin{bmatrix} 1 & x_1 \\ 1 & x_2 \\ ... & ... \\ 1 & x_{81} \end{bmatrix} \bullet \begin{bmatrix} a_x^i \\ b_x^i \end{bmatrix} = \begin{bmatrix} Vx_1 \\ Vx_2 \\ ... \\ Vx_{81} \end{bmatrix} \tag{3.10}$$

for the x directional model, and

$$\begin{bmatrix} 1 & y_1 \\ 1 & y_2 \\ ... & ... \\ 1 & y_{81} \end{bmatrix} \bullet \begin{bmatrix} a_y^i \\ b_y^i \end{bmatrix} = \begin{bmatrix} Vy_1 \\ Vy_2 \\ ... \\ Vy_{81} \end{bmatrix} \tag{3.11}$$

for the y directional model.

Since the matrix has a form of M x N and the number of rows M is greater than or equal to its number of columns N, a least-squares model of singular value decomposition is used to solve the parameters (Mikhail and Ackermann 1976).

## 3.3. Strain rate of the Lambert Glacial Basin

Based on the methodology above, longitudinal, transverse, and lateral shear strain rates are calculated. Since the strain rate is applied mainly for the ice stream area, and the slow surface velocity field contains a larger error rate in the flow direction from the velocity field, the strain rate field with surface velocity above 15 m/year is clipped for

visual interpretation and error removal. The value of the longitudinal (x directional) strain rate is positive where the velocity increases downstream (rightward or northward). The value of the transverse (y directional) strain rate is positive where the velocity increases Eastward. The lateral shear strain is positive where the velocity increases to the right, which most of the major ice stream is in the down stream direction. This means that it is positive on the left margin of the stream on the ice shelf and decreases in magnitude towards the center of the stream.

Where the ice is freely floating, it effectively moves as a block. Therefore, the surface strain field for the ice shelf is representative of the strain field through the entire ice thickness whereas for grounded ice takes the assumption of depth averaged velocity and homogeneous strain rates for the thickness.

As Figure 3.1 shows, the lateral shear strain rate distribution defines the shear margins of ice flows. The range of lateral shear strain varies depending on the location and ice flow velocity from -0.0621 to 0.0542 $a^{-1}$. The result explains that the major ice stream of Lambert and Mellor Glaciers and their confluence area experiences the most severe ice deformation and the width of the shear margin decreases as it flows downstream except for the convergent area with the tributary glaciers. The high values of the strain rate in the shear margins have noteworthy implications for the internal properties of the ice flows (Young and Highland 2002). Because of low quality for orbital adjustment for the original velocity data, artifacts appear in a diagonal direction. But the general pattern and the value of the strain rate within the orbit are correct and provide an effective view on glacier dynamic analysis and flow regime description.
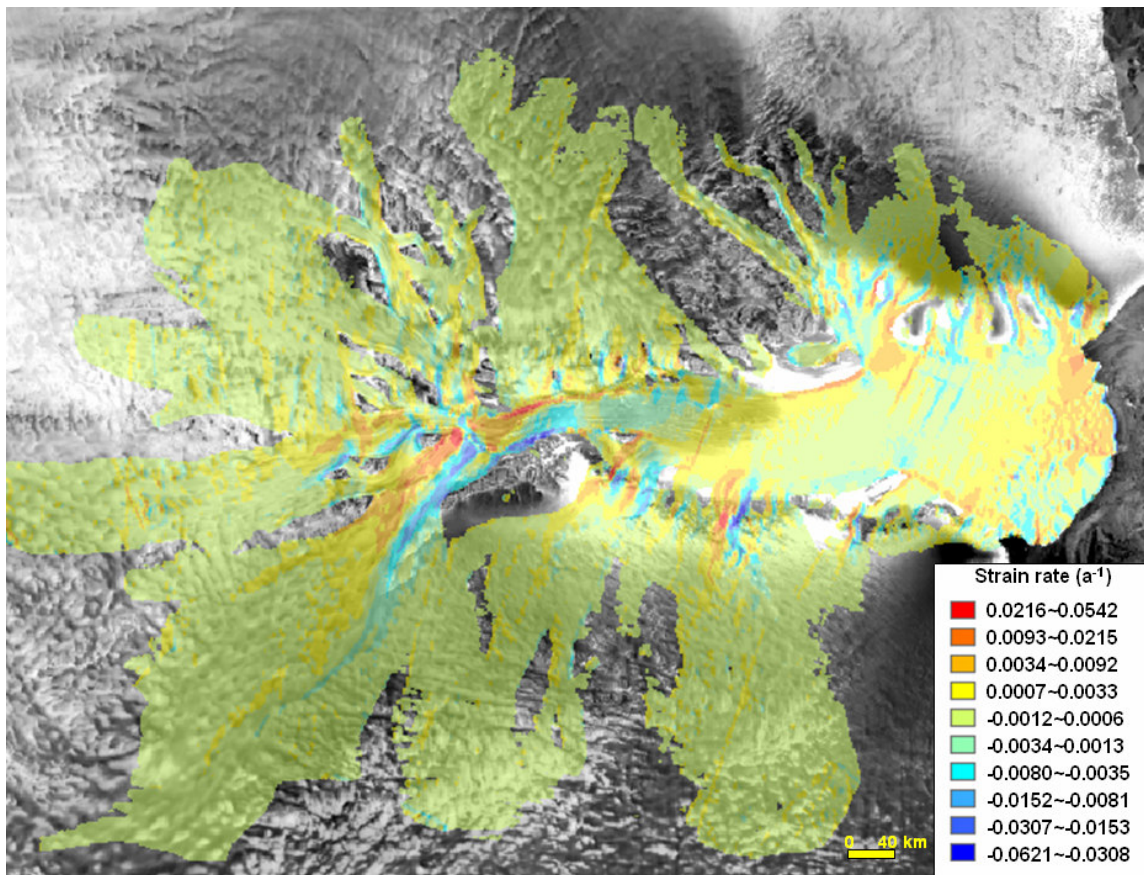
Figure 3.1 Lateral shear strain rate of the Lambert Glacier – Amery Ice Shelf system.
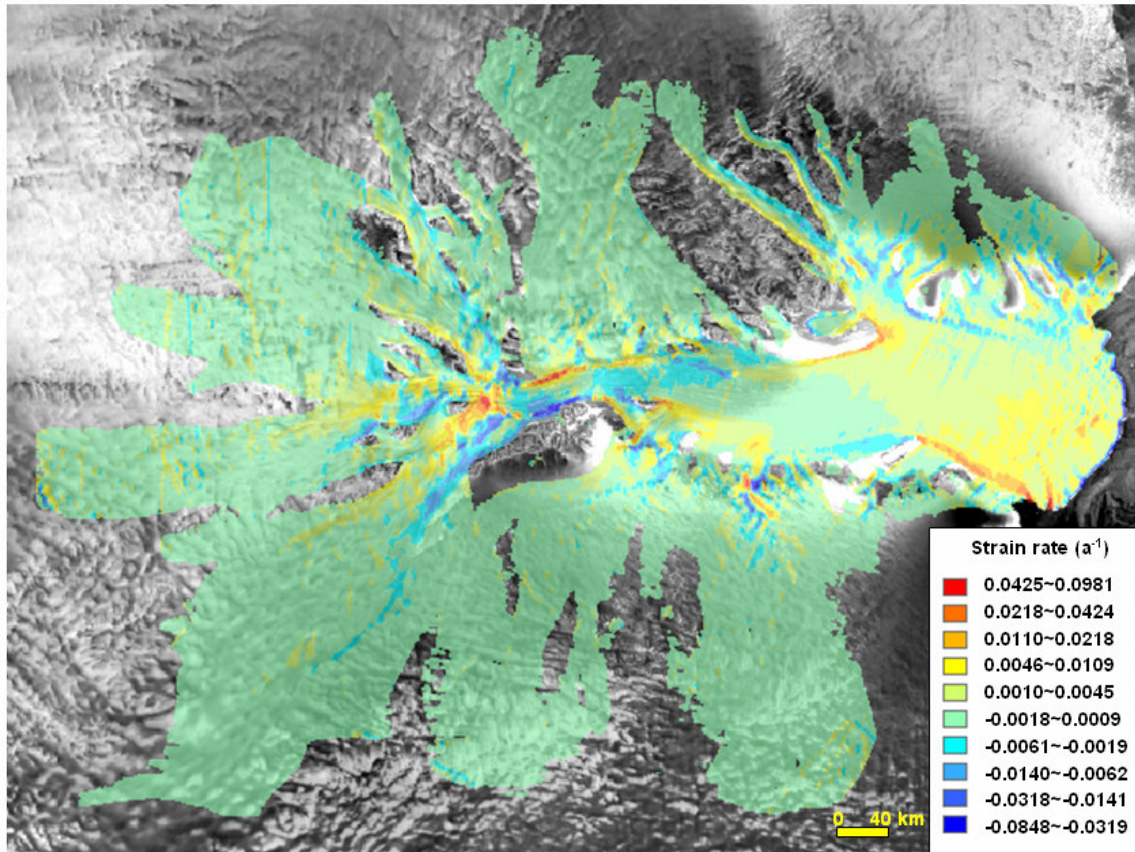
3.2 Longitudinal strain rate of the Lambert Glacier – Amery Ice Shelf system.

Since in the polar stereographic projection in this study the generally north-flowing major ice streams and Amery Ice Shelf moves in x direction, the longitudinal strain is the main component of ice deformation for the main ice stream. It tells the strain rate distribution for the center part of the main ice streams. As Figure 3.2 shows, the confluence region has the highest ice deformation in the main ice stream with the maximum values of 0.075 and -0.039 $a^{-1}$. Especially, the elongated zone of high positive strain rate distribution is observed at the main ice streams confluence where the grounding line is located as the ice velocity increases at the grounding zone. The

longitudinal strain rate becomes negative as the velocity decreases after the ice is floating. Because of the stable ice stream movement in the middle of the ice shelf, the middle of the ice stream shows minimal longitudinal ice deformations. Notably, the front of the ice shelf shows variable positive strain rate values ranging 0.089 to 0.014 $a^{-1}$. These imply the extensive deformation at the ice shelf front, and it may contribute to the development of longitudinal rifts and crevasses. The high positive strain rate distribution and the rifts and fractures distribution observed in SAR image mosaic shows close correspondence.

### 3.3.1. Strain rate of grounded ice of Lambert, Mellor and Fisher Glaciers

As mentioned before, the strain rate for grounded ice assumes that shear stress is proportional to depth and the depth averaged velocity represents the depth averaged stress, therefore the strain rate calculated for grounded ice is directly related to that stress. The grounded ice flow shows a very complicated strain rate distribution (Figure 3.2). Since it neglects effects of the basal friction, the there are limited interpretations for the complicated pattern. However, the general pattern of strain rate distribution can be explained through the ice flow direction, velocity, ice flow merging, and rock exposure along the glacier. The longitudinal and transverse strain rate profile supports the interpretation of the strain rate distribution of this study.

The strain rate of the grounded Lambert Glacier shows characteristic trends of positive and negative strain rate bands along the flow caused by high velocity flow and shear margin by Mawson Escarpment and Cumpston Massif (Figure 3.2). The highest

strain rate is detected at the confluence area with Mellor Glacier of 0.0482 $a^{-1}$ which is a major effect of ice streams merging. The lowest strain rate of -0.0267 $a^{-1}$ is identified near the grounding line on the east side of the glacier and is caused by a velocity increase in the grounding zone.

Two flow lines are placed along the east and west shear margin to illustrate the longitudinal variation in strain rate, and the other two for upstream and downstream for the transverse strain rate profile (Figure 3.2). The west longitudinal shear margin (Figure 3.3 a) shows a plain distribution as ice flow approaches to Cumpston Massif which acts as a major obstacle to the flow. As the glacier flows towards Cumpston Massif, the strain rate abruptly increases to 0.03 $a^{-1}$ then decreases to 0.005 $a^{-1}$ as it flows away from the massif. Another positive strain rate peak is observed around 123,000 m of the flow line and is caused by the ice flow merging with Mellor Glacier as they face each other. It results in the high deformation of the region. The strain rate drops down as it approaches the grounding line with increasing velocity (Figure 3.3 a).
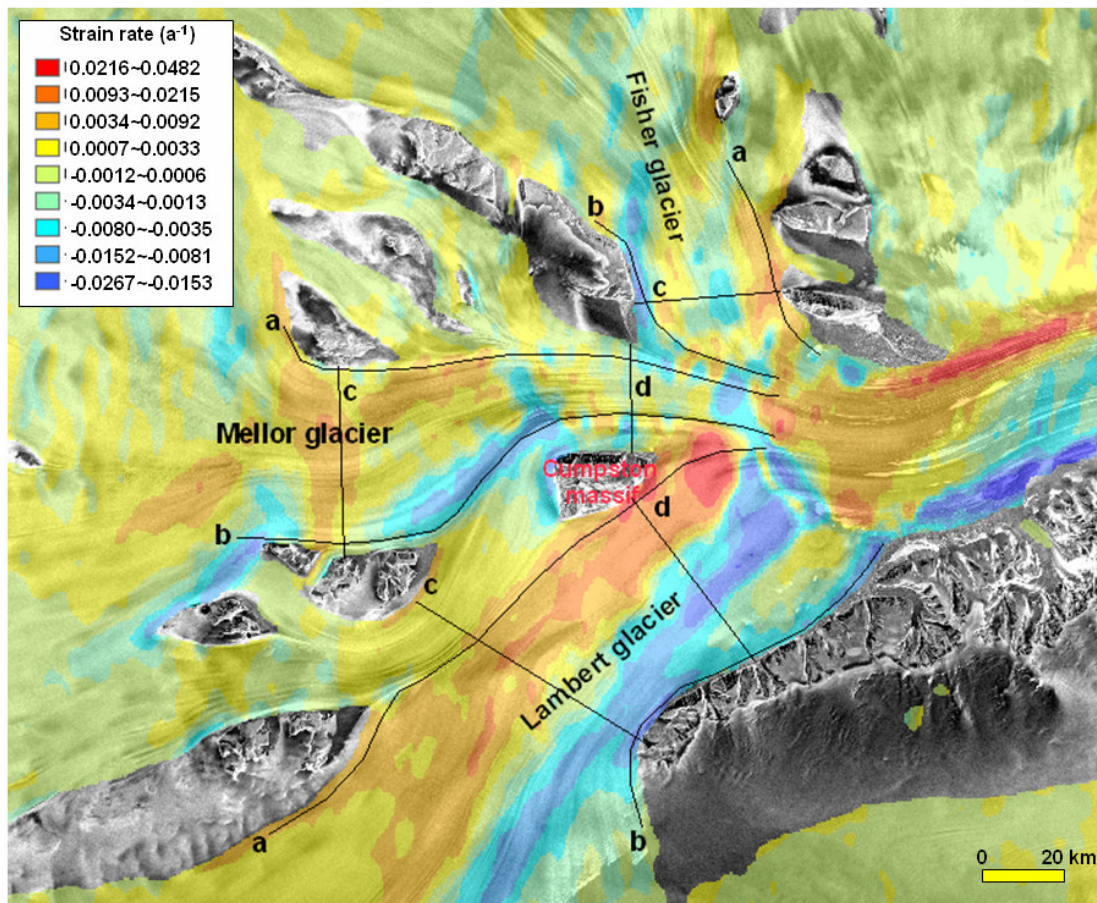
Figure 3.3 Lateral shear strain rate distribution of grounded ice flow of the Lambert,

Mellor and Fisher Glaciers. "a", "b", "c", and "d" in the Figure indicates the strain rate

profile lines for each glacier in the following Figures.
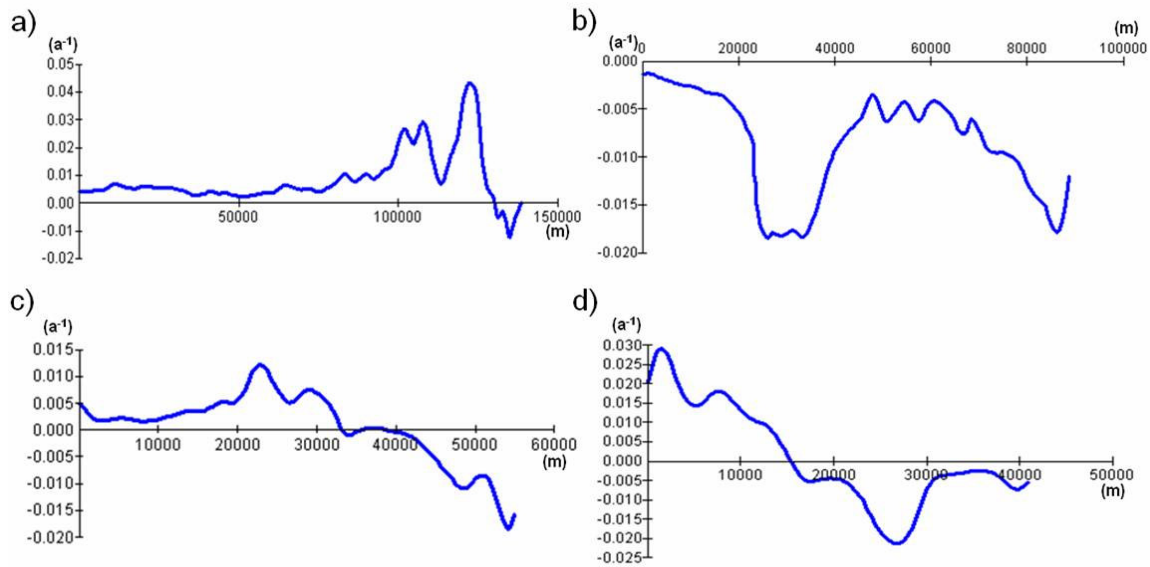
Figure 3.4 Longitudinal (a and b) and transverse (c and d) lateral shear strain rate profiles of grounded Lambert Glacier.

The east shear margin of Lambert Glacier exhibits a typical negative strain rate shear margin (Figure 3.3 b) caused by the fast moving glacier flowing away from the Mawson Escarpment. The strain rate dramatically decreases where the glacier flows away from Mawson Escarpment as the velocity increases, creating a high negative strain rate in the section between 20,000 m and 43,000 m. The three abrupt decreases after the section are the effect of small ice stream merging draining from the valley in the mountain area.

The transverse profile of the upstream area shows the typical trend of a high shear margin glacier created by ice flow merging in the western shear margin near 22,000 m and the flowing away effect from the mountain area in eastern shear margin

(Figure 3.3 c). The center area of the ice flow doesn't experience any noTable shear strains near 10,000 m and 38,000 m of the profile. However, the two extreme distributions along the profile are more exaggerated in the upstream region because of Cumpston Massif and the grounding line effect (Figure 3.3 d). The western shear margin shows high deformation where the ice flow moves in a high velocity towards Cumpston Massif. The center portion of the stream shows a negative strain rate distribution which is different from general trend of the strain rate distribution. This is caused by the velocity increase effect near the grounding line as well as the ice flow merging. It is concluded that the grounded ice flow of Lambert Glacier experiences a lot of dynamic ice variation and deformation because of the topographic and grounding line effects in addition to its fast movement.
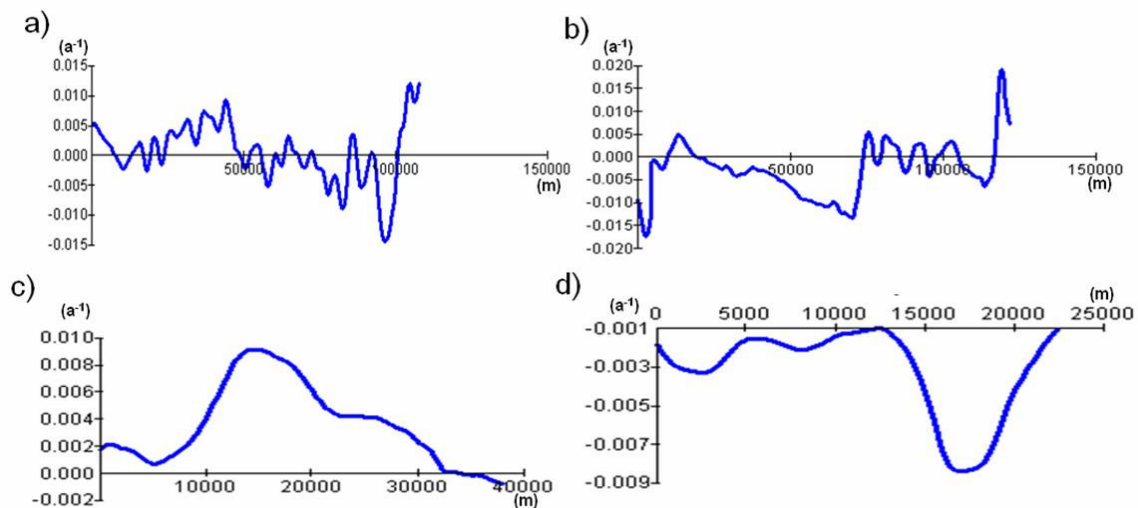


Figure 3.5 Longitudinal (a and b) and transverse (c and d) lateral shear strain rate profiles of grounded Mellor Glacier.

The grounded part of Mellor Glacier shows a more complicated distribution of strain rates (Figure 3.2). It exhibits high variations as the velocity varies with the ice flow merging experiencing the effects of three streams merging into one. The highest strain rate of 0.4048 a$^{-1}$ is detected at confluence area and the minimum of -0.0267 a$^{-1}$ near grounding line in the grounded ice flow of Mellor Glacier. The western longitudinal profile (Figure 3.4 a) starts with a positive strain rate as it passes by the rock exposure and drops to a negative strain rate as it flows away from the rock. The section between 15,000 and 50,000 m draws positive fluctuations in strain rate as it merges with two ice streams, and it decreases as a negative fluctuation because of the velocity increase effect. The minimum is detected near the grounding line where the velocity increase is highest. The eastern longitudinal profile shows negative strain rates and increases up to 0.005 a$^{-1}$ which can be explained by two neighboring mountains as the flow moves away from the small mountain and towards a larger mountain (Figure 3.4 b); decreases are attained in the 20,000 to 80,000 m section where the flow moves away from the mountain and the velocity increases until it gets to the confluence region.

The upstream transverse profile shows the highest positive strain rate distribution in the center and is lowest in the margins (Figure 3.4 c). This can be explained by velocity decrease as the flow width decreases with the ice flow merging in the downstream area. The downstream transverse profile has a negative strain rate trend with an abrupt decrease near 17,000 m (Figure 3.4 d). This region is the major area where the velocity increases as the width of the ice flow path is the smallest.

Fisher Glacier shows a similar trend as the other glaciers. The northern shear margin shows a negative strain rate distributions and the southern shear margin shows positive strain rate distributions. The highest strain rate of 0.0151 a$^{-1}$ is observed at the southern shear margin at the edge of Mt. Stinear, and the lowest of -0.0173 a$^{-1}$ at the northern shear margin in contact with the mountain. The longitudinal trend can be explained the same way as the other glaciers where the grounding line effect and shear margin effect of mountain area depends on the ice flow direction and velocity variation (Figure 3. 5 a, b, and c).
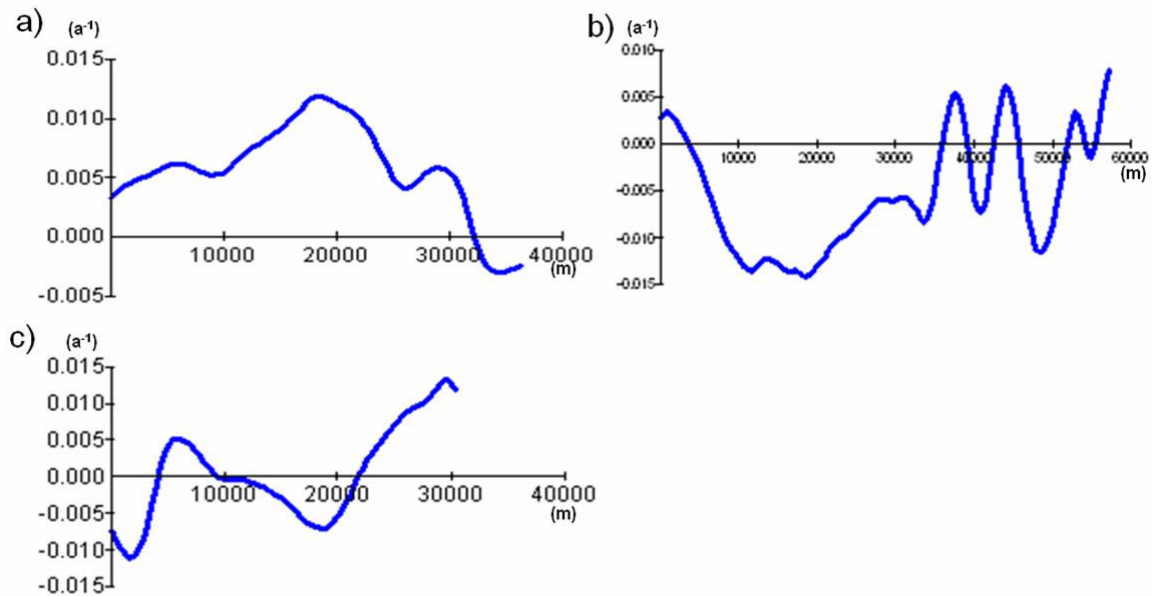


Figure 3.6 Longitudinal (a and b) and transverse (c) lateral shear strain rate profiles of grounded Fisher Glacier.

**3.3.2. Lateral shear strain rate distribution of the upstream area of Amery Ice Shelf and western and eastern tributary glaciers**

The upstream region of Amery Ice Shelf can be characterized by high shear strains on the stream margins and strain rate variations in center stream due to the grounding line effect, high average velocity, meander of the ice stream along the Mawson Escarpment, and tributary channel merging. Although not as complicated as grounded ice, the upstream region experiences high deformations through the entire stream (Figure 3.6). The highest lateral shear strain rate observed in the main ice shelf stream is $0.0403$ $a^{-1}$ where there is a stream merging from the western tributary glacier, and the lowest of $-0.0592$ $a^{-1}$ at the edge of Mawson Escarpment where the velocity increases away from the edge with flow direction changes. Three longitudinal profile lines are placed along each end of the shear margins and the center flow to observe the changes in the lateral shear strain rate of the upstream area (Figure 3.6).
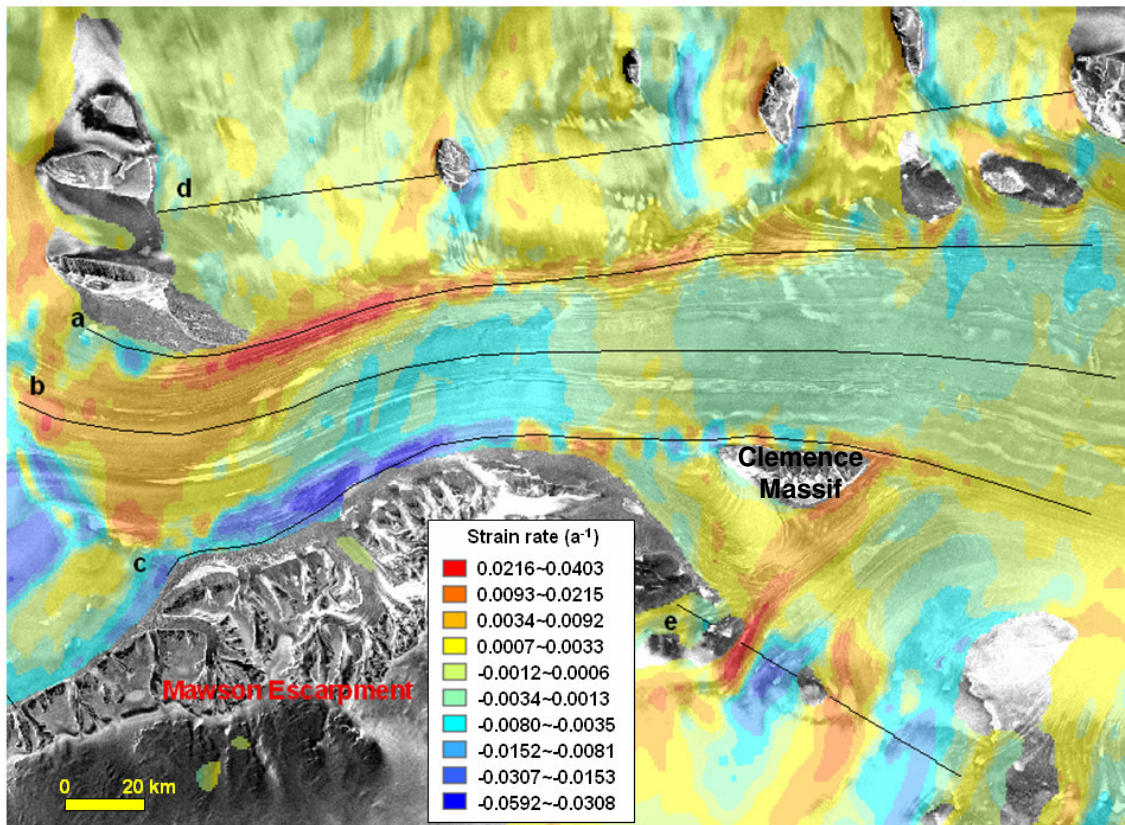
Figure 3.7 Lateral shear strain rate distribution in the upstream area of Amery Ice Shelf, western tributary glacier, and eastern tributary glacier. "a", "b", "c", "d" and "e" in the Figure indicate the strain rate profile lines in the following Figures. The pink line in the Figure represents the grounding line extracted from this study.

The western shear margin begins with a negative shear strain as it passes the grounding line and makes a turn into a shear margin which causes positive shear strain along the margin (Figure 3.7 a). Some of the abrupt increase on the profile near 50,000 m are noticable and can be explained by the tributary glacier facing the main ice stream.

Linear artifacts are observed along the ice stream and in the profile as jumps or drops which are caused by the orbital adjustment problem. The eastern shear margin shows the opposite trend of lateral strain rate from the western shear margin; i.e. the flow pattern creates the opposite strain field along the margin. However, the same positive jumps are observed when the tributary glaciers are merging and the ice flow is dividing which causes decreases in the ice velocity (Figure 3.7 c). The center portion does not experience any noticeable deformation once it gets away from the grounding line and the ice velocity decrease area at 50,000 m. Other than a few drops in strain rate from the orbital adjustment errors, the general pattern is plain and the variation range is minimal.

The western tributary channel shows no noticeable deformations on high elevation areas until it comes to the Prince Charles Mountain area, especially near the grounding line (Figure 3.6). The highest strain rate of 0.0137 $a^{-1}$ is detected at the northern margin of Shaw Massif and the lowest strain rate of -0.0160 $a^{-1}$ at southern edge of Shaw Massif. The transverse strain rate shows dramatic changes at the sides of the mountains (50,000 m, 100,000 m and 150,000 m) (Figure 3.7 d). The eastern tributary glacier shows a maximum of 0.0335 $a^{-1}$ near the rock exposure where the velocity decreases and a minimum of -0.0224 $a^{-1}$ where the velocity increases. Both western and eastern tributary glaciers make good example of the topographic effects of alternative bands of positive and negative shear strain rates (Figure 3.7 d and e). However, the general magnitude of the strain rate is smaller than the main ice streams because of slower ice stream movement.
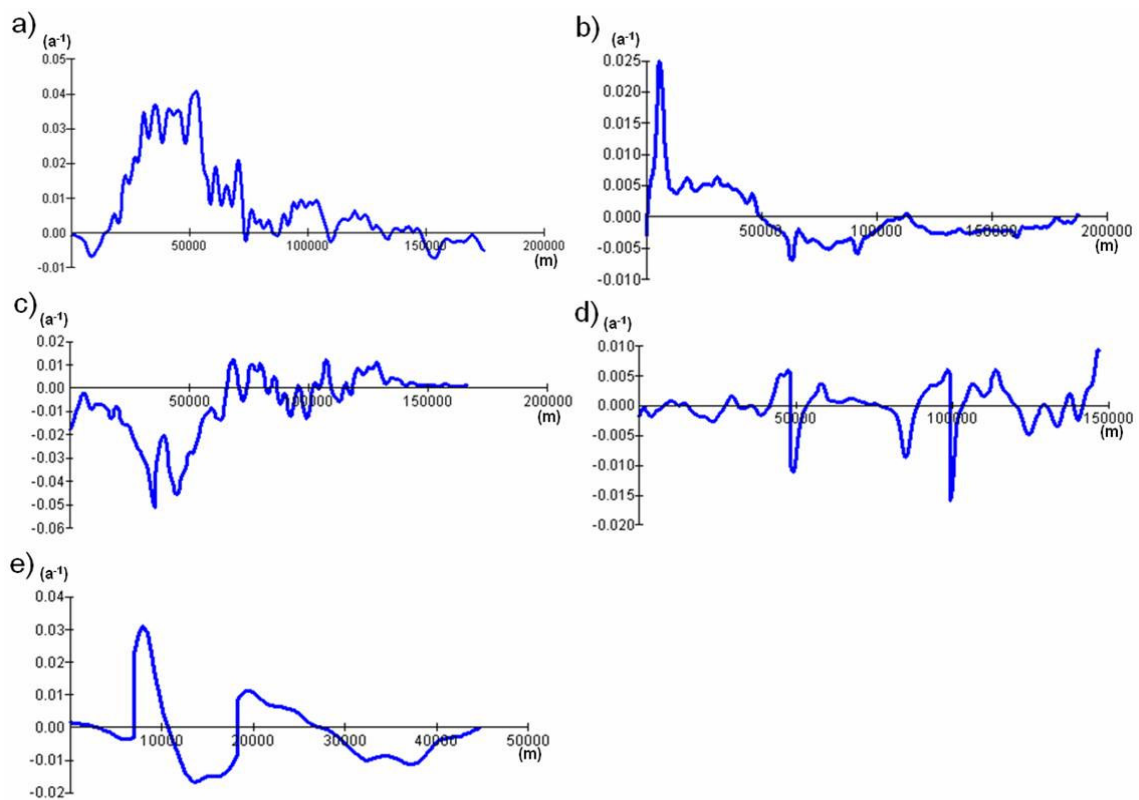
Figure 3.8 Longitudinal ((a), (b), and (c)) lateral shear train rate profiles of upstream area of Amery Ice Shelf, and transverse ((d) and (e)) lateral shear strain rate profiles of western and eastern tributary glaciers in Amery Ice Shelf upstream region.

### 3.3.3. Lateral shear strain rate of downstream area of Amery Ice Shelf and eastern tributary glacier

The main ice stream of the downstream area of Amery Ice Shelf shows a more stable ice flow pattern as it flows in a relatively constant direction and the path of the ice stream increases (Figure 3.8). As a result, the deformation in the center flow is almost zero and the shear margin is narrow except for the tributary glacier merging area. The highest and lowest values are observed at the eastern tributary merging area with the values of $0.0174$ $a^{-1}$ and $-0.0177$ $a^{-1}$ respectively.

The longitudinal profile of the western shear margin shows a major positive lateral shear margin along the Jetty Peninsula (Figure 3.9 a) between 45,000 m and 123,000 m. The major drops at 130,000 m can be explained by the flow away effect from the edge of the peninsula. After 140,000 m, the profile becomes the transverse profile of the ice flow from the Charybdis Glacier area. As mentioned in the beginning of the paragraph, the center flow of the main ice stream shows minimal deformations which range less than $0.001$ $a^{-1}$ in both positive and negative fields except for the error peaks from orbital adjustment (Figure 3.9 b). The eastern shear margin shows some variations near the tributary glacier merging area, but these are generally minimal deformations because of the relatively wider channel and gentle flow direction (Figure 3.9 c). The transverse shear strain rate distribution shows how stable the ice stream is through its width. Except for the high peak western shear margin at Jetty Peninsula, about 80% of the width shows the plain strain rate near $0$ $a^{-1}$ (Figure 3.9 d).

The eastern tributary glacier shows the effect of topographic variations very well. Since the surface topography has many rock exposures and protrusions, it hampers and changes ice flow movement and causes alternative variations in lateral shear strain rate (Figure 3.8). This causes high magnitudes of lateral shear strain rate ranges from -0.0621 $a^{-1}$ to 0.0542 $a^{-1}$. The transverse strain rate profile confirms the effect (Figure 3.9 e). Dramatic changes from positive to negative lateral shear strain rate change are detected by the physical barrier of rock exposures. Once it gets out of the topographic effect area it shows the typical ice stream strain rate distribution (Figure 3.9 f).

### 3.3.4. Lateral shear strain rate of Charybdis Glacier area

The area upstream of Charybdis Glacier and Scylla Glacier shows a plain shear strain distribution down to the merging area since the flow direction is constant and parallel to the valley wall direction, and velocity change through the ice stream is minimal (Figure 3.10). These are the same characteristics as the downstream area of the main ice stream. The longitudinal profiles of these glaciers are not necessary as they show the same pattern that was described before. However, there are complicated patterns of strain rate as it gets to the discharging area. The complication is mainly caused by 8 ice streams merging into one in addition to topographic variations of rock exposures (Figure 3.10). The transverse profile from upstream to downstream shows the same general trend of the merging area (Figure 3.11 a, b, and c). As small streams merge into each other, the lateral shear strain rate shows a lot of fluctuations in relatively small magnitudes (Figure 3.12 a). As they merge into each other, four major merged ice streams fewer peaks but higher magnitudes (Figure 3.12 b). Once they merge into one ice stream, they show the

effects of merging at the beginning (Figure 3.12 c), but with the typical characteristics of the ice stream of one edge in positive and the other in negative (Figure 3.9 a and Figure 3.10). The highest strain rate is observed at the major merging area of 0.0287 $a^{-1}$ and the lowest of -0.0196 $a^{-1}$ near the same area.
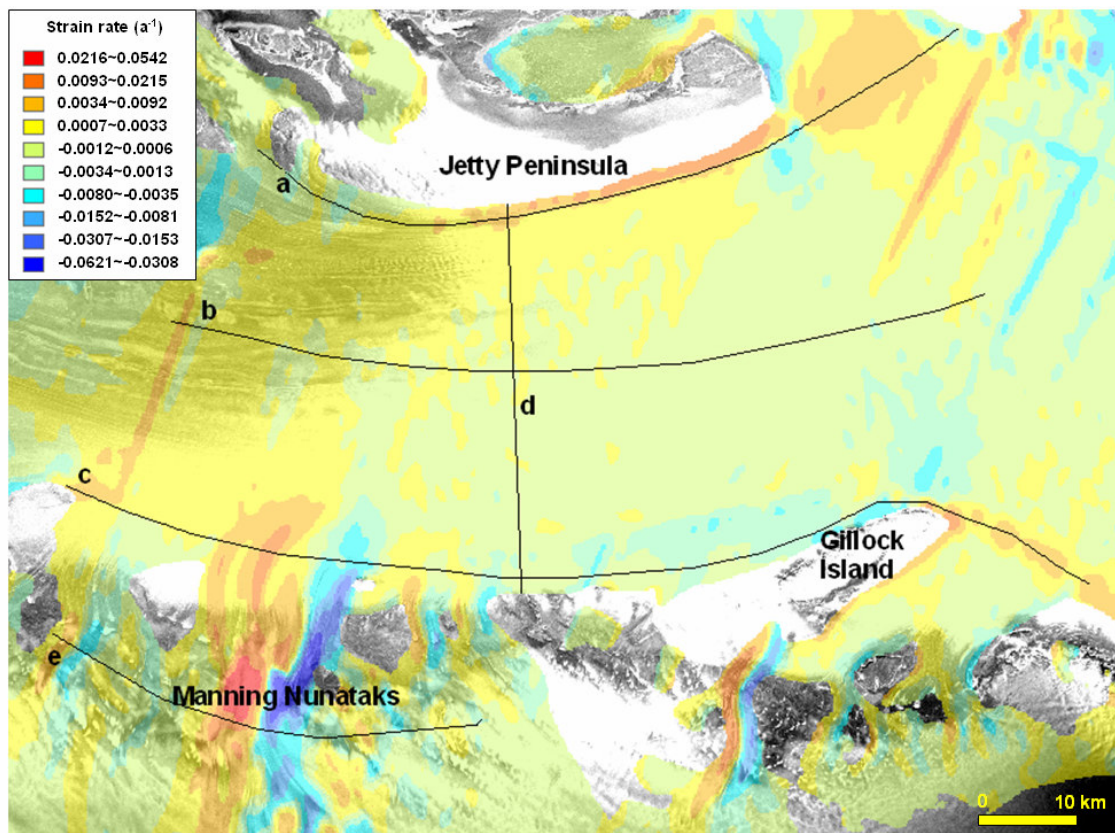


Figure 3.9 Lateral shear strain rate distribution of the downstream area of Amery Ice Shelf and the eastern tributary glacier. "a", "b", "c", "d", "e", and "f" in the Figure indicate the strain rate profile lines in the following Figures. The pink line in the Figure represents the grounding line extracted from this study.
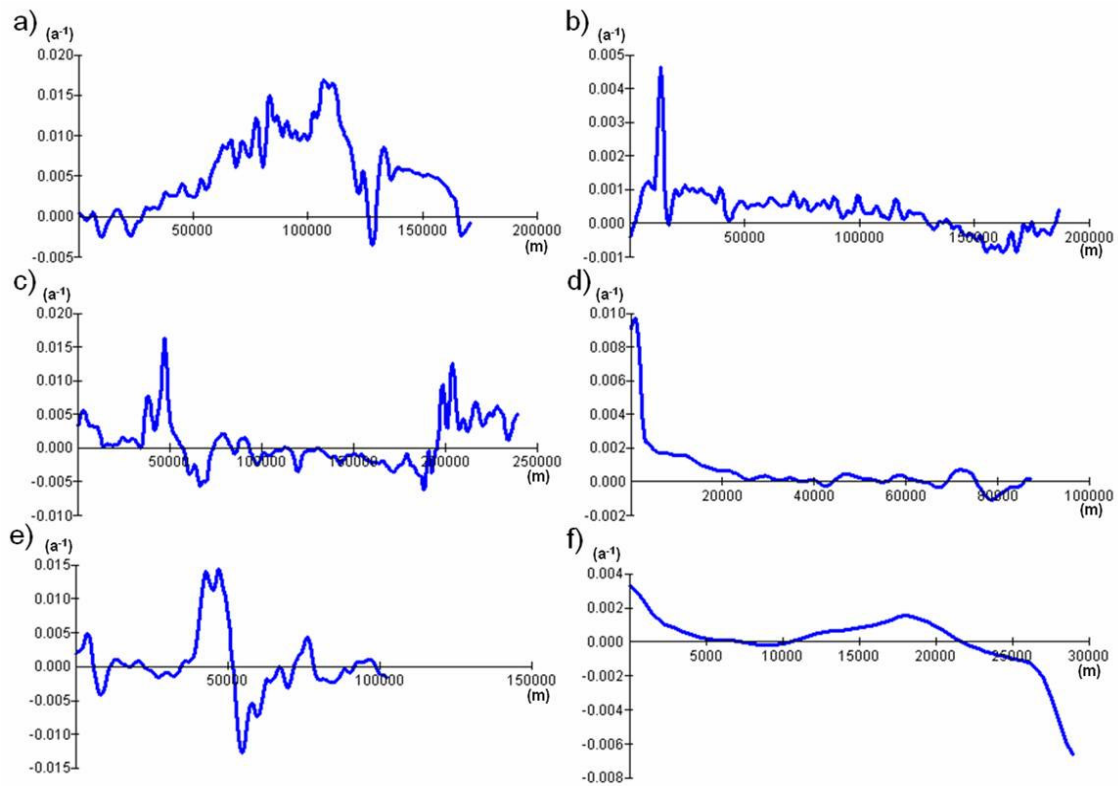
Figure 3.10 Longitudinal (a, b, and c) and transverse (d) lateral shear strain rate profiles of the downstream area of Amery Ice Shelf, and transverse (e and f) lateral shear strain rate profiles of the eastern tributary glaciers in Amery Ice Shelf downstream region.
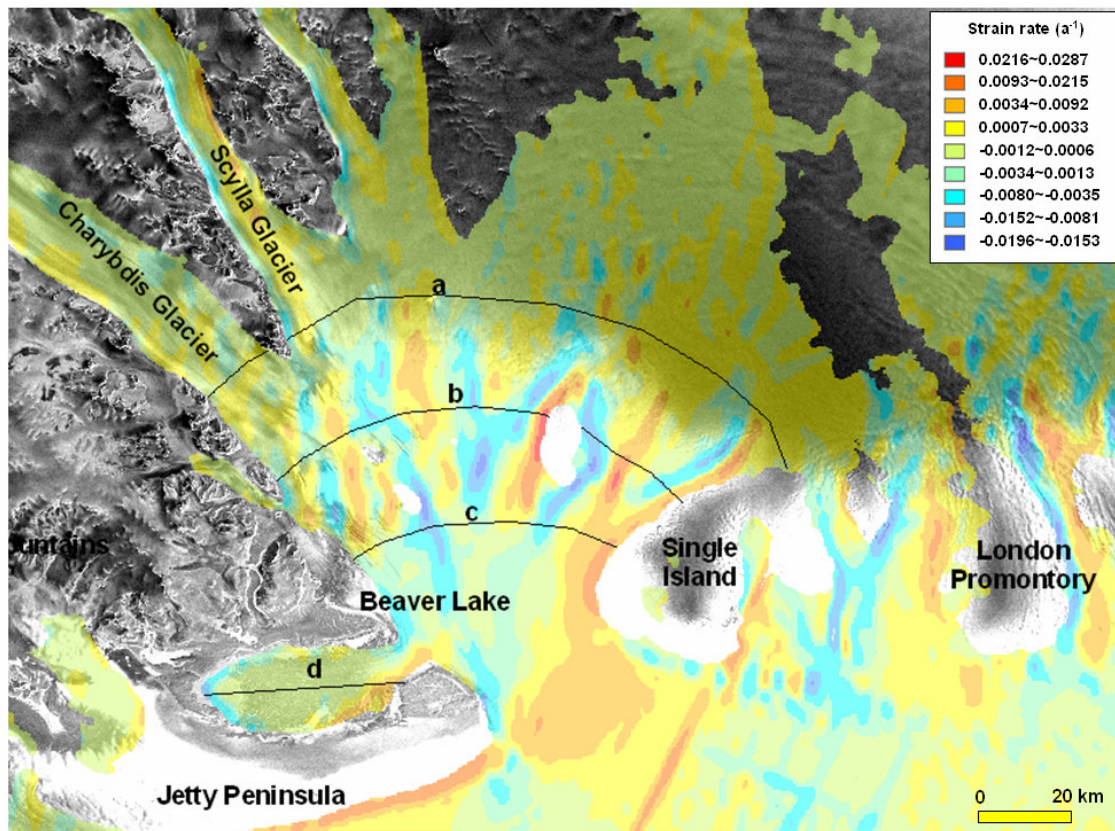
Figure 3.11 Lateral shear strain rate distribution of the Charybdis Glacier and Beaver Lake area. "a", "b", "c", and "d" in the Figure indicate the strain rate profile lines in the following Figures. The pink line in the Figure represents the grounding line extracted from this study.
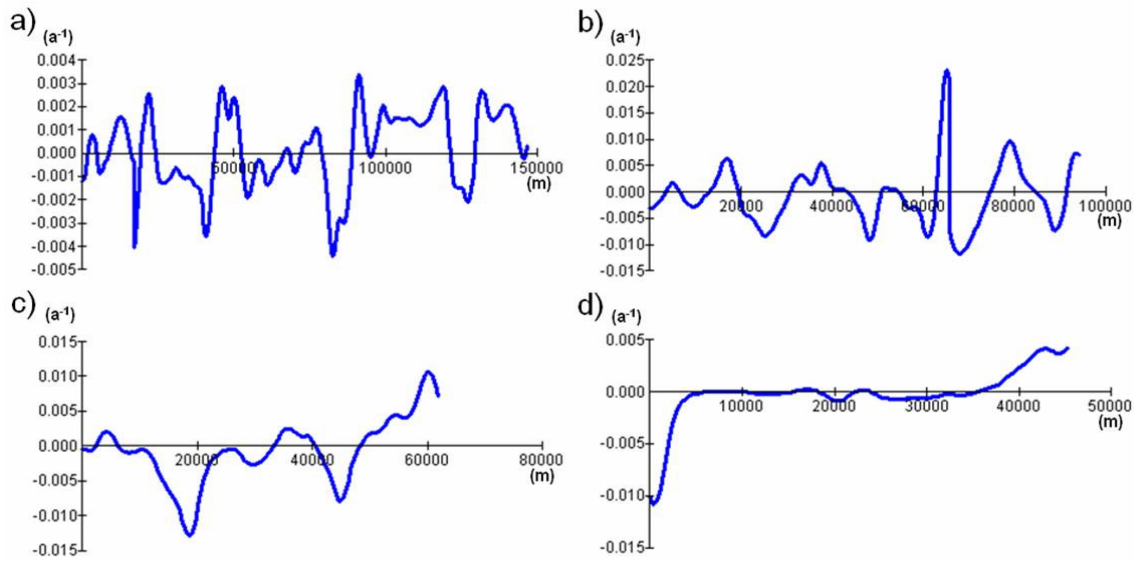
Figure 3.12 Transverse lateral shear strain rate profiles of the Charybdis Glacier area (a, b, and c) and Beaver Lake (d) area.

## 3.4. Spatial pattern and trend of strain rate

The lateral shear strain rate effectively tells the story of the ice deformation distribution over the glaciers. The values of the shear strain rate can imply internal properties. The high strain rate causes heating distributed over the ice thickness, and it results in significant horizontal temperature gradients out of the shear margins (Young and Hyland 2002, Harrison *et al.* 1998). The strain rate distribution shows close relationships to the ice flow direction, ice flow velocity, and surface features. When the glacier flows towards mountains, it creates negative strain rates. Generally, the ice flow shows the characteristics of compressive flow. On the other hand, it is showing positive strain rates when the glacier flows away from the mountains; and the ice flow shows the characteristics of extending flow. From the characteristics, it is safe to say that the high

positive strain rate area experiences ice thinning and the high negative strain rate area experiences ice thickening.

The computation results show that the major ice stream channels and their confluence zones are experiencing strong deformations. The strain rate variation is dominant in transverse direction, compared with the longitudinal direction of the glacial channels. The high strain rate in the shear margins has significant impacts on the internal properties of the glaciers. The strain heating within the shear margins can raise the temperature of the core of the shear margins, leading to significant horizontal temperature gradients out of the margins (Harrison *et al.* 1998). The strain rate varies along the longitudinal direction of the Amery Ice Self. Above or near the grounding zone, the velocities of the three main glaciers (the Lambert, the Mellor, and the Fisher) are increasing in the downstream direction, resulting in positive strain rate and extensive deformation. At the confluence zone and upper stretch of the ice shelf, the strain rate is positive, causing compressive deformation. This is confirmed by visually examining the SAR image and InSAR coherence image for this region. In the middle stretch of the ice shelf, not much velocity change is detected in the longitudinal direction, meaning not much longitudinal deformation. At the front of the ice shelf, significant positive strain rate values imply the extensive deformation. This may contribute to the development of longitudinal rifts and crevasses, and hence influence ice berg calving process.

## CHAPTER IV

## GROUNDING LINE DETERMINATION

### 4.1. Definitions

The grounding line is a transitional area separating inland ice from the ice shelf (Weertman 1974). On the ice shelf, the floating ice is the major area of mass loss from the Antarctic ice sheet, via iceberg calving and basal melting (Jacobs *et al.* 1992).

Increased basal melting may cause increased strain rates near the grounding zone and it allows the ice stream to thin and flow more rapidly (Budd and Warner 1998). The horizontal location of the grounding zone is sensitive to changes in ice thickness and sea-level (Stephenson 1984) and it is an important indicator of the dynamic state of the ice stream. Since the grounding line may migrate in response to changes in ice thickness and sea level, accurate delineation of the position and shape of the grounding zone of a glacier-ice shelf system is critical to asses possible changes in ice sheet dynamics; the mass flux entering an ice shelf though the grounding line can be an indicator of an ice stream dynamics, basal conditions, mass balance, and accumulation rates. In addition, the location of the grounding zone provides essential information for describing the basal conditions for an assessment of the ice dynamics, for inclusion in numerical models of the ice flow, and for an assessment of ice-ocean interaction (Fricker *et al.* 2002).

The Amery Ice Shelf is the largest ice shelf in East Antarctica. It drains the grounded portion of the Lambert Glacier-Amery Ice Shelf system, which accounts for 16

% of the area of the grounded East Antarctic ice sheet (Fricker *et al.* 2000). The Lambert, Mellor, and Fisher Glaciers flow through the grounding line of the Lambert Glacier system; it has been well studied as one of the main components of ice mass discharging into Amery Ice Shelf. However, significant mass from tributary glaciers and Charybdis Glacier is contributed into Amery Ice Shelf and the grounding lines and mass flux from these glaciers has not received much attention compared to fluxes and grounding lines from the three largest glaciers. Furthermore, the grounding line delineated recently for the region (Fricker *et al.* 2002) has limited accuracy since it is based on the hydrostatic calculation using surface elevations. This study derives a more accurate grounding line along the whole Amery Ice Shelf perimeter based on a combination of SAR interferometry and hydrostatic calculation of elevation.

This chapter describes previous studies of the grounding line for the Lambert-Amery system, the details of methodology, and the grounding lines of the Lambert system, tributary glaciers, and Charybdis Glacier.

Until a more recent grounding line location was verified from various studies (Ficker *et al.* 2002, Rignot 2002), the location of the grounding zone of the Lambert-Amery system from Budd et al. (1982) has been generally accepted. They inferred that the grounding-floating transition occurs around 71.2 °S coinciding with a maximum surface slope near Pickering Nunatack. This location was based on the data collected during a theodolite and electronic distance measurement survey (EDM) of the ice shelf by the Australian National Antarctic Research Expedition (ANARE) in 1968-70 (Budd *et al.* 1982).

This grounding line location has been questioned by several subsequent studies. Robin (1983) suggested the grounding zone would need to be further south based on a single ice core at 69.451°S, 71.497 °E and Radar Echo Sounding (RES) data; Drewry and Robin (1983) also suggested that ice between 300 and 500 km from the Amery ice front  mainly afloat on the basis of RES data from Morgan and Budd (1975).  Bentley (1987) also noted that the lower 180 km section of the Lambert Glacier shows more likely the ice dynamic characteristics of an ice shelf than an ice stream. In addition, visual interpretations from satellite data supported the further south location of the grounding zone (Swithinbank 1988, Hambrey and Dowdeswell 1994). However, no conclusive quantitative evidence has been previously presented to contradict the location of Budd *et al.* (1982). Based on hydrostatic equilibrium, Fricker *et al.* (2002) determined that the grounding-line position was located some 200 km upstream from the grounding line from Budd *et al.* (1982). Their analysis, however, could not locate the grounding line position better than within several km. Rignot (2002) utilized InSAR data to delineate the grounding line for the portion of system. He delineated only half of the grounding line of the Lambert/Mellor/Fisher system from InSAR due to a lack of InSAR coverage. The grounding line position was determined using a topographic map, the boundary of narrow interferometric fringes, and the map of the difference in ice velocity between ERS InSAR and RADARSAT speckle tracking. This work established the confluence of Lambert/Mellor/Fisher Glacier as the grounding line of the Lambert-Amery system.

Although the grounding line position of the confluence of main three glaciers has been actively studied, grounding line position for the tributary glaciers of the Amery Ice Shelf is limited. Fricker *et al.* (2002) delineated the grounding line location for the Amery Ice Shelf based on the hydrostatic calculation. However, their study focused on describing the grounding line position of main glacier region. The grounding line position is very important in mass balance calculation in terms of flux gate location, and the grounding line position of tributary glaciers should not be ignored in a comprehensive mass balance study. In addition, the computed location of grounding line from Fricker *et al.* (2002) most likely detects the stable floating point of the ice shelf which is located more downstream on the ice shelf than real grounding line position. The limitations of the method create uncertainty in the grounding line location. The studies of the main grounding line position has provided the clue of grounding line migration because the more recent study claims the more southward location of grounding line. Fricker *et al.* (2002) confirmed the southward extension of the grounding line position. The result of this study provides the supporting evidence of grounding line migration.

## 4.2. Grounding line identification methods

Because the grounding line is the transition zone of inland ice and floating ice, it experiences both vertical movement of floating ice and differential horizontal movement between grounded ice and floating ice. Interferometric SAR processing has been used as an effective tool in identification of the grounding line in numerous areas (Goldstein *et al.* 1993, Rignot 1996, Gray *et al.* 2002). In addition, the hydrostatic height anomaly

(the difference between the measured surface height and the surface height calculated from measured ice thickness) can be used to identify floating ice (Ficker *et al.* 2001).

### 4.2.1. Hydrostatic calculation of elevation

The relationship between the surface height H (relative to sea level) and the ice thickness Z at any point is given by the hydrostatic equation:

$$H = \frac{Z(\rho_w - \rho_i)}{\rho_w}$$  (4.1)

where $\rho_w$ and $\rho_i$ are the column-averaged densities of sea water and ice respectively. The hydrostatic anomaly ($\delta h'$) is defined as the difference between the measured surface height and the surface height calculated from the measured ice thickness using the equation.

$$\delta h' = \bar{h} - \frac{Z(\rho_w - \rho_i)}{\rho_w}$$  (4.2)

Since the grounding line is a transition area between inland ice and floating ice, $\delta h'$ is significant for grounded ice or where there are errors in the total ice thickness or density values (Fricker *et al.* 2001). This study used recent surface height data obtained from the ICESat laser altimetry data (Zwally *et al.* 2003). The Geoscience Laser Altimeter System (GLAS) instrument on the Ice, Cloud, and land Elevation Satellite (ICESat) provides global measurements of polar ice sheet elevation to discern changes in ice volume over time. The 1062 nm laser channel produces surface altimetry with 183-day repeat cycles. The separation between the tracks is about 15 km. The height measured

from laser altimeter is expected to be the precision of better than 10 cm (Zwally *et al.* 2002). However, the preliminary laser altimetry data used by this study has limited accuracy of 1.5 m (Zwally *et al.* 2003).

BEDMAP ice thickness data (Lythe *et al.* 2000) is utilized for the hydrostatic calculation of ice thickness. The major source of the BEDMAP ice thickness are airborne Radio Echo Sounder by the Russian Polar Marine Geological Reseach Expedition (PMGRE) over seven field seasons between 1986 and 1995 (Fricker *et al.* 2001). The 5 km original BEDMAP ice thickness grid is resampled into 1 km grids using bilinear interpolation. The vertical accuracy of the ice thickness for the Amery Ice Shelf area is expected to be 50 m with the distance between RES flightlines around 5 km. Fricker *et al.* (2001) derived the column-averaged ice density from a density model which has two layers of meteoric ice to account for a firm layer plus a marine ice layer at the base of the shelf. The column-averaged ice density ranges 860 Kg m$^{-3}$ at the calving front to 921 kg m$^{-3}$ near the grounding line of the Lambert Glacier (Figure 4.1). The column-averaged density of the sea-water displaced by the ice shelf was taken as 1029 kg m$^{-3}$, based on measurements off the ice shelf front (Wong et al., 1998).
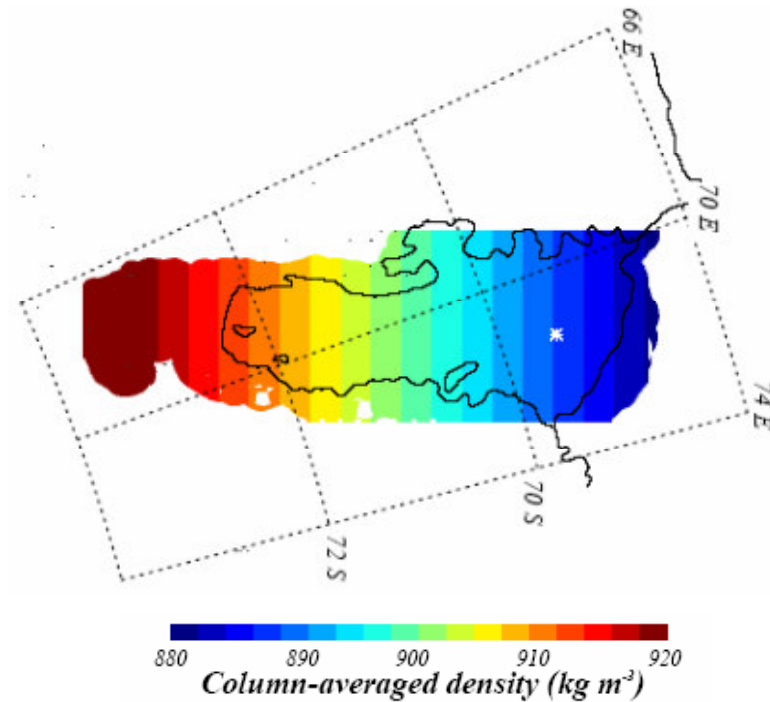
Figure 4.1 Simple linear model for the column-averaged ice density of the Amery Ice Shelf (Fricker, 1999).

## 4.2.2. SAR Interferometry

The vertical velocities increase abruptly at grounding lines. Due to the vertical movement of floating ice and differential horizontal movement between grounded ice and floating ice, interferometric fringes change sharply with a high gradient at the grounding line. Fringes are lost or abrupt, coherence estimates are reduced when the phase is changing rapidly; this is because the phase will change over the window used to calculate the coherence. In this way coherence images can be complementary to the phase-gradient images in estimating the position of the grounding zones (Gray *et al.*

2002). This study used the interfeometry coherence image and vertical velocity from repeat-pass SAR interferometry from the Antarctic Mapping Mission-2 (Jezek 2003) to identify the location of the grounding line.

## 4.3. Grounding Line of the Lambert Glacial Basin

Because of the characteristic features of grounding lines, coherence images can be used to accurately map the location of the grounding line. However, the 24 day repeat orbit of RADARSAT can be a disadvantage if there is a large velocity gradient across the grounding line, because there can be a loss of coherence. In this case, information such as topography and ice velocity must be used to estimate the grounding line position. However, if coherence is maintained across the grounding zone then the 24 day image separation can be an advantage since the height difference of floating ice because two of the main tidal constituents, M2 (period: 12.42 hours) and O1 (period: 25.82 hours) are much larger for the 24 day pass separation since it increases the vertical movement between the pairs (Gray *et al.* 2002). This study utilizes coherence images of an ascending pass of AMM-2 (Jezek 2003) as a main constraint to delineate the grounding lines of glaciers discharging into Amery Ice Shelf (Figure 4.2).

Figure 4.2 Coherence image of Radarsat SAR interferometry.

Since most of ice streams flow down slope as they pass through the grounding line, the vertical velocity of the slope shows negative vector flowing downward flow; when the ice stream floats at the grounding zone, the negative velocity gradient changes into a positive gradient because the direction vertical velocity vector upward. Therefore, the vertical velocity component (Vz) can be an alternative choice to support a coherence image. However, it is necessary to differentiate the change in velocity gradients because of surface slope change and because of a floating ice stream. This study used vertical velocity components as a second constraint to delineate the grounding line overlaid on SAR magnitude images to distinguish surface glacier features (Figure 4.3). In addition, a velocity magnitude image is very effective in delineating glacier flows that can be used

to delineate glacier margins if the margin in the coherence image is too wide to delineate.
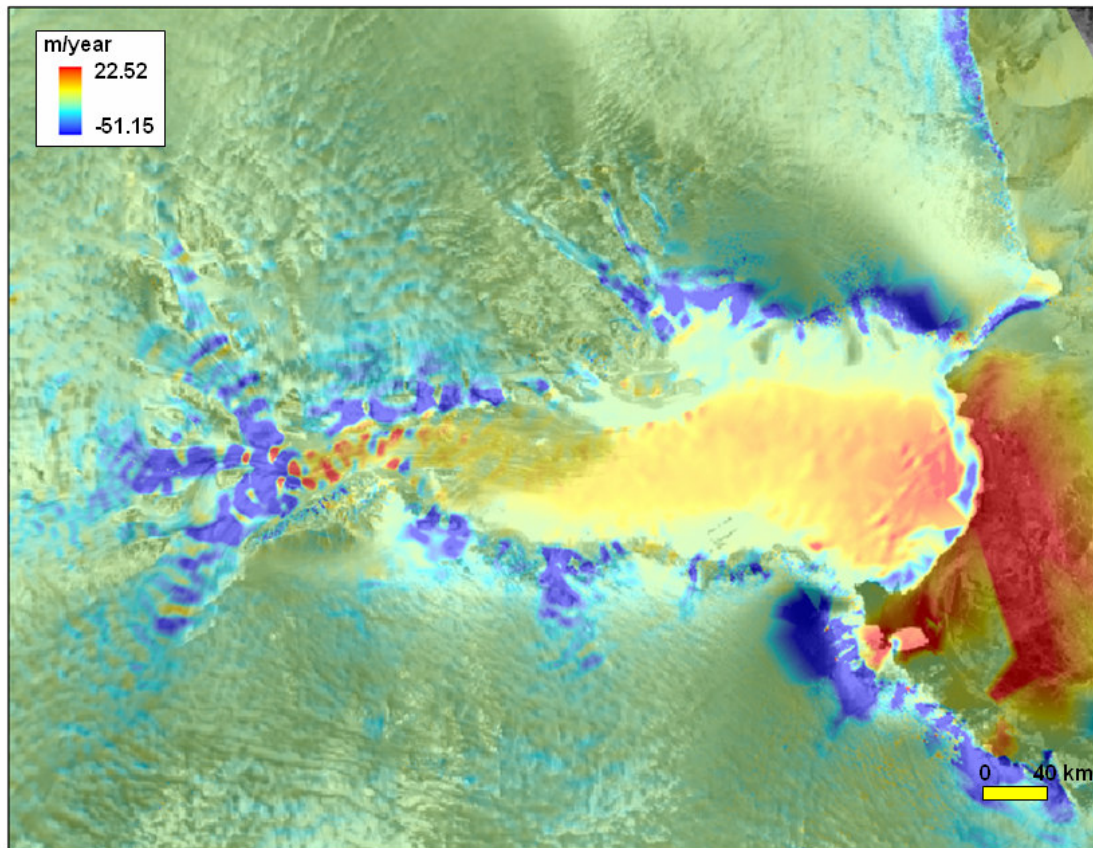


Figure 4.3 Vertical velocity component from Radarsat SAR interferometry.

The grounding line delineated from this study is subdivided into 5 main glacier regions around Amery Ice Shelf; the Lambert Glacier system, the western tributary glaciers, the Charybdis Glacier area, the eastern tributary glaciers, and the eastern tributary glaciers near Reinbolt Hills (Figure 4.4). The grounding line extraction and

pattern are discussed in terms of coherence, surface features, surface velocity, and vertical velocity components in the following.
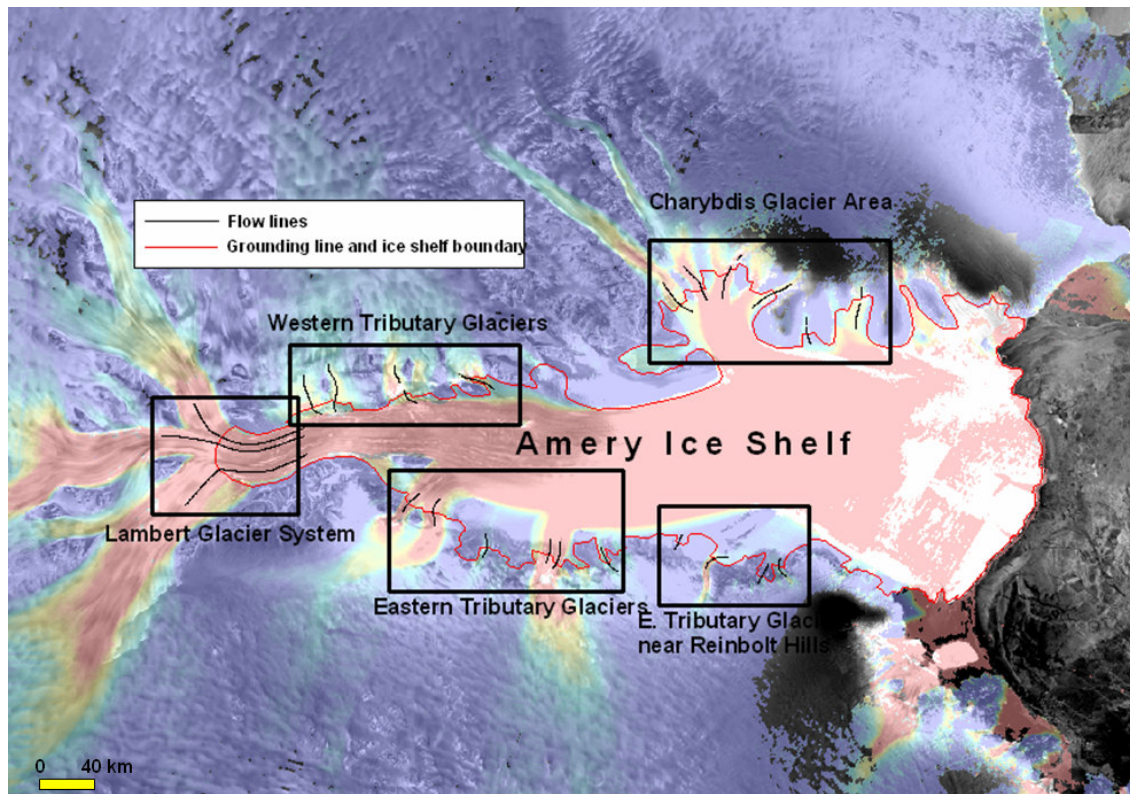


Figure 4.4 Five main glacier regions overlaid on grounding line and flow lines.

### 4.3.1. Lambert Glacier system grounding line

The Lambert Glacier system grounding line defines the south end of Amery Ice Shelf. In other words, the main ice stream consisting of Fisher, Mellor, and Lambert Glaciers begins floating from that point. Because of its glacial characteristics of fast movement caused by ice stream merging and floating ice, SAR interferometry fails in coregistration and phase unwrapping (Figure 4.5 b and c). SAR images show there is an abrupt slope

change where Fisher, Mellor and Lambert Glaciers converge, and it can be an alternative hint to give the location of the grounding line (Figure 4.5 a). Coherence images, because of the failure in phase unwrapping, indicate the grounding zone is 24 km long in the N-S direction near 67°E and 73.5°S. Vertical velocity components from SAR interferometry show similar patterns.



Figure 4.5 The SAR image (a), coherence image (b), vertical velocity (c), and surface velocity map (d) of Lambert Glacier system grounding line area. Red colors represent high velocity areas and blue colors represent low velocity areas for velocity maps (c) and (d).

To support the grounding line from the SAR image, this study mosaiced velocity information from speckle tracking for the ice convolution area (Figure 4.6 d). Increased basal melting may lead to increased strain rates near the grounding zone, allowing the ice stream to flow more rapidly (Budd and Warner 1998). Three flows lines were placed to detect the grounding line location from ice velocity profiles, one from each glacier (Figure 4.6). The red line in Figure 4.6 indicates the grounding line position determined from this study.

The velocity profile for each glacier confirms the grounding line location from the SAR image (Figure 4.6). The velocity of Fisher Glacier increases from 193 m/year to 580 m/year at the grounding line (Figure 4.7 a). The velocity of Mellor Glacier shows a positive velocity change of 300 m/year from the beginning of the flow line (390 m/year) to the grounding line location (688 m/year) (Figure 4.7 b). Lambert Glacier draws the highest velocity on the grounding line with 780 m/year which increased from 420 m/year at the beginning of flow line (Figure 4.7 c). The grounding line derived from the SAR image and surface velocity filed is positioned at E 66.62° and S 73.18° for Fisher Glacier, E 66.82° and S 73.27° for Mellor Glacier, and E 67.33° and S 73.3° for Lambert Glacier.
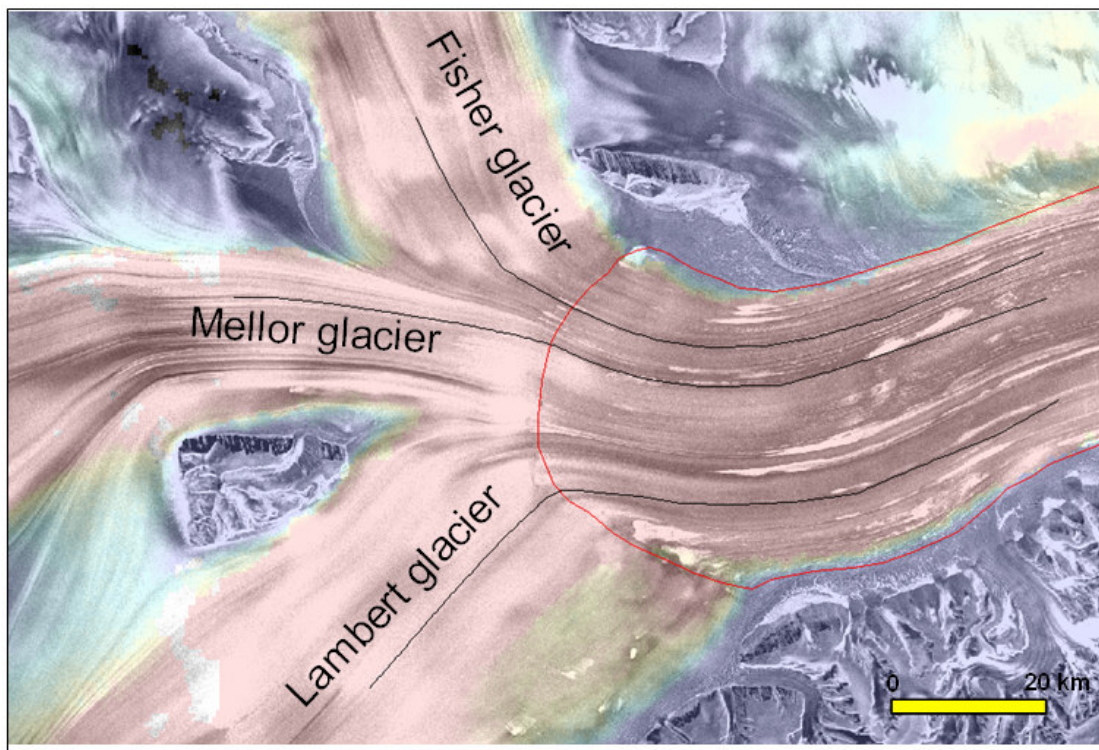
Figure 4.6 Flow lines from Fisher, Mellor, and Lambert Glaciers for velocity profile.
Red line indicates the grounding line from this study.
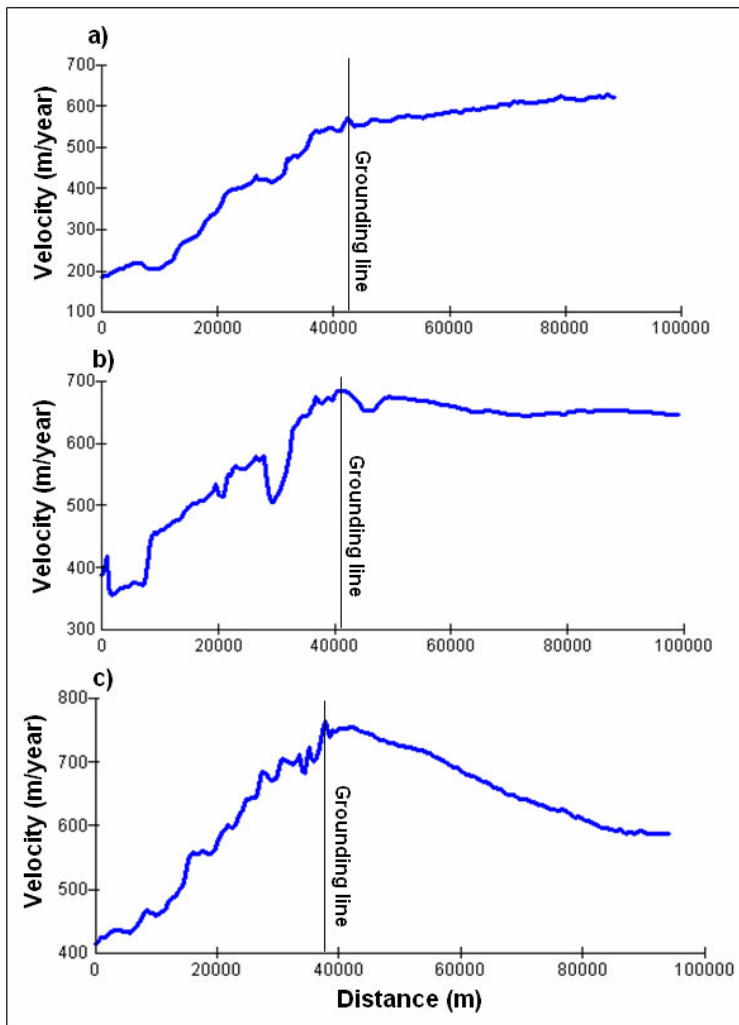
Figure 4.7 Surface velocity profile of Fisher (a), Mellor (c), and Lambert (c) Glaciers.

## 4.3.2. Tributary glaciers on the west part of Amery Ice Shelf

Five main ice streams discharge into the west portion of Amery Ice Shelf from the Prince Charles Mountains along the 350 km section from Mt. Stenear to Fisher Massif (Figure 4.8 a and d). The surface velocity of the five tributary channels ranges from 70 to 180 m/year along the grounding line leading to a significant ice mass discharge into Amery Ice Shelf (Figure 4.8 d). The location of the grounding line is well distinguished

at the downstream edge associated with the low coherence (Figure 4.8 b and Figure 4.9 e). The grounding line defined by the coherence image well matches with the change in the vertical velocity component (Figure 4.9 c and Figure 4.9 e).

Four flow lines are placed to determine the grounding line position for the western tributary glaciers (Figure 4.9 e). Flow line "a" shows a vertical velocity increase from -5 to 0.5 m/year between minimum and maximum at the grounding line (Figure 4.9 a). The vertical velocity of flow line "b" increases from -3.5 m/year to 1 m/year at the grounding line (Figure 4.9 b). The vertical velocity of flow line "c" shows a positive velocity change of 4 m/year from the minimum value of the flow line (-3.8 m/year) to the grounding line location (0.2 m/year) (Figure 4.9 c). The vertical velocity profile of flow line "d" draws the highest velocity on the grounding line of 0 m/year which increased from -4.5 m/year at the beginning of the flow line (Figure 4.9 d). As the profiles shows, our grounding line position matches with the low coherence boundaries and high vertical velocity.

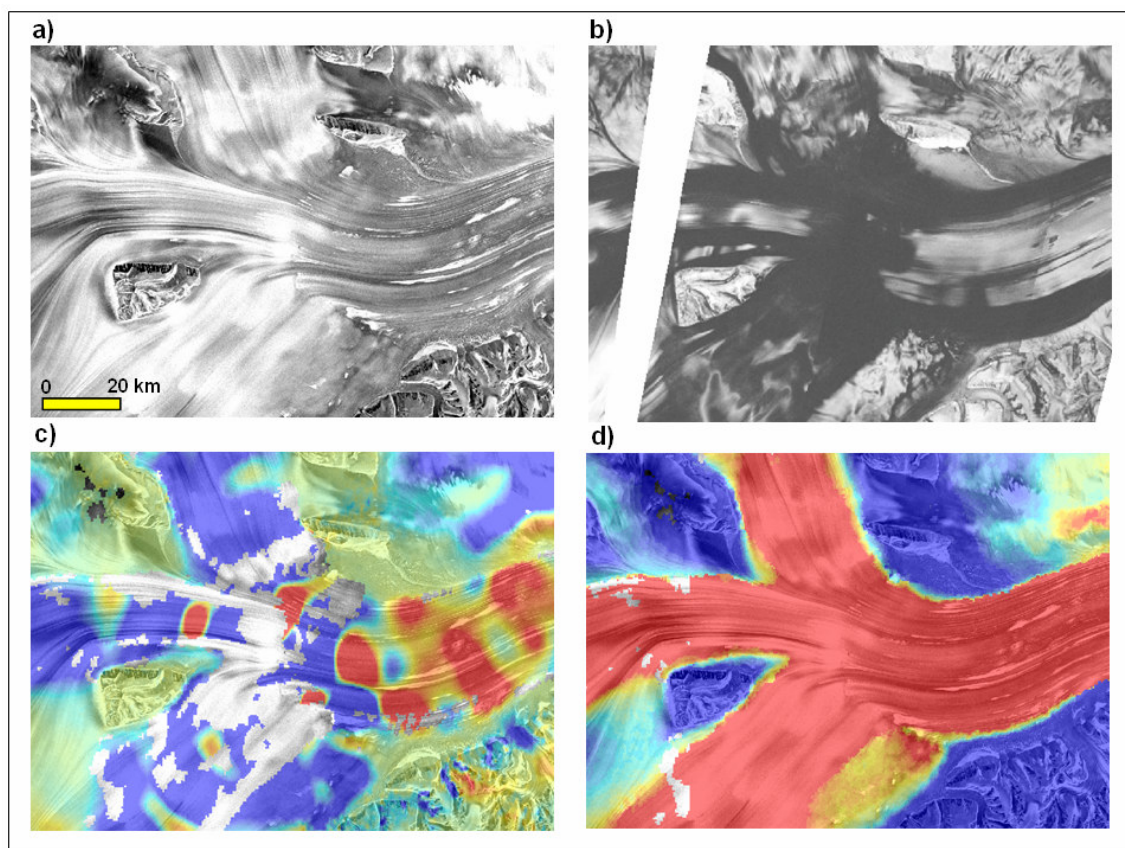Figure 4.8 The SAR image (a), coherence image (b), vertical velocity (c), and surface velocity map (d) of the western tributary glaciers of Amery Ice Shelf. The red colors represent high velocity areas and blue colors represent low velocity areas for velocity maps (c) and (d).
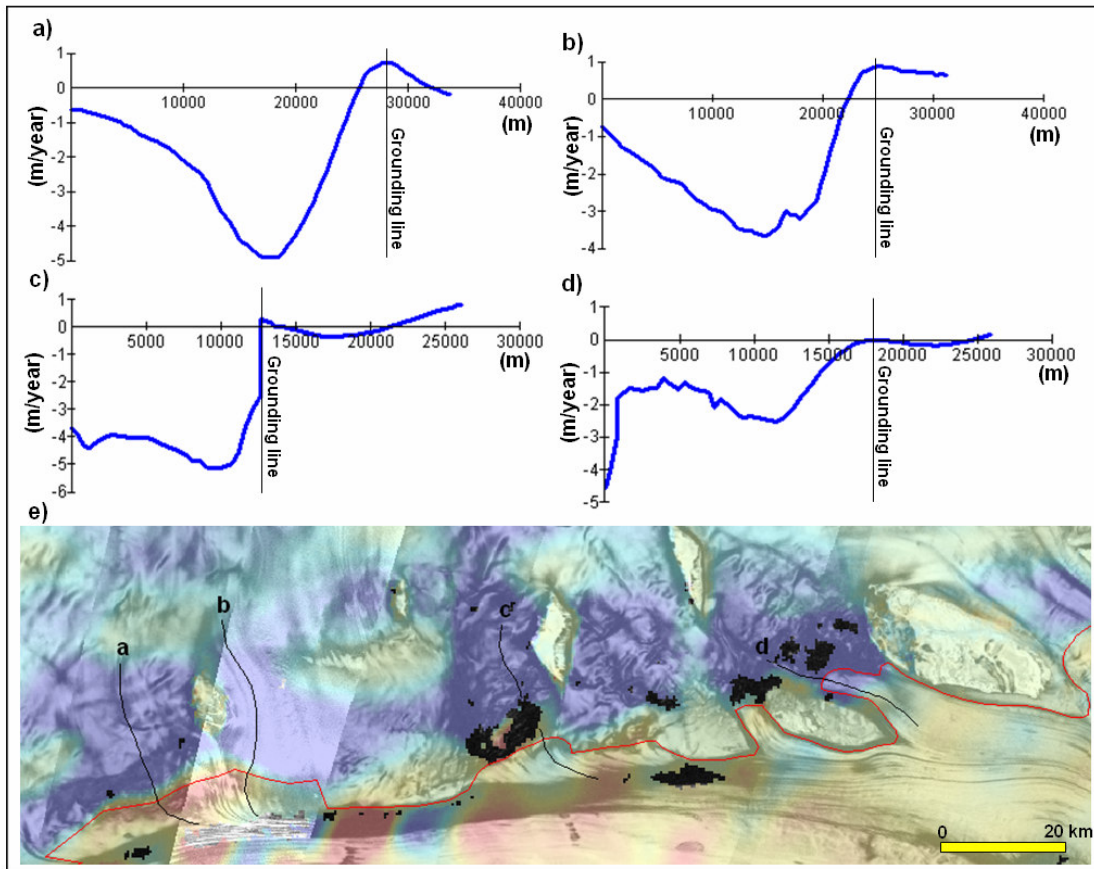
Figure 4.9 Vertical velocity profile of western tributary glaciers (a, b, c, d) and grounding line overlaid with vertical velocity field and coherence image (e).

### 4.3.3. Charybdis Glacier area

Five glacier streams including Nemesis, Charybdis, and Scylla Glacier flow into Amery Ice Shelf through the conduit between Jetty Peninsula and Single Island (Figure 4.10 a and d). Nemesis Glacier has a maximum surface velocity of 145 m/year in the high slope area. Charybdis Glacier and Scylla Glacier are the glaciers contributing the most ice mass in the area, and their surface velocity reaches a maximum of 198 m/year (Charydbis) and 158 m/year (Scylla) (Figure 4.10 d). The surface velocity increases in

the confluence area and reaches a maximum of 352 m/year where the confluence stream merges with the main stream of Amery Ice Shelf. Coherence image show complicated pattern of ice flow margins and grounding line position (Figure 4.10 b).

The vertical velocity component provides supplementary evidence in the grounding line position where the coherence image shows complications (Figure 4.10 c). This study determined the grounding line position based on overlapping areas of low coherence and positive vertical velocity component gradients.



Figure 4.10 The SAR image (a), coherence image (b), vertical velocity (c), and surface velocity map (d) of the Charybdis Glacier area. Red colors represent high velocity areas and blue colors represent low velocity areas for velocity maps (c) and (d).

Six flow lines are placed for each of the glacier flows to obtain vertical velocity profiles (Figure 4.11). As Figure 4.11 shows, the grounding line from this study matches with the low coherence and positive gradients of the vertical velocity component.
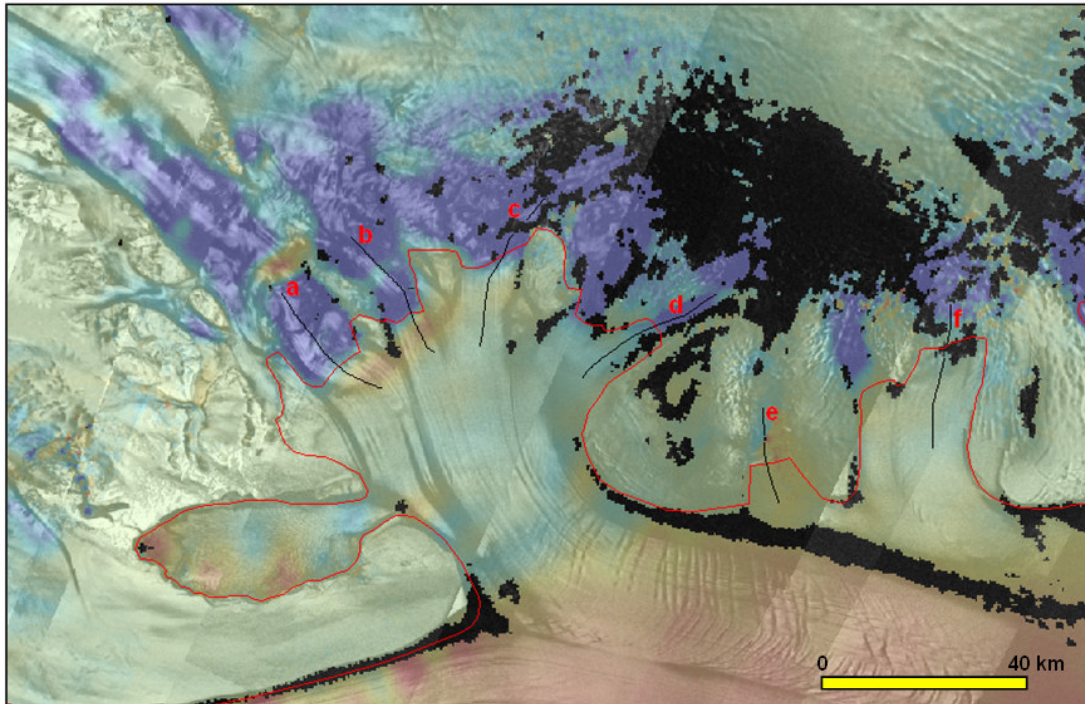


Figure 4.11 Flow lines from Nemesis, Charybdis, Scylla, and other tributary glaciers located on the western part of Amery Ice Shelf. The background image is the vertical velocity component field overlaid on the coherence image. The red line indicates the grounding line from this study.

Nemesis Glacier records a maximum vertical velocity of 0.8 m/year near grounding line and the minimum of -4.5 m/year at the high downward slope area (Figure 4.12 a). Charybdis Glacier shows two positive slopes in the vertical velocity profile

(Figure 4.12 b). However, the maximum vertical velocity of 0.7 m/year matches with the low coherence boundary. The first positive gradient is caused by a general trend of small upslope topography. Scylla Glacier does not show abrupt changes in vertical velocity (Figure 4.12 c). However, the grounding line location is drawn based on low coherence, and it matches with the highest vertical velocity along the flow line. The grounding line of tributary glaciers "d" and "e" in Figure 4.12 are not coincide between the vertical velocity and coherence image. Based on the vertical velocity gradient, the location of the grounding line for ice stream "d" should be placed further downstream since the abrupt vertical velocity change is detected at the downstream than this study identified based on low coherence boundary (Figure 4.12). Stream "e" shows a large increase in vertical velocity, but the grounding line is not placed at that point. The big jump is caused by fail in phase unwrapping and the inconsistent velocity data between the neighboring orbits; in this case the jump area is the orbit boundary. Therefore, it is more sound to determine the grounding line based on the coherence and velocity profiles within the same orbit which have the same processing parameters. Stream "f" shows similar patterns with Scylla Glacier (Figure 4.12 f).
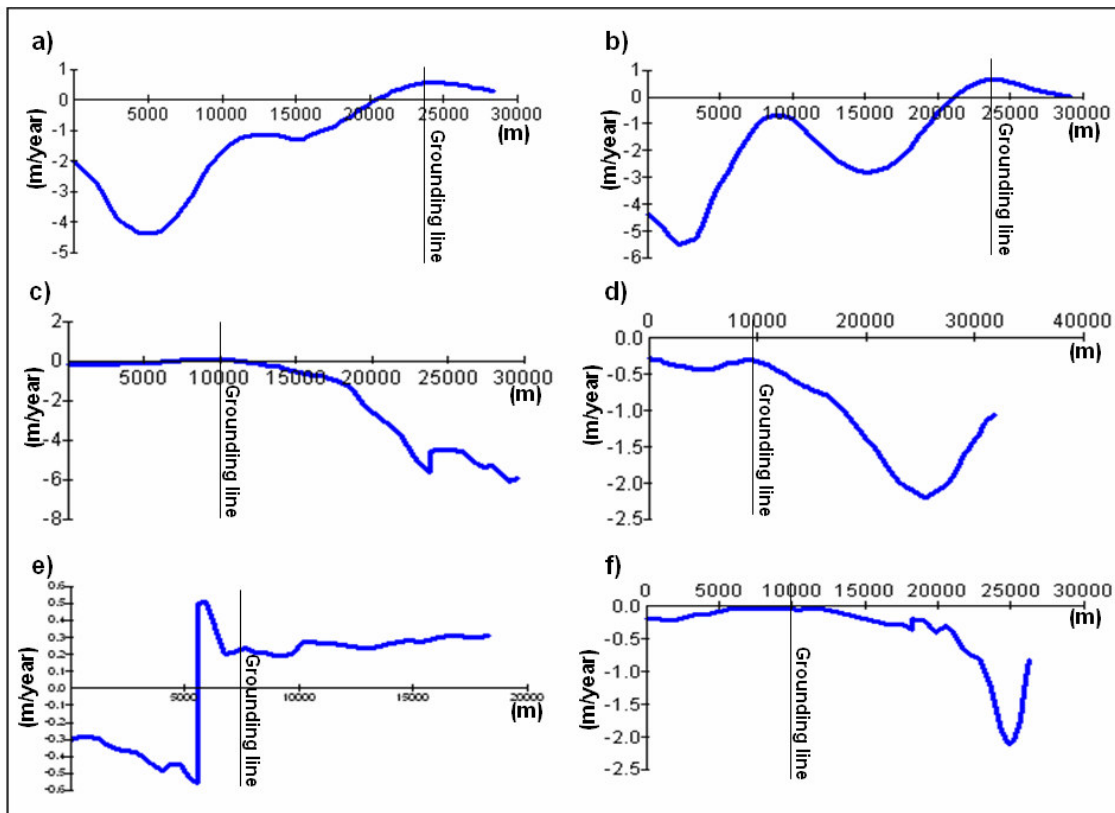
Figure 4.12 Surface velocity profile of Nemesis (a), Charybdis (b), Scylla (c), and other tributary glaciers (d, e, f) located on the western part of Amery Ice Shelf.

### 4.3.4. Tributary glaciers on east part of Amery Ice Shelf

Three main ice streams and three supplementary ice streams discharge from the east side of Amery Ice Shelf in the segment between Clemence Massif and Foster Ntk (Figure 4.13 a and d). The maximum velocity of three main ice streams ranges from 235 m/year (stream "a" in Figure 4.13) to 607 m/year (stream "d" in Figure 4.13), and velocity decreases as they merge into the main ice stream of Amery Ice Shelf (Figure 4.13 d). The supplementary ice stream have velocity ranges from 78 m/year (stream "c" ) to 119 m/year (stream "f") (Figure 4.13 d).
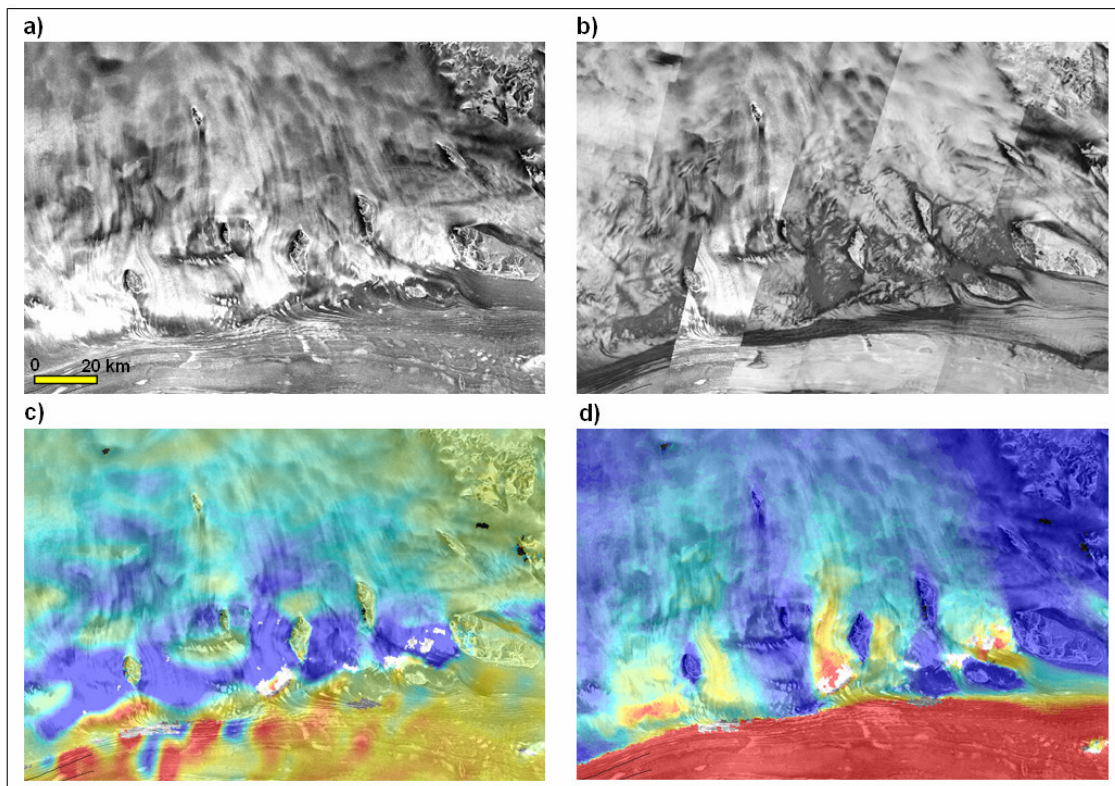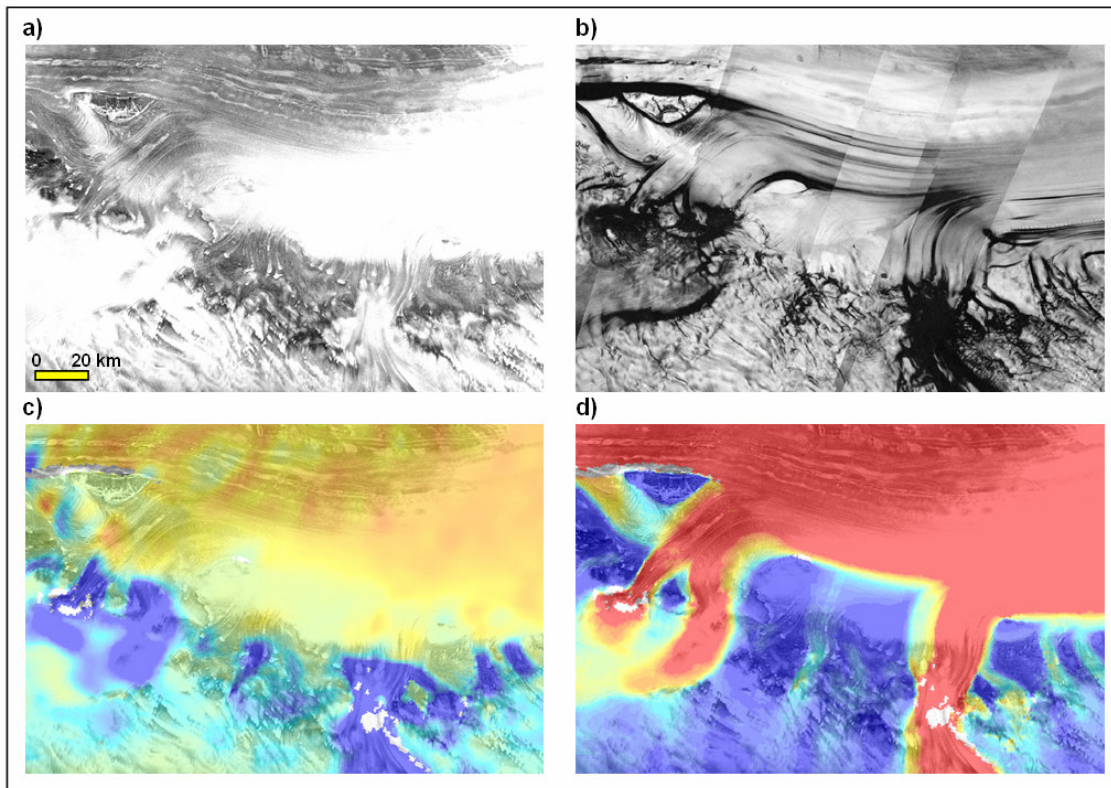
Figure 4.13 The SAR image (a), coherence image (b), vertical velocity (c), and surface velocity map (d) of the eastern tributary glacier of Amery Ice Shelf. Red colors represent high velocity areas and blue colors represent low velocity areas for velocity maps (c) and (d).

The grounding line position matches with the low coherence areas and stream channel boundaries (Figure 4.14 a). However, the vertical velocity component indicates different grounding line location different from low coherence areas (Figure 4.14 b and Figure 4.15).
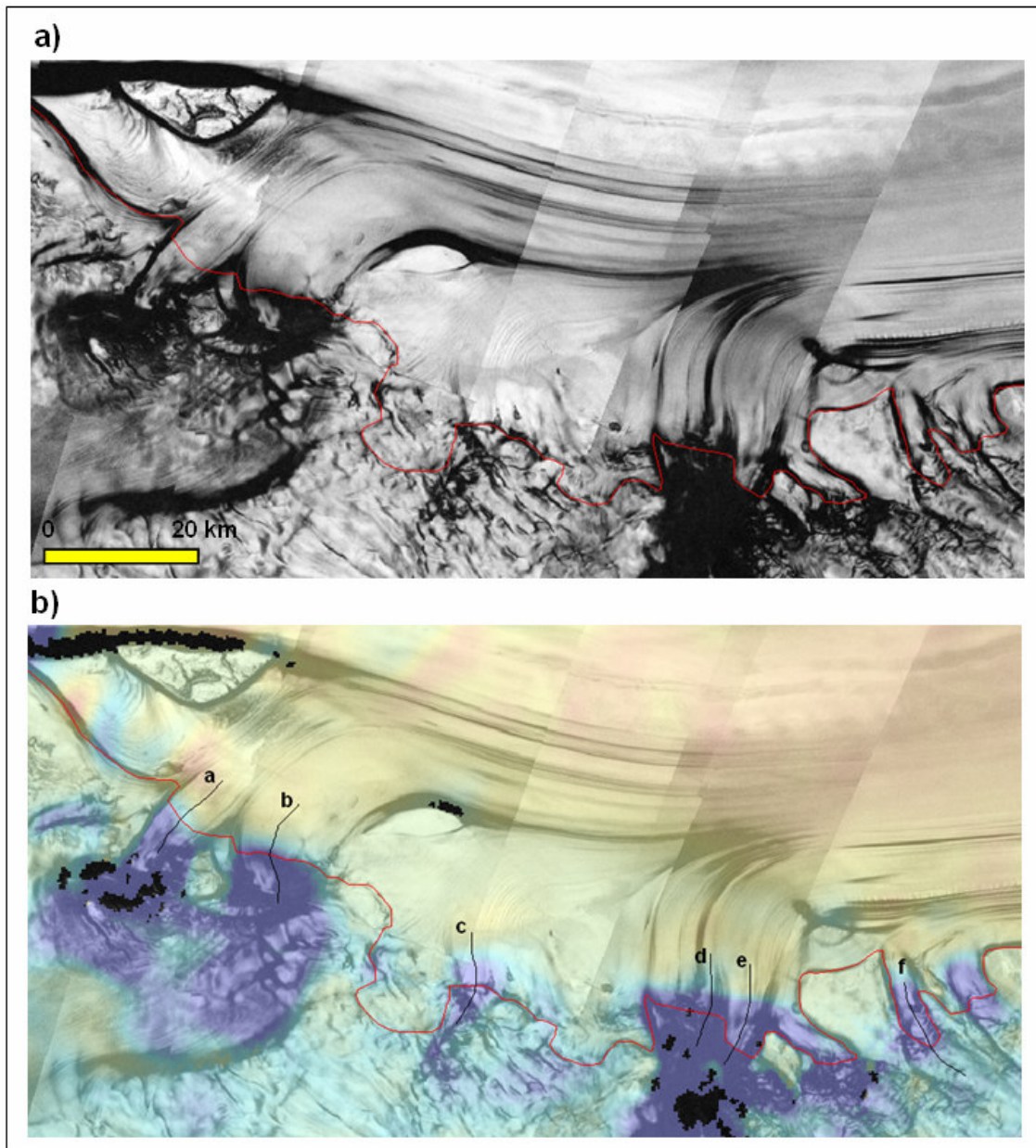
Figure 4.14 The grounding line of the eastern tributary glaciers of Amery Ice Shelf overlaid on a coherence image (a) and vertical velocity component (b).

The vertical velocity profile for the ice flow of the five main streams does not match with the coherence image in grounding line positions, which are placed in a

negative vertical velocity (Figure 4.15). This indicates that the grounding line is in transition which shows a wide range of grounding zone distributions.
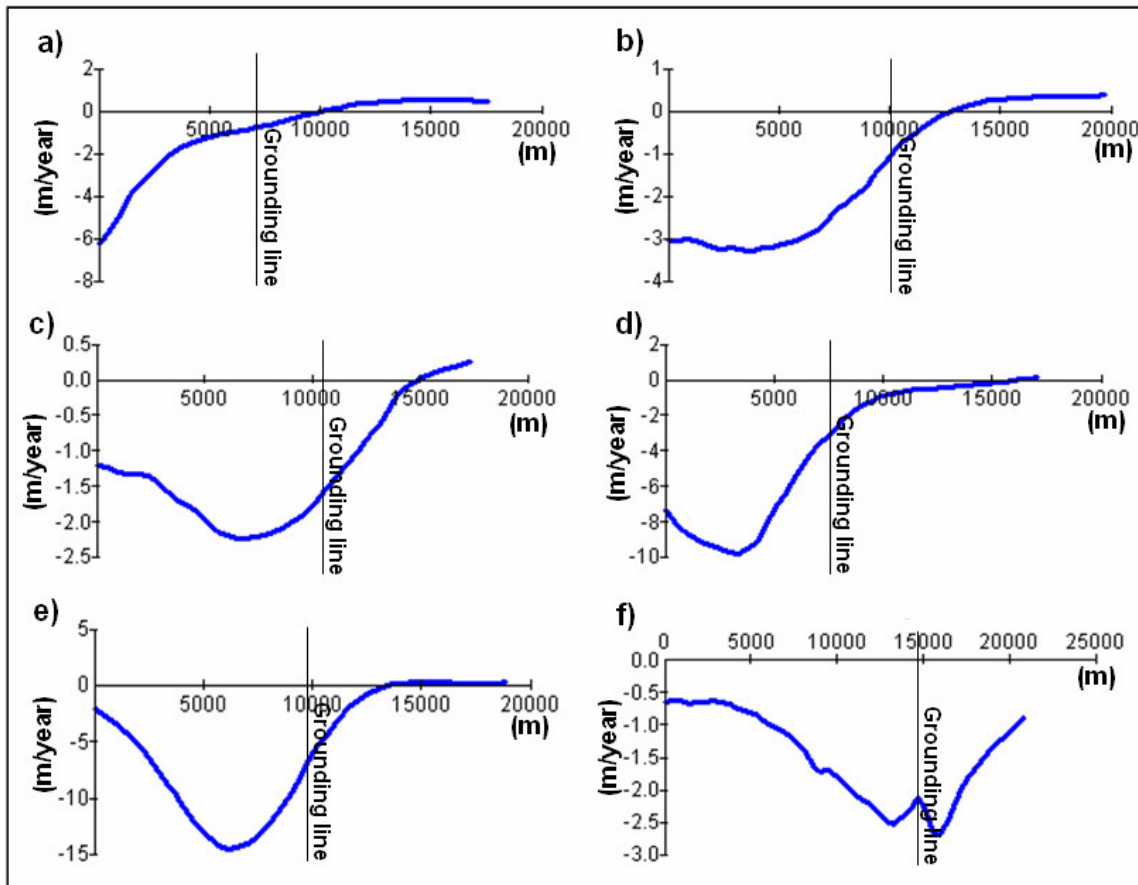


Figure 4.15 Vertical velocity profiles of eastern tributary glaciers of Amery Ice Shelf.

**4.3.5. Tributary glaciers on the east side of Amery Ice Shelf near Reinbolt Hills**

Tributary glaciers on the east side of Amery Ice Shelf near Reinbolt Hills consist of three ice streams with a maximum velocity range of 87 m/year to 148 m/year (Figure 4.16). This region shows similar patterns in the grounding line that its position in the coherence

image does not match with the vertical velocity component (Figure 4.17 and Figure 4.18). The previously applied interpretation for the eastern tributary glaciers can be used again here. It is presumed that the grounding line placed in this study is in a changing ice stream floatation zone.
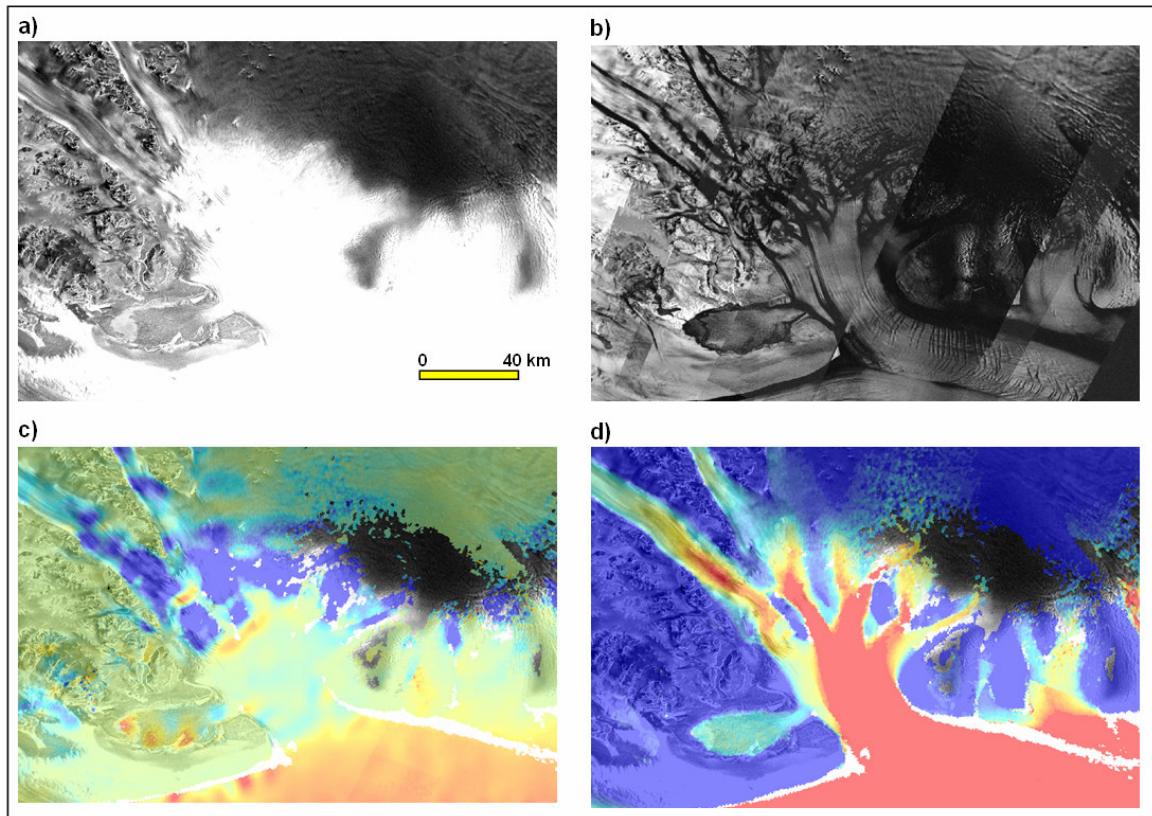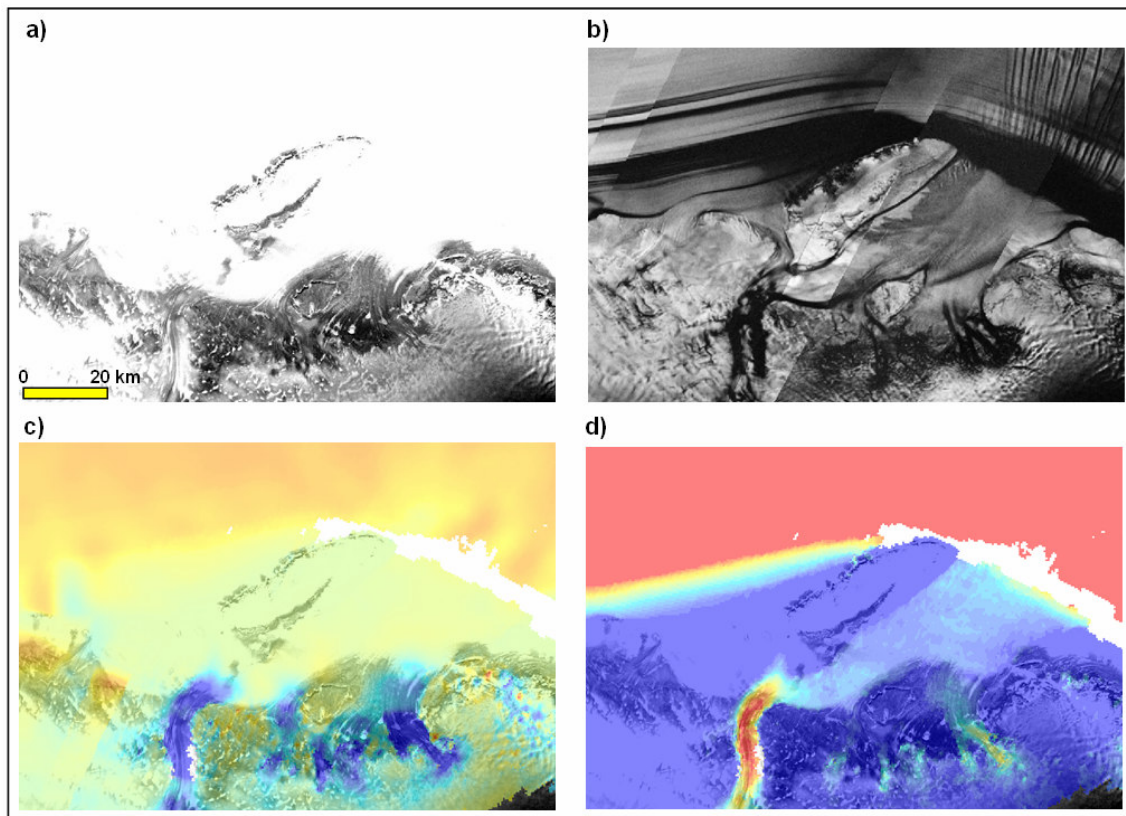


Figure 4.16 The SAR image (a), coherence image (b), vertical velocity (c), and surface velocity map (d) of tributary glaciers on the east side of Amery Ice Shelf near Reinbolt Hills. Red colors represent high velocity areas and blue colors represent low velocity areas for velocity maps (c) and (d).
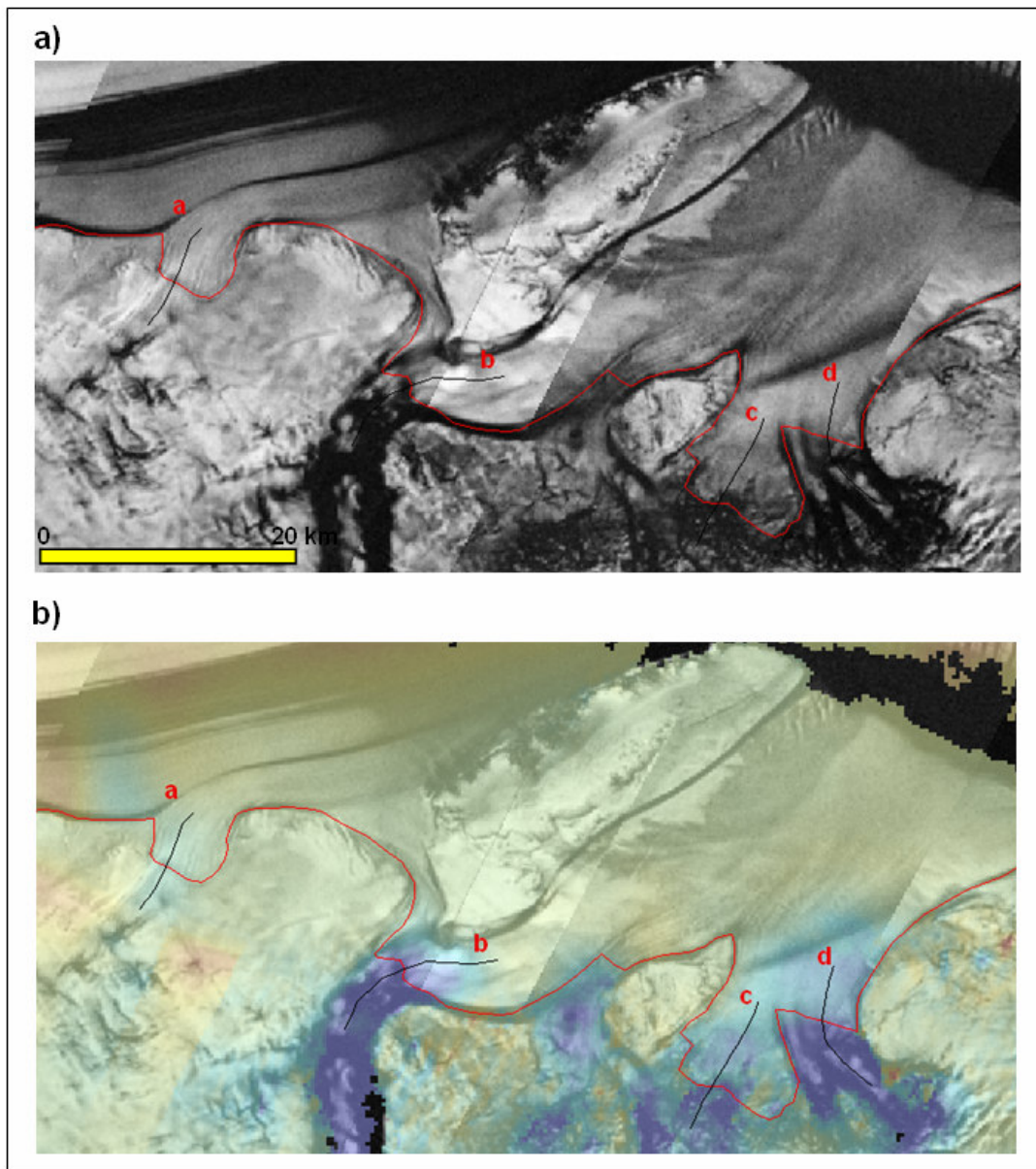
Figure 4.17 The grounding line of tributary glaciers on the east side of Amery Ice Shelf near Reinbolt Hills overlaid on a coherence image (a) and vertical velocity component (b).
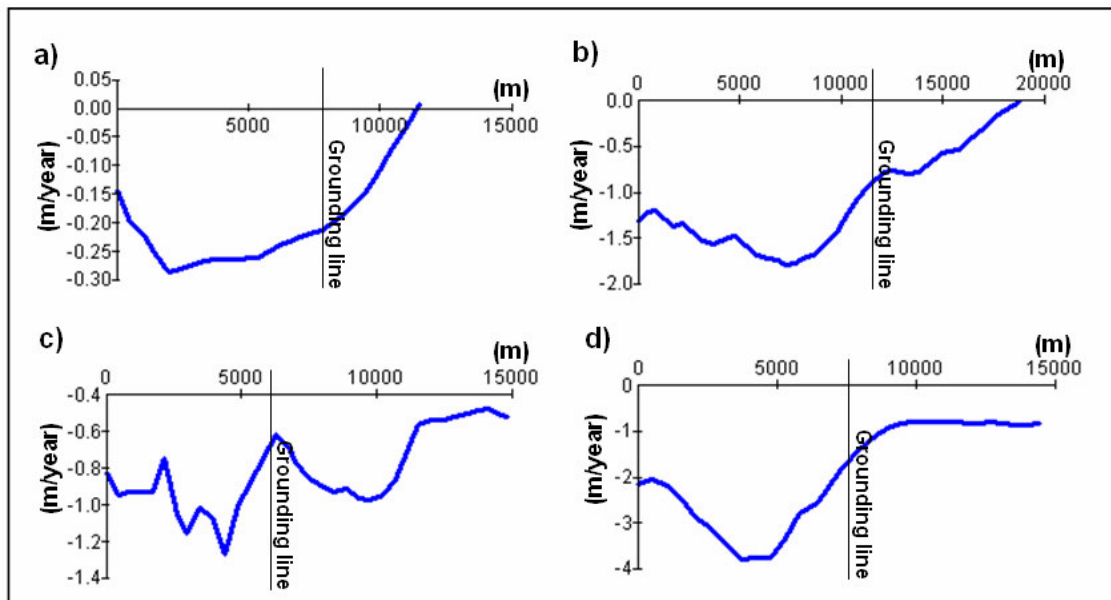
Figure 4.18 Vertical velocity profiles of tributary glaciers on the east side of Amery Ice Shelf near Reinbolt Hills.

## 4.4. Grounding line validation

As mentioned in the methodology, surface elevation combined with ice densities is useful for identifying floating ice. This study utilizes ICESat laser altimetry data as the major source of surface elevation (Zwally *et al.*2002). If the ice is floating, the height anomaly between the height from laser altimetry and height from the hydrostatic calculation of the ice thickness data should be zero. Based on the standard statistical theory of error propagation (Taylor 1997), 50 m of ice thickness, 1.5 m of height error and 10 kg/m$^3$ of density error produce a 30 to 32 m of error range on floating ice identification. This study uses 30 m as a threshold to identify floating ice. In other words, the hydrostatic anomalies within 30 m are considered as floating ice.

A total of 36,832 surface elevation points are calculated from ICESat laser altimetry (Figure 4.19). Of these, 26,130 points are within the error range indicating floating ice.

The observed general floating ice distribution matches the grounding line delineated from this study. As Figure 4.19 illustrates, some portions on the ice shelf are identified as grounded ice. Most of these observations are correct, detecting rock exposures on the ice stream such as Clemence Massif and Corry Rock. However, misidentified grounded ice points are mainly distributed in the ice shelf front and discharging area and are caused by irregular distributions and errors in ice thicknesses; only 126 out of 12,393 points are considered as errors in the ice shelf discharging area. The hydrostatic error range is 30.1 ~ 33.0 m for those areas which indicates those are the border the 30 m control for defining floating ice.

The elevation points near the grounding line show shifts to upstream ranges up to 9.8 km in the eastern tributary glacier, excluding the obvious error in the Beaver Lake area. The Beaver Lake area shows floating ice points on a rock exposure area which again is mainly caused by ice thickness errors. The main Lambert Glacier system grounding line positioned from this study is identified as grounded ice from the hydrostatic calculation and the difference between the grounding lines from the two methods ranges up to 24 km. This is expected since this method detects floating ice. If the glacier system is in transition at the grounding zone; a high down-slope angle with high surface velocity and large ice mass might induce a larger area of transition zones

between floating and grounded ice which the hydrostatic method has difficulty in quantifying (Fricker *et al.* 2002).
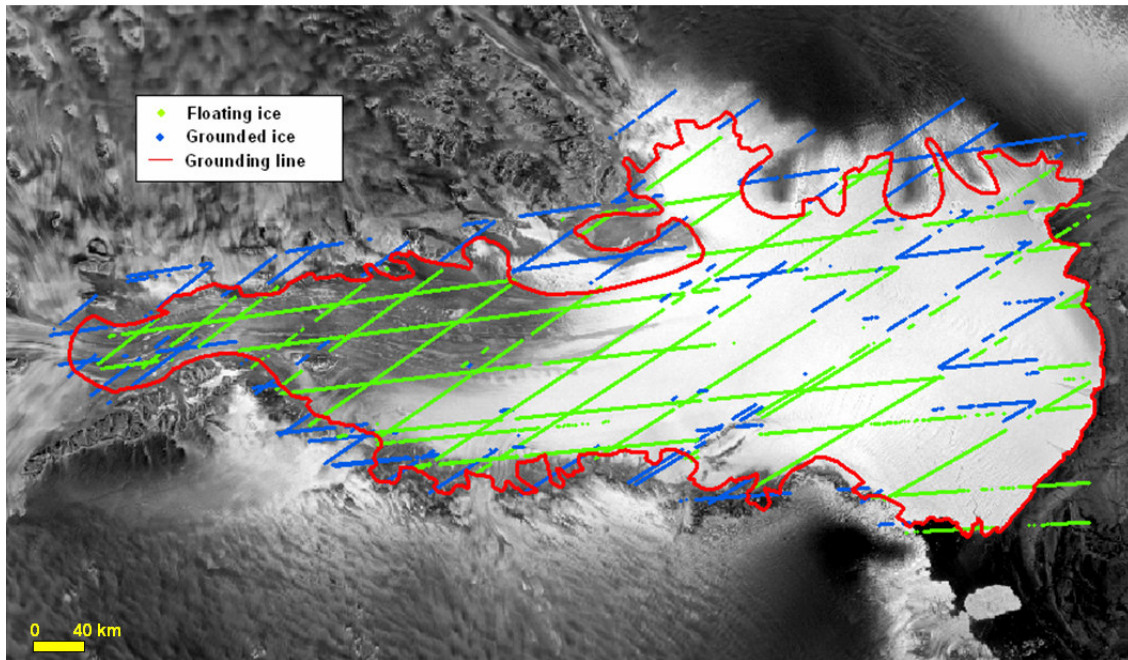


Figure 4.19 Floating ice points from the hydrostatic anomaly calculation with the grounding line from this study.

## 4.5. Comparisons with previous studies

A grounding line delineated by SAR interferometry is provided from this study. The most of the grounding line position has placed in high accuracy less than 2 km around the Amery Ice Shelf except the grounding line position of three main ice streams. The grounding line position of the three main ice stream is place within a range of 20 km low coherence zone which cause by the failure in phase unwrapping from the abrupt velocity increase. It might also indicate that the main ice stream grounding zone is distributed in

wide area. Most of the tributary glaciers shows good phase unwrapping result, and it enables higher accuracy in grounding line determination. With a vertical velocity profile and hydrostatic data, the grounding line position from this study is confirmed.

Comparing the results to a previous study (Figure 4.20), general positions are similar between this study and the groundling line by Fricker *et al.* (2002) from hydrostatic calculation. However, this study places the grounding line farther upstream compared to previous studies. The distance between the tow lines ranges up to 16.5 km at the main ice stream. This can be explained by the characteristics of the methodology. As Figure 4.21 shows, the grounding line from the hydrostatic calculation can only placed at the location of floating ice whereas the actual grounding line is located farther upstream. Therefore, the distance between the InSAR and hydrostatic results can be significant where the ice thickness is greater and surface velocity is faster which will result in pushing the hydrostatic point (H' in Figure 4.21) farther downstream.
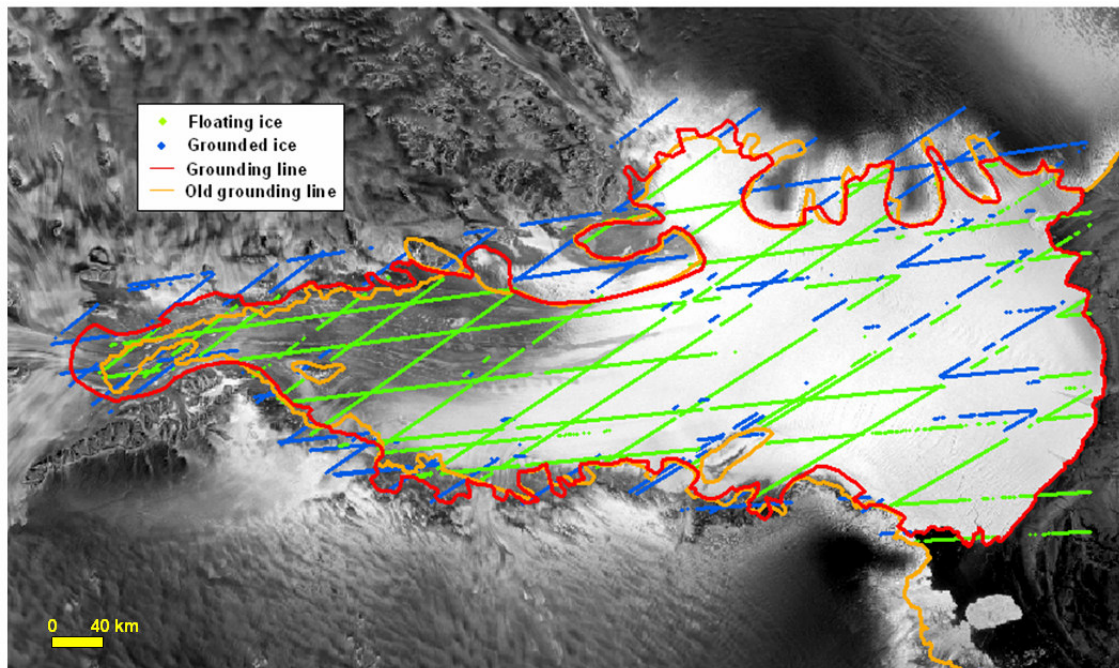
Figure 4.20 Grounding line comparison between this study and previous study.


On the other hand, there are some locations where the previous grounding line detected more upstream. But the hydrostatic calculation from this study indicates that the location is possibly wrong since it more consistently matches the grounding line from InSAR; it can be explained by accuracy in elevation data. The previous study used DEM from ERS-1 radar altimetry data in 1 km spacing (Fricker *et al.* 2000). Comparing the vertical accuracy of 1.7 m from ERS-1 and 1.5 m from ICESat data and 170 m spacing of ICESat along track spacing in addition to point level measurement, it is expected that the data from this study will provide more accurate calculation of hydrostatic anomalies.
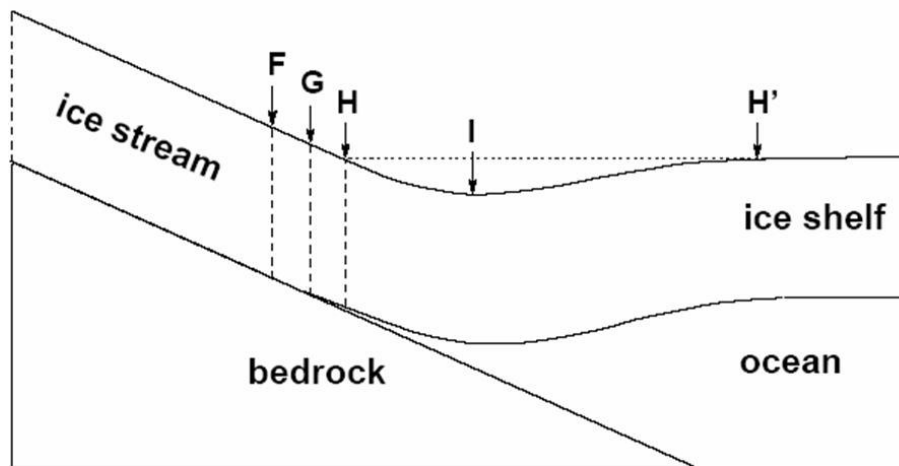
Figure 4.21 Schematic diagram of points associated with the grounding zone. F is 'limit of flexure', G is the 'grounding line', H and H' are the 'hydrostatic points' and I is the location of the change in slope. The Figure is from Fricker *et al.* (2002).

The second possible reason may be a grounding line transition. Depending on the status of ice dynamics and tidal differences, the position of the grounding line can change as was studied in the northern Greenland grounding line migration (Rignot *et al.* 2001). The data used in the InSAR process was taken in 2000 and the ICESat data in 2003 which makes 8 to 10 years difference between the data acquisition of this study and that of Fricker *et al.* (2002). In addition, this the grounding line location of this study positioned the grounding line for the main glacier further south from Fricker *et al.* (2002). This supports the grounding line extension southward suggested by Fricker *et al.* (2002). However, it is necessary to have a more thorough investigation follow up to determine the rate of grounding line migration and its impact on glacier dynamics of the area.

**CHAPTER V**

**COMPUTATION OF BALANCE VELOCITY**

**5.1. Concept of balance velocity**

Balance velocity is the depth averaged horizontal velocity required to maintain a steady state. In other words, the outward flow distribution exactly matches the net accumulation (Budd *et al.* 1971). The balance flux of a glacier system is the hypothetical distribution of mass flux in a steady state system. There are two sources of mass input, surface accumulation ($A$) and ice flux coming from higher elevations ($Q_{in}$) (Figure 5.1).
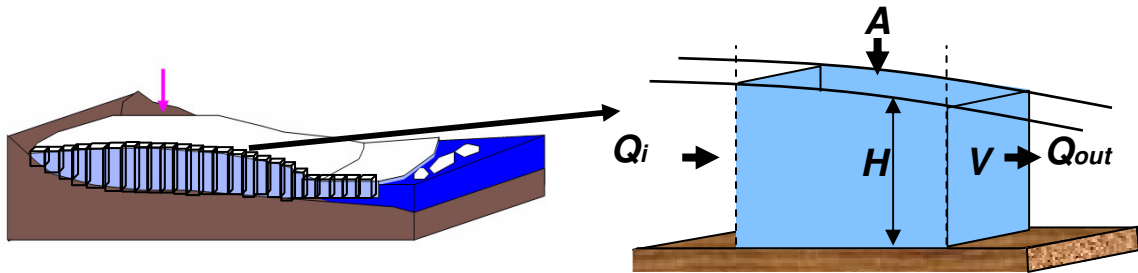


Figure 5.1 Schematic diagram showing the concept of balance velocity.

Since ice flux at any point is calculated by depth averaged velocity ($V$) multiplied by ice thickness ($H$), the combined value of ice flux from high elevation ($Q_{in}$) and accumulation at the point ($A$) should be equal to the value ($Q_{out}$) of ice thickness ($H$) times the depth averaged velocity ($V$). It can be summarized as the following equations;

$$Q = V \times H \tag{5.1}$$

$$Q_{in} + A = Q_{out} = V \times H \tag{5.2}$$

$$V = \frac{Q_{out}}{H} \tag{5.3}$$

Therefore, the balance velocity is directly calculated by the division of ice thickness if balance flux is calculated. It is necessary to know the ice flow direction and the spatial distribution of the mass accumulation rate to calculate an accurate balance flux. The balance flux distributions can provide local information on the balance state of the system using the flow velocity and ice thickness information. Balance flux calculation is carried out by two main procedures: ice flow direction calculation and ice flux distribution. Surface slopes derived from DEMs are the major sources for extracting flow direction information. However, the assumption of the ice flow direction from the DEM is valid only when the surface slope is averaged over a horizontal scale of between 10 and 20 ice thickness (Budd 1968). Because of 2,000 m average ice thickness, the highest spatial resolution of DEM for the Lambert Glacier system is limited to 20 km. As Figure 5.2 shows, the course spatial resolution is disadvantageous in detecting small ice streams. In addition, small error in flow direction and flux distribution can make huge difference in the final output.

This chapter summarizes the previous studies of balance flux calculations, suggests a new method for calculating ice flow direction and flux distribution, and compares the results on the Lambert Glacier system between previous methods and the method used in this study.
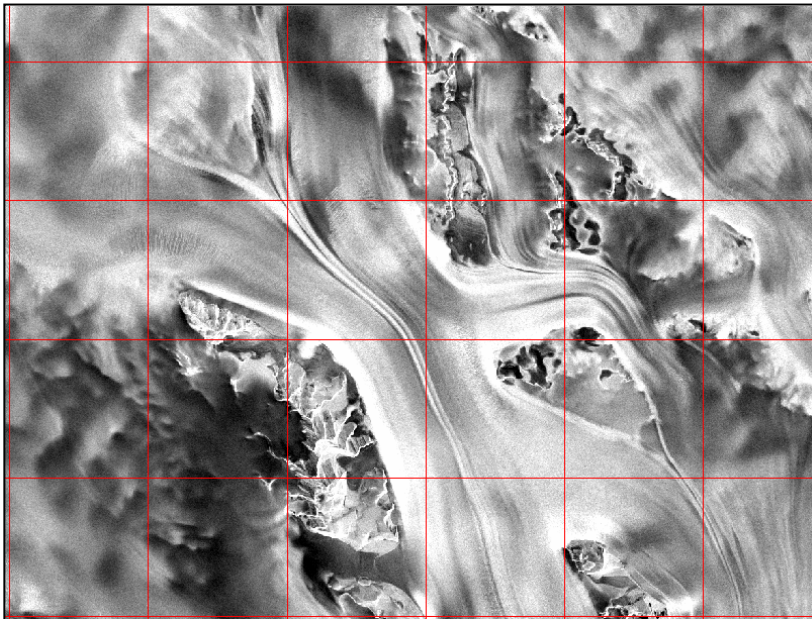
Figure 5.2 SAR image of portion of ice streams in Lambert Glacier System overlaid with 20 km grid.

A flowline-type technique was first introduced by Budd *et al.* (1971). They examined a block of ice bounded by digitized flow lines, and the net surface accumulation was calculated. This techniques was adapted by later used by other researchers (Budd and Carter 1971, Budd and Allison 1975, Smith and Budd 1981, Budd *et al.* 1982, Radok *et al.* 1987). Although this approach represents the concept of balance velocity, it has some limitations in processing time and flow direction extraction because of manual digitizing and limited flow line features.

The mostly widely used grid based method, was introduced by Budd and Smith (1965), Budd and Warner (1996) devised a finite difference method coupling the balance flux equations with flux magnitudes of neighboring cells, and this method was

later updated by Fricker *et al.* (2000). They calculated ice flow direction based on the direction of the steepest slope using a digital elevation model by comparing elevations in four cardinal pixels to the center pixel (Figure 5.3).
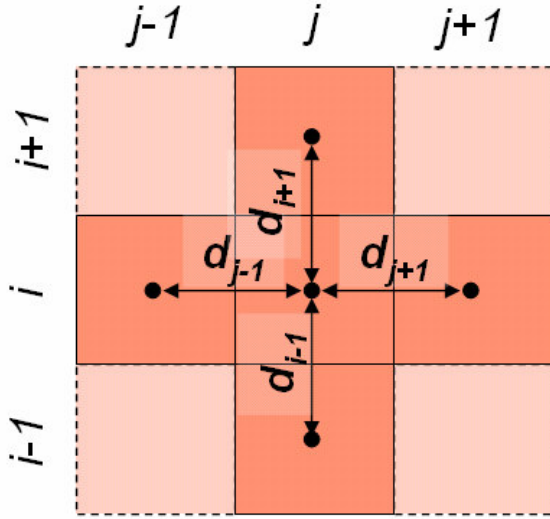


Figure 5.3 Grid cell and its neighboring pixels in flow direction calculation.

If the surface elevation of pixel (i, j) is denoted as $E_{i,j}$, the elevation difference with neighboring pixels is

$$d_{j+1} = E_{(i,j)} - E_{(i,j+1)} \tag{5.4}$$

$$d_{i+1} = E_{(i,j)} - E_{(i+1,j)} \tag{5.5}$$

Once the slope components of x (dx) and y (dy) are derived, the flow direction ( ) is

$$\cos\theta = d_x / \sqrt{d_x^2 + d_y^2} \tag{5.6}$$

$$\sin\theta = d_y / \sqrt{d_x^2 + d_y^2} \tag{5.7}$$

since the rate of ice flow through a cell with side length $l$ is related to both the flux magnitude and the direction of flow through the cell, the balance flux can be calculated as

$$\Phi_B = \frac{\psi_{i,j}^{out}}{l(|\cos\theta| + |\sin\theta|)} \tag{5.8}$$

where out flux of cell (i, j) is

$$\psi_{i,j}^{out} = a_{i,j}l^2 + \psi_{i,j}^{in} \tag{5.9}$$

where $a_{i,j}$ is surface accumulation of cell (i, j) and $l$ is cell size.

However, this method has limitations in detecting slope and flux distribution in diagonal pixels, since the process is based on cardinal pixels.


## 5.2. Flow direction calculation

The main concept of balance velocity has a lot in common with hydrological modeling, where there have been many studies approaches for calculating flow direction and flow accumulation from DEM (O'Callagham and Mark 1984, Quinn *et al.* 1991, Freeman 1991, Costa-Cabral and Burges 1994, Lea 1992, Tarboton, 1997). Therefore, hydrological modeling can provide useful options for flow direction calculation. This study uses Tarboton (1997)'s fitting plane algorithm (D $\infty$ ) to calculate flow direction from a DEM.
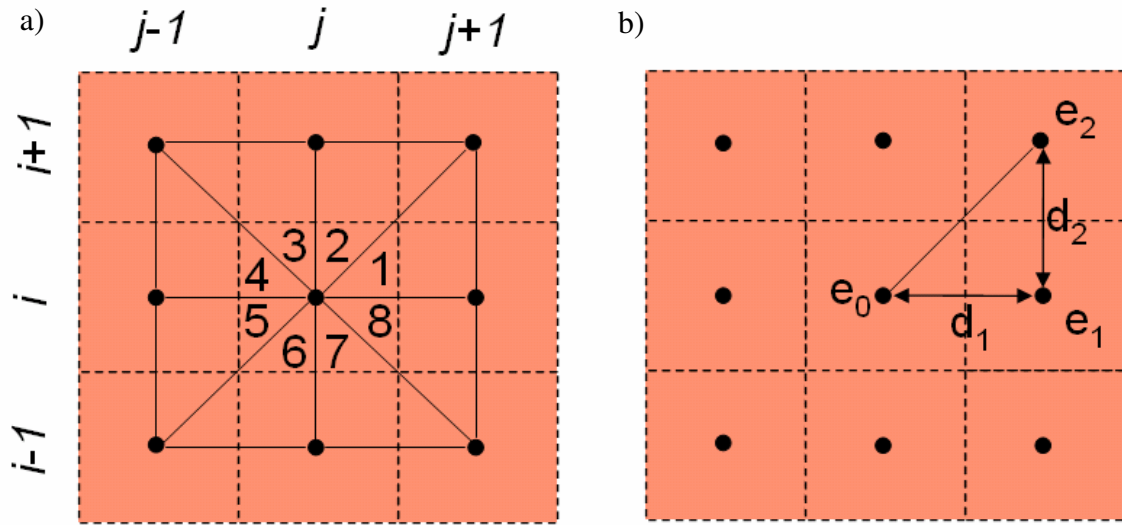
Figure 5.4 Plane triangular facets on a block-centered grid (a) and definition of variables (b) for the calculation of slope.

Tarboton (1997) calculated the slope magnitude and slope direction for each facet created on planar triangular facets on a block-centered grid (Figure 5.4) with the following;

$$r = \tan^{-1}(s_2 / s_1) \tag{5.10}$$

$$s = (s_1^2 + s_2^2)^{1/2} \tag{5.11}$$

where $r$ is the steepest slope direction, $s$ is the slope magnitude. And the slope vector of each component can be calculated as (Figure 5.4);

$$s_1 = (e_0 - e_1)/d_1 \tag{5.12}$$

$$s_2 = (e_1 - e_2)/d_2 \tag{5.13}$$

where $e$ is the elevation and $d$ is the pixel size.

Once all the components for each facet have been calculated, the flow direction of the center pixel can be extracted with,

$$r_g = a_f r' + a_c \pi / 2 \qquad\qquad (5.14)$$

where r' is the slope direction from the facet with the maximum slope magnitude. And the multiplier $a_f$ and the constant $a_c$ depend on the facet selected.

## 5.3. Flux distribution

Previous studies have had problems in assigning the flux to diagonal pixels. If the cardinal pixel is flowing away from the diagonal pixel, the flux can never be assigned to the diagonal pixel (Figure 5.5). However, it could be contrary to physical law to assign the flux directly to the diagonal pixel because there is no face contacting the diagonal pixel to assign the flux.
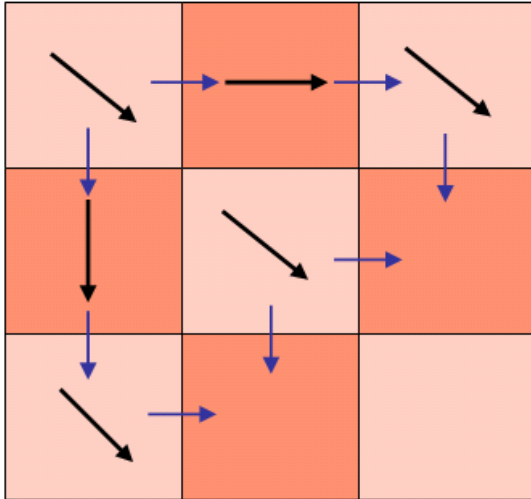


Figure 5.5 Schematic diagram showing cardinal flux distribution.

To solve this problem, this study created new algorithms to deal with two different types of flux; passing through flux and redistributing flux. Ice flux in one pixel calculated from equation 5.7 is subdivided into passing-through flux and redistributing flux based on the ice flow direction following;

$$\psi_{P(i,j)} = (\psi_{in(i,j)} + A_{(i,j)}) \times \tan\theta \qquad (5.15)$$

where $\psi_{P(i,j)}$ is the passing through flux distributed from cell (i, j), $\psi_{in(i,j)}$ is the total influx to cell (i, j), $A_{(i,j)}$ is the surface mass accumulation for cell (i, j), and $\theta$ is the flow direction (Figure 5.6). Since the total out flux from the cell should be equal to the total input to the cell, the redistributing flux ($\psi_{R(i,j)}$) of cell (i, j) is;

$$\psi_{R(i,j)} = (\psi_{in(i,j)} + A_{(i,j)}) - \psi_{P(i,j)} \qquad (5.16)$$

Once the passing-through flux and redistributing flux are calculated, the redistributing flux is assigned to neighboring cardinal pixel following the flow direction (Figure 5.5 a). The passing-through flux is divided into two identical fluxes to be assigned to two neighboring pixels in a cardinal direction following the flow direction (Figure 5.6 a). After assigning the passing-through flux to the cardinal pixels, the flux amount is considered for just the input flux to the cardinal flux but not considered for accumulated flux to be redistributed for out-flux calculation. Instead, the passing-through flux is assigned once again to the cardinal pixel that is diagonal from the origin (Figure 5.6 b). The passing-through flux reassigned to the destination pixel is saved as influx to that pixel and will be added in the out-flux calculation resulting in the same effect of flux assignment to the diagonal pixel from the origin (Figure 5.6 c). Therefore,

the whole flux in the pixel will be considered as passing-through flux and assigned to the

diagonal pixel if the flow direction is n* $n \times \dfrac{\pi}{4}$ (Figure 5.6 d). Since this algorithm

assigns the diagonal flux through cardinal pixel, it is named the Cardinal Addressing and

Redistributing Algorithm.
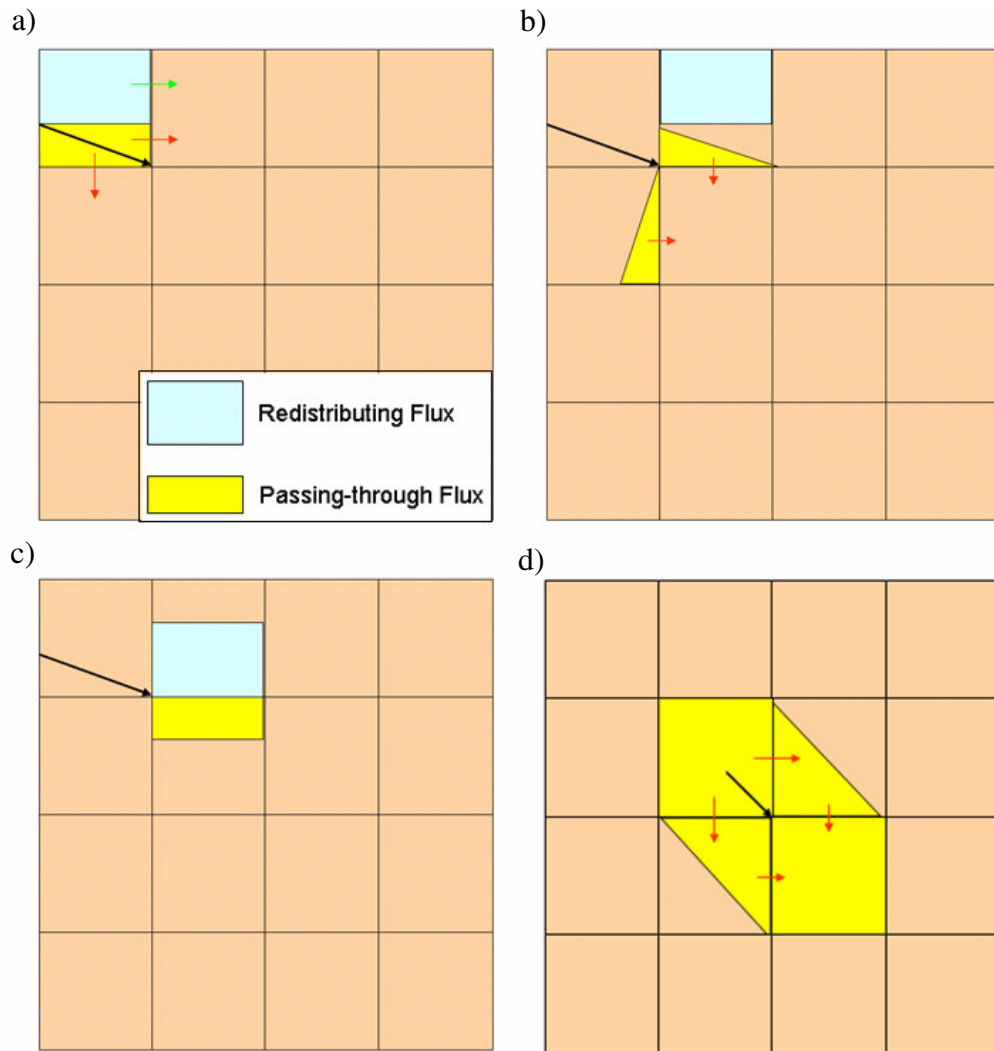


Figure 5.6 Flux distributing process of cardinal addressing and redistributing flux

algorithm from this study.

**5.4. Balance velocity of the Lambert Glacial Basin**

The OSU DEM (Liu *et al.* 1999) is used as major input of elevations for flow direction calculations. The DEM is compiled using several topographic data sets which have rather disparate sampling intervals. The interpolated product is re-sampled into 200, 400, and 1000 m post spacing. This study resampled 200 m DEM to 20 km spatial resolution to derive flow direction based on the surface elevation.

The accumulation data from Vaughan *et al*. (1999) is utilized to calculate balance flux. The surface accumulation map of Vaughan *et al*. (1999) in a 10 km resolution grid was derived from passive microwave satellite data along with 1800 in situ measurements. The 10 km cell size accumulation grid is resampled to 20 km for consistency with surface elevations. The balance flux grid is divided by ice thickness to calculate balance velocity. The BEDMAP 5 km cell size ice thickness data (Lythe *et al.* 2001) is the source of the ice thickness in the balance velocity calculation. The BEDMAP ice thickness is derived from more than 150 independents surveys, conducted by 15 nations, over the pas 50 years. Compared to other parts of Antarctica, Lambert Glacial Basin-Amery Ice Shelf system has the densest data coverage, where ground based Radar Echo Sounding and Airborne Radar Echo Sound data have 5 km to 10 km track-spacing. The accuracy of ice thickness is different in different regions. The thickness accuracy of the study area ranges 50 m at Amery Ice Shelf to 150 m at high elevation areas (Lythe *et al.* 2001).

Following the methods for ice flow calculation and ice flux distribution above, the balance flux distribution over the Lambert Glacial Basin is derived (Figure 5.7). As

Figure 5.7 shows, the balance flux provides an effective representation of the pattern of surface ice flow that would be present if the system were in balance. Streaming behavior of the flow in topographic channels is clearly distinguished in spite of limited spatial resolution. Stream boundaries and tributary channels are easily detected, and the magnitude of flux increases as the stream order increases.

To show the general pattern in detail, the balance flux grid is resampled into a 5 km cell size using bilinear interpolation, and the balance velocity is calculated at 5 km spatial resolution. As Figure 5.8 shows, the main ice streams are identified easily and it indicates that the ice flux is mainly transported by the Lambert and Mellor Glaciers. Except for abnormally high velocity on the high elevation area of the western tributary glacier, balance velocity increases downward and shows two main discharges from Amery Ice Shelf to the ocean; one from a major stream from the Lambert system, and the other from western glaciers located in the down stream area including Charybdis Glacier.
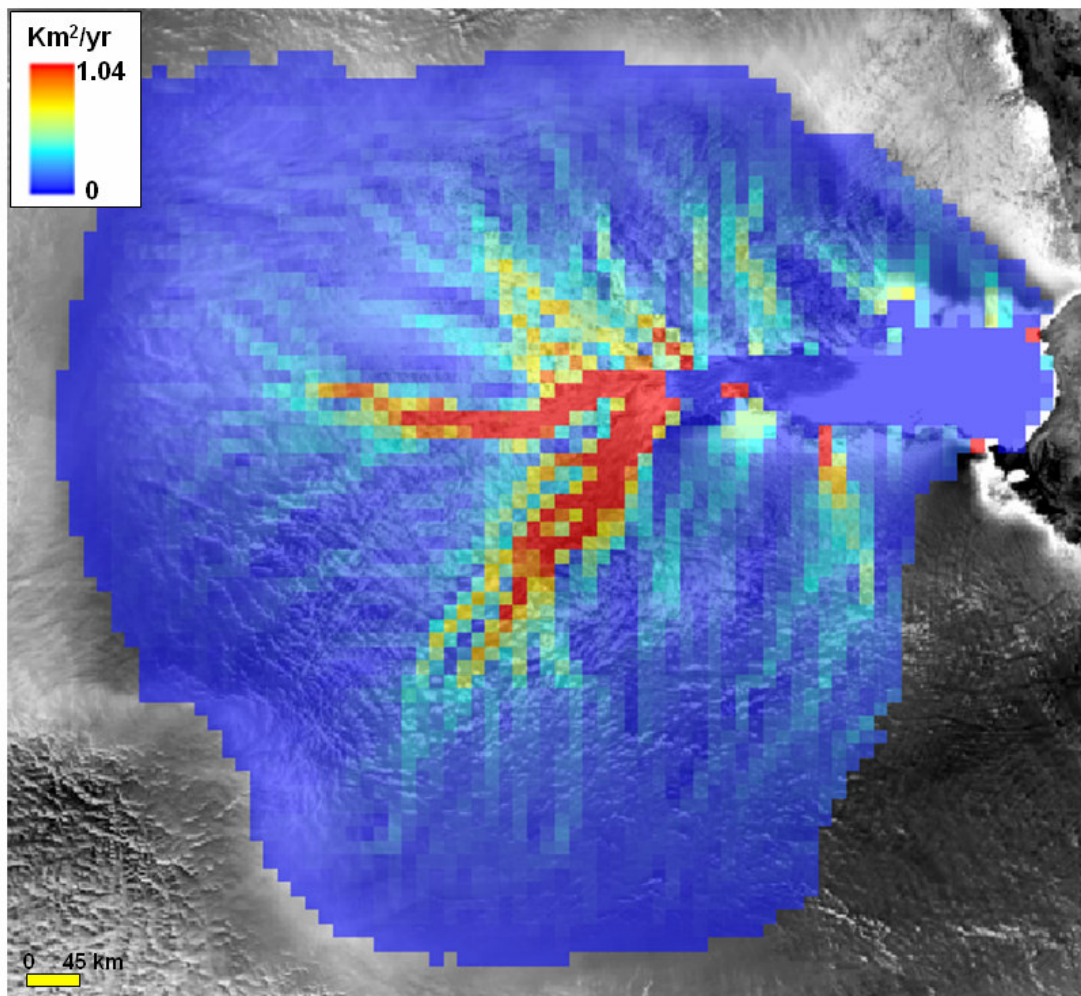
Figure 5.7 Balance flux of Lambert Glacier – Amery Ice Shelf system.
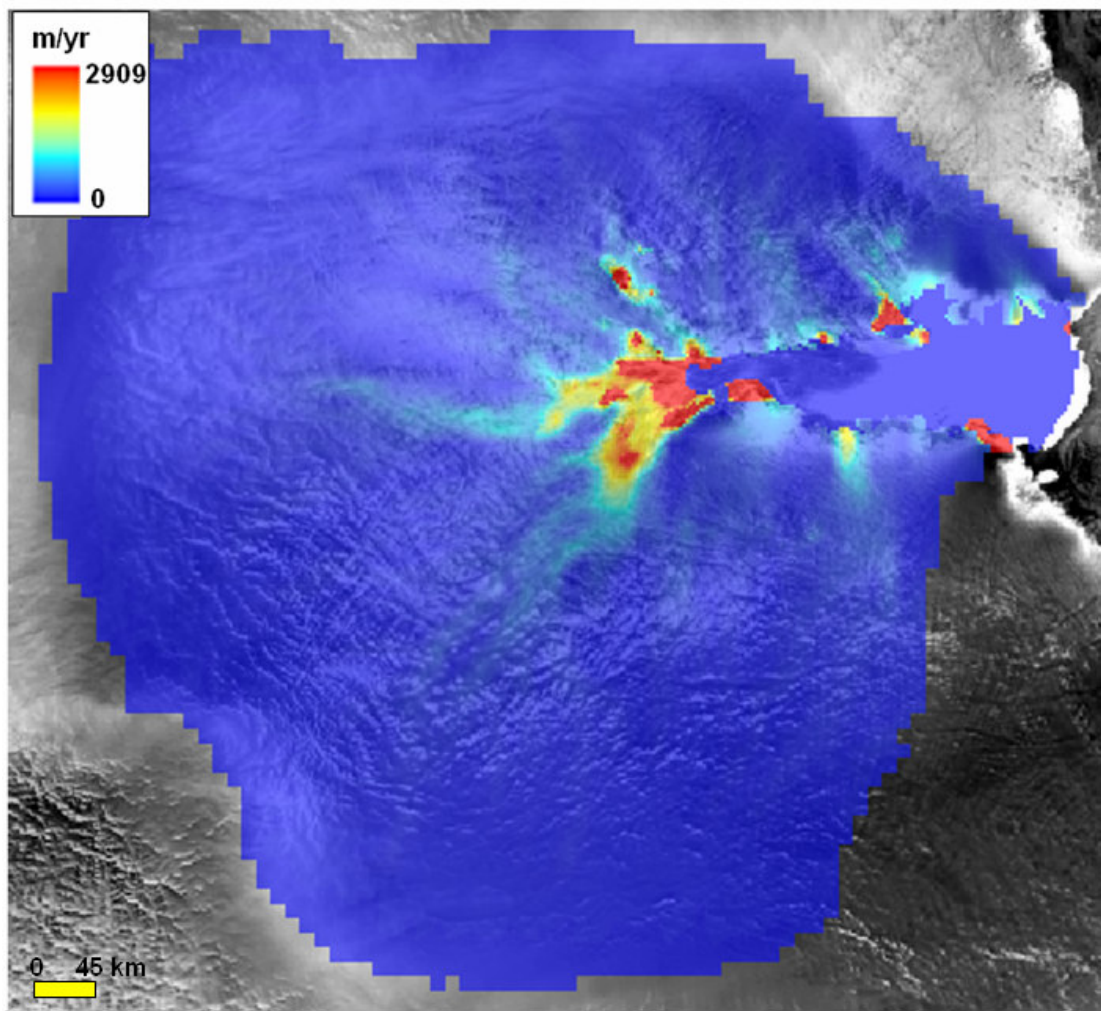
Figure 5.8 Balance velocity of Lambert Glacier – Amery Ice Shelf system.

## 5.5. Interpretation

To make comparisons and spatial distribution of balance velocity over the Lambert Glacier - Amery Ice Shelf system, the balance velocity from Budd and Warner (1996), balance velocity from this study, and the ice depth averaged velocity from SAR interferometry are utilized. Although differences exist in basic assumptions between

balance velocity and measured velocity from satellites, the general pattern of stream line topography and velocity distribution should be the same. The InSAR surface velocity is converted into the ice depth average velocity by multiplying by 0.87 (Budd and Warner, 1996) for the grounded ice area. It is assumed that ice depth average velocity is the same as the surface velocity multiplied by ice depth average velocity factor of 0.87.

As Figure 5.9 shows, the balance velocity from this study delineates the main stream and stream boundaries (b) compared to Budd and Warner's algorithm (a). General stream patterns and stream widths have more similarities with this study and InSAR velocity. However, both of the balance velocities failed in the detection of the main ice stream in Amery Ice Shelf because the flat surface elevation in the ice shelf area presents difficulties in determining the ice flow direction. In addition, the balance velocity calculation is not valid for the ice shelf region since it does not consider basal melting. Therefore, ice shelf area is excluded for the interpretation and analysis. The ice stream detection in the mountain areas is inconsistent with the InSAR velocity as the 20 km resolution of cell size has disadvantages where topographic variations result in small stream channels flowing through valleys.  It results in limitation in flow direction calculation and ice flux distribution in mountain areas.

128
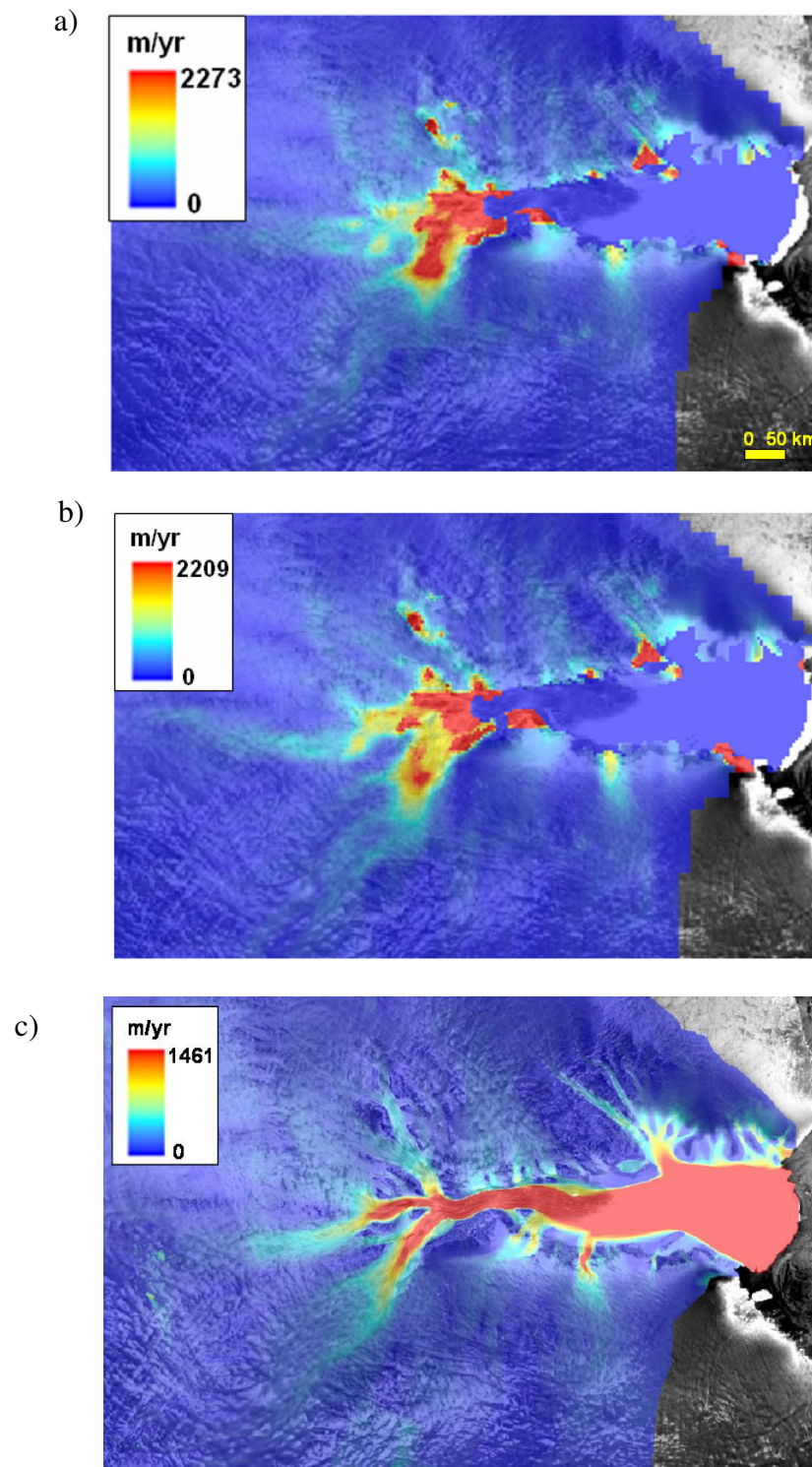


Figure 5.9 Balance velocity and ice depth averaged velocity comparison from Budd and Warner (1996) (a), this study (b), and SAR interferometry (c).

To compare the abilities of detecting stream channel in relatively gentle slope areas and mountainous areas, transverse velocity profiles were created for Lambert, Mellor, Fisher and Charybdis Glaciers (Figure 5.10 and 11). The profile line for Lambert and Mellor Glaciers represent gentle slope stream channels and the profile line for Fisher and Charybdis Glaciers represent valley stream channels.

Both the balance velocity from Budd and Warner (1996) and this study delineated the ice streams in gentle slopes (Figure 5.11 a and b). But in terms of stream location and velocity distribution, the balance velocity of this study is superior compared to that of the previous study. This study was successful in deferring the velocity range in Lambert Glacier showing 10 to 15 m/year difference from InSAR velocity (Figure 5.11 a), and also the shape of the profile is identical to the InSAR velocity, except the area where the velocity decreases abruptly because of the limitations on spatial resolution. The balance velocity from the Budd and Water (1996) generally estimated the velocity 50 ~ 60 % lower than the InSAR velocity and it often detects incorrect stream position as in the case of Mellor Glacier (Figure 5.11 b). As previously stated, the valley glaciers can not be detected effectively using balance velocity and so both of the balance velocity methods failed and showed reverse patterns of velocity distribution (Figure 5.11 c and d). However, both of the balance velocity methods detected small balance velocities as in the case of Charybdis Glacier because of the relatively wide width of the stream channel (Figure 5.11 d). The velocity distribution for the valley glacier shows huge differences in the reverse pattern (Figure 5.11 c), and even the velocity estimation is 50 to 70 % lower for relatively wide valley glaciers.
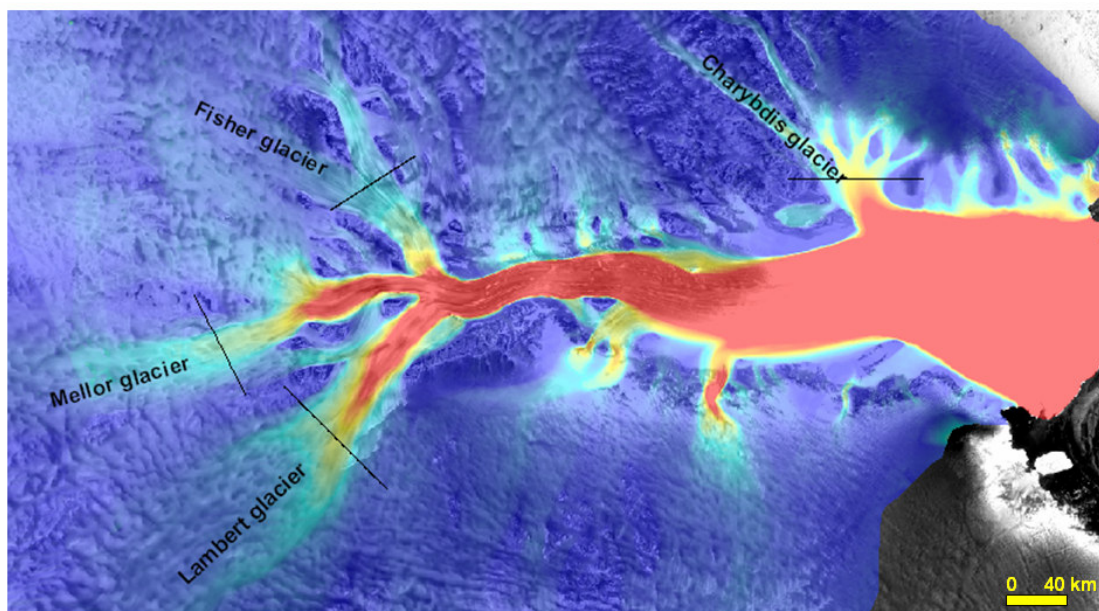
Figure 5.10 Location of velocity profile overlaid on SAR interferometry ice depth averaged velocity map.
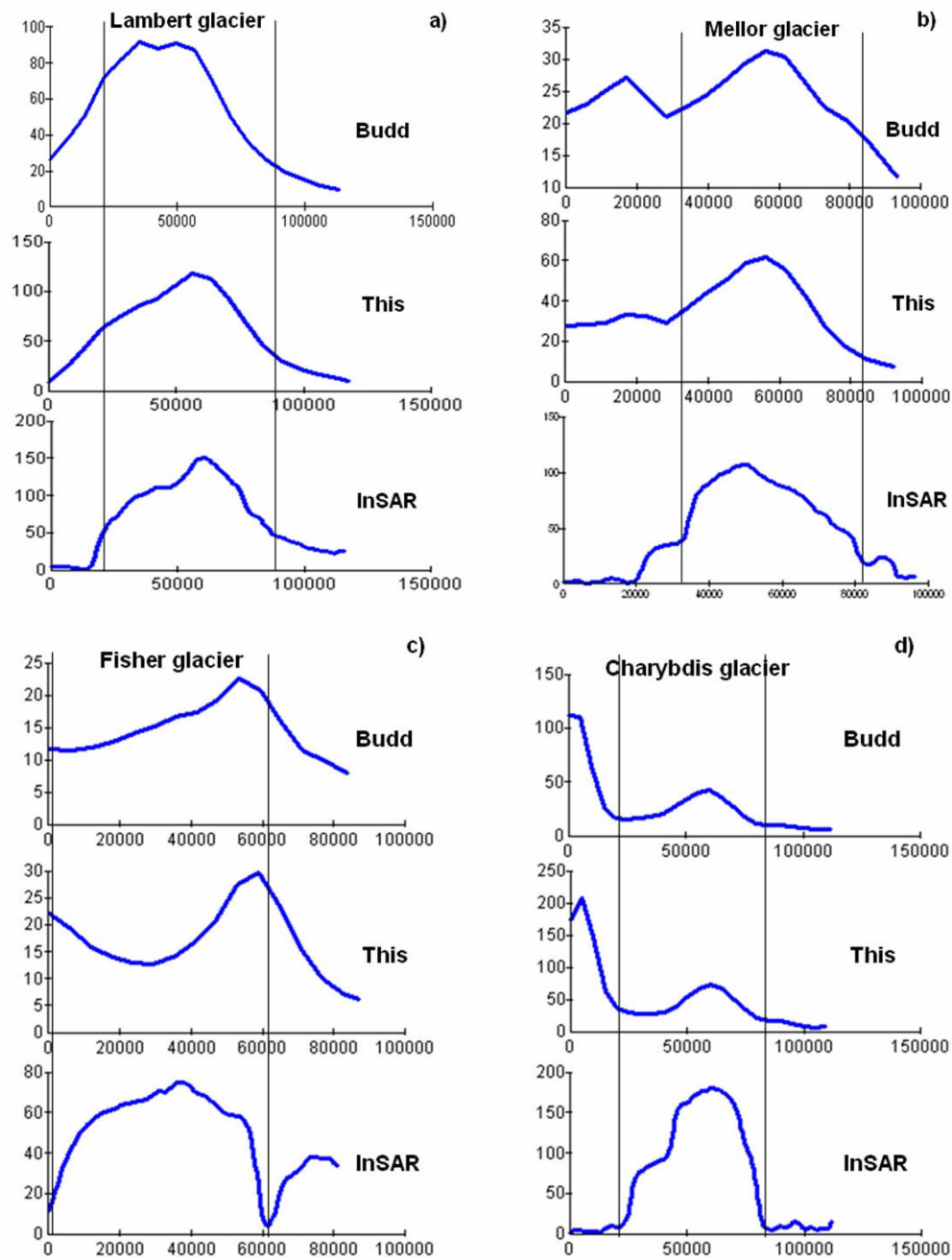
Figure 5.11 Transverse velocity profiles of Lambert (a), Mellor (b), Fisher (c), and Charybdis Glaciers (d). "Budd" indicates the balance velocity from Budd and Warner (1996), "This" indicates the balance velocity from this study, and "InSAR" indicates ice depth average velocity from SAR interferometry.

The velocity difference grids between the balance velocity and InSAR velocity were created to illustrate the balance velocity distribution errors in terms of stream line extraction to compare the result between Budd and Warner (1996) and this study. As Figure 5.12 and Table 5.1 show, minimal velocity difference pixels are more widely distributed for this study. It is especially effective for delineating the upstream area. Whereas the previous study shows larger differences in major channels of Lambert and Mellor Glaciers, this study provides a better representation of the general trends of ice streams. However, this study has disadvantages in the downstream area since it overestimates balance velocity as it discharges because of the flux distribution algorithm based on the velocity difference with InSAR velocity. In conclusion, this study is very effective in balance velocity calculation in upstream area. It makes this study a more reliable tool in balance velocity calculation since it is more useful in upstream areas.

Table 5.1 Summary of velocity difference between balance velocity from Budd and Warner (1996) and InSAR velocity, and between balance velocity from this study and InSAR velocity.

| Velocity difference (m/year) | Budd and Warner (1996) | | This study | |
|---|---|---|---|---|
| | No. of pixels | % of pixels | No. of pixels | % of pixels |
| 0~50 | 52946 | 93.4 | 53114 | 93.8 |
| 50~200 | 2148 | 3.8 | 1872 | 3.3 |
| 200~500 | 998 | 1.8 | 904 | 1.6 |
| 500~1000 | 464 | 0.8 | 310 | 0.5 |
| > 1000 | 126 | 0.2 | 433 | 0.8 |
| Total | 56682 | 100 | 56633 | 100 |
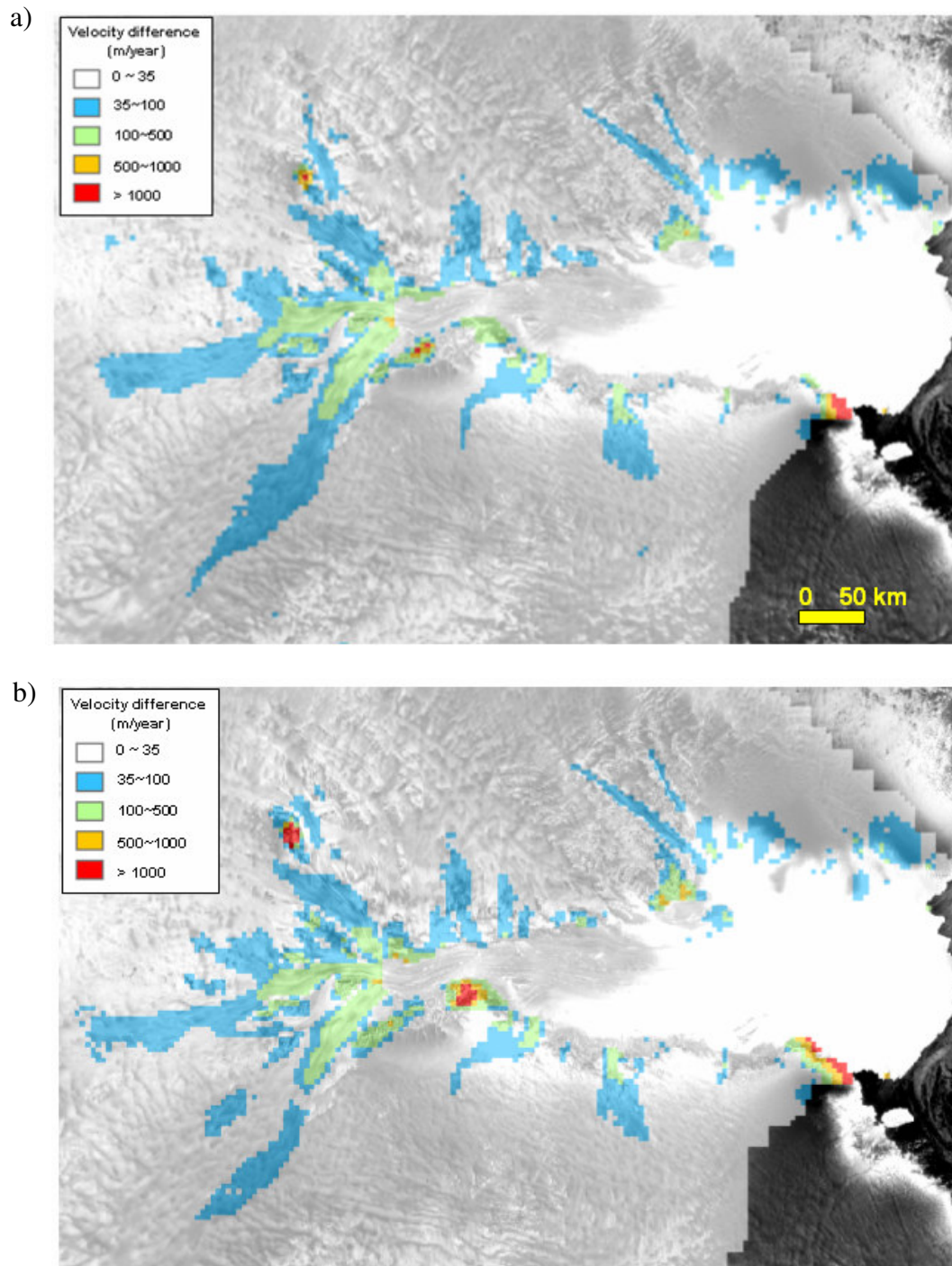
Figure 5.12 Velocity difference between the balance velocity from Budd and Warner (1996) and InSAR velocity (a), and between the balance velocity from this study and InSAR velocity (b).

On the other hand, the velocity difference can explain the current balance state of the Lambert Glacier - Amery Ice Shelf system. As it mentioned above, the downstream area is not reliable in terms of explaining the balance state. The mass imbalance map is created based on the velocity differences between the balance velocity of this study and the InSAR ice depth velocity (Figure 5.13). A positive imbalance occurs where the balance velocity is higher than the InSAR velocity and a negative imbalance where the InSAR velocity is higher than the balance velocity. Since balance velocity for the ice shelf area is not reliable, only grounded ice is considered for mass imbalance.

The most of the upstream area and accumulation catchment area is in balance. The mountain area is the major source of the positive imbalance. The ice stream areas are the negative imbalance. The confluence of the Lambert, Mellor, and Fisher area shows a especially large negative imbalance near a grounding line.
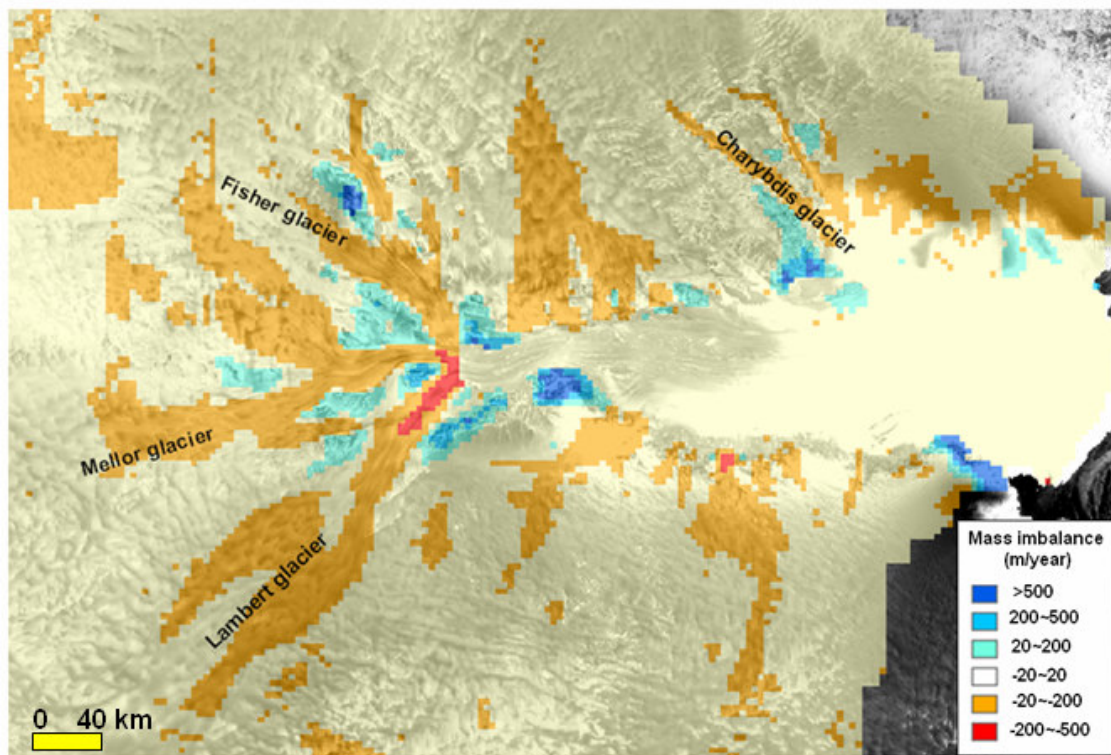
Figure 5.13 Mass imbalance map of Lambert Glacier system grounded ice area.

## CHAPTER VI

## MASS BALANCE ANALYSIS

### 6.1. Overview

The mass balance of ice sheets is important because major changes in their dimensions affect the climate and sea level globally. Methods for ice sheet mass balance calculations can be classified into 3 types (Patterson 1994): calculation of balance terms, comparison of mass flux and accumulation rate, and measurement of changes in ice thickness. The calculation of balance terms calculates every input and output components in a mass balance system using all available data and methodology. Patterson (1994) listed accumulation as a positive input term, and calving, surface ablation, and melting as major negative terms for mass balance calculations. This method has certain limitations in data quality due to lack of in-situ measurements for negative input terms, and is not appropriate for glacial basins that discharge ice mass into an ice shelf.

The comparison of the mass flux and accumulation rate method, also called mass-flux (mass budget) method, is the most commonly used mass balance calculation method for the Antarctic ice sheet. This method avoids the difficulty in determining calving rates. The ice flux per unit width is the ice thickness multiplied by the depth-averaged velocity. This velocity can range from about 70 % to 100 % of the measured surface velocity depending on the relative proportions of ice deformation and basal motion. However, most of the ice is discharged through the ice shelves, where the velocity at depth is equal to the surface velocity. The flux can be measured across the

grounding line where the need to estimate basal melting is eliminated. This method is simply a comparison between the flux across the grounding line and the accumulation over the grounded part of the basin.

Measurement of changes in ice thickness uses repeated elevation measurements of marker set in the ice. Surface elevation measurements should be converted to ice thickness to calculate changes in ice mass. If the elevation represents a short-term change in snowfall, it should be multiplied by the ratio of the density of near-surface snow to the density of ice. If it represents a long-term change, which is more interesting, the base of each marker should be set below the firn-ice transition. Thickness changes can be determined by comparing accumulation rates with the submergence velocity. Repeated surface elevation measurements, and changes in surface elevation can be obtained by averaging thousands of individual measurements at crossovers widely spaced in time using satellite techniques such as radar altimetry and laser altimetry.

The GIS based mass balance calculation was introduced by Bindschadler *et al.* (1993). This method is based on the theoretical background of the mass flux method. It deals with the mass balance at individual point, whereas the flux method only treats one flux gate in a basin. This point or pixel-based method enables the analysis of spatial distribution of mass balance as well as thickening and thinning spatial variations. The basal melting and ice-depth average ice velocity need to be determined in order to calculate the ice flux in each cell, since its flux gate is at the micro-scale (one pixel).

This study provides the mass balance calculations from the GIS ice mass balance model and mass flux methods under the assumption of steady-state conditions. As

mentioned before, basal melting and vertical velocity distribution should be taken into account to calculate the mass balance of each cell GIS based mass balance calculation. But in most of the cases, basal melting is negligible compared with the surface ablation unless the ice is floating (Paterson 1994). Therefore, the GIS based mass balance distribution is valid only for the grounded ice unless good basal melting rates are known.

With the assumption of two dimensional movement, plastic, and laminar ice motion in steady state, the velocity at any depth along the central axis can be estimated by assuming that shear stress is proportional to depth and that the strain rate directly relates to that stress. The internal vertical velocity profile of a glacier in a longitudinal section should show a decreasing rate of flow from the surface to the bedrock floor (Nye 1952). Since the velocity distribution is a function of the shear stress, the surface velocity can represent the velocity through the entire ice thickness when the basal shear stress is negligible (Bindchabler *et al.* 1993). This study takes the ice depth average velocity factor of 0.87 (Budd and Warner 1998).

**6.2. Previous studies**

Allison (1979) estimated the mass balance of the Lambert Glacier Drainage Basin based on ice movement measurements at ground stations in Prince Charles Mountains. The Lambert Glacier Drainage Basin is the part of the system that drains the major ice streams entering Amery Ice Shelf. It does not include ice streams that drain the western or eastern margins of the Amery Ice Shelf. He estimated the positive mass balance of 12 Gt $a^{-1}$ on the basis of flux calculations. The total accumulation for the interior portion of the basin upstream from the ground station line was informed to be 60 Gt $a^{-1}$, and discharge across the ground station line in upstream was estimated at 29.7 Gt $a^{-1}$. Allison estimated an additional mass loss of 18 Gt $a^{-1}$ from the ice streams converging into the Amery Ice Shelf.

Bentley and Givinetto (1991) estimated the imbalance of the Lambert-Amery system as part of mass balance of Antarctica study. Surface accumulation was calculated based on the data from the 1968-70 ANARE surveys (Budd *et al.* 1982) and McIntyre's (1985) reinterpretation of surface mass input data. Bentley and Givinetto (1991) obtained a positive mass imbalance of 39 Gt $a^{-1}$ for the Lambert drainage basin.

Fricker *et al.* (2000) computed balance flux for the entire Lambert-Amery system based on ERS-1 satellite radar altimeter surface elevations (Fricker *et al.* 2000) with six different of accumulation data sets. They also calculated the mass balance between a traverse line (LGB) in the upstream area and the ground station line (GL) in the downstream area using in-situ measurements. They concluded that the mass balance between the two transects is positive and it is not possible to accurately determine the

state of balance of large Antarctic drainage basins based on the currently available accumulation data.

Rignot (2002) calculated the mass balance for the three major glaciers of Lambert Glacial Basin as part of mass balance study of nine East Antarctic glaciers. He extracted surface ice velocity using RADARSAT-1 speckle tracking method. Total snow accumulation was based on two digital accumulation maps (Givinetto and Zwally 2000, Vaughan *et al.* 1999). BEDMAP (Lythe *et al.* 2000) and ERS DEM are used to calculate ice flux through grounding line. His analysis suggested that the glacier system close to balance of -2 ± 4.66 km$^3$ ice a$^{-1}$. The grounding line ice flux is 57.5 ± 5 km$^3$ ice a$^{-1}$ and calculated mass input is 55.2 ±1 km$^3$ ice a$^{-1}$.

Although many studies on mass balance of Lambert Glacier basin have been conducted, the previous studies only focused on the mass balance of the confluence Lambert Glacier, which accounts for only 60 % of Lambert Glacier–Amery Ice Shelf System in terms of surface accumulation. No study has investigated the sub-basin scale of mass balancer for entire Lambert Glacier–Amery Ice Shelf System. This study will provide the mass balance of all sub-basins draining its ice mass into the Amery Ice Shelf. In addition, newly extracted ice velocities will increase the accuracy of the mass balance study. Furthermore, the new ice velocity field enables the GIS based mass balance study which can to give detailed picture of ice thickening and ice thinning within the basin.

## 6.3. Methods

### 6.3.1 Mass budget method

As described before, the mass budget method compares the mass input and the mass output in the glacier system. All the mass in a glacier basin drains to the ice shelf through the grounding line. The major mass input source of the glacier basin system is surface accumulation. The basal melting and ice flux passing though grounding line are the major output of the glacier basin system (Figure 6.1). For grounded ice flow, the basal melting amount is negligible, compared with the surface ablation (Paterson 1994). Therefore, the mass output should be ice flux passing through grounding line.

To calculate the flux across the grounding line an imaginary flux gate is placed along the grounding line (Figure 6.1). If surface velocities and ice thicknesses along the grounding line are available, the flux can be calculated as sum of the flux at each pixel across the gate. The flux gates are aligned perpendicular to the flow direction. Therefore, the total flux through the grounding line is;

$$\Phi_{out} = \sum_{i=1}^{N} H_i \times W_i \times V_i \qquad (6.1)$$

where $H_i$, $W_i$, and $V_i$ denote ice thickness, pixel width perpendicular to the flow direction, and ice flow velocity of pixel $i$ along the flux gate. The mass balance of the entire glacial basin can be calculated by comparing the total accumulation of the area and the total outflux passing through the grounding line.

The random error of flux calculation and mass balance calculation is estimated based on the standard statistical theory of error propagation (Taylor 1997). From the

equation 6.1, there are two parameters that have errors in input data; ice thickness and ice flow velocity. By applying multiplication error propagation, the random error ($\sigma_{flux}$) of flux calculation can be estimated as

$$\sigma_{flux} = \sqrt{(W^2 V^2 \sigma_H^2 + W^2 H^2 \sigma_V^2)} \qquad (6.2)$$

where W denotes the cell size, V denotes ice velocity, H denotes ice thickness, $\sigma_H$ and $\sigma_V$ denote the errors of ice thickness and ice velocity, respectively. Since the mass balance calculation is based on simple subtraction between the two parameters of ice flux and surface accumulation, the addition/subtraction error propagation equation can be applied to calculated the random error of mass balance ($\sigma_{mass\_balance}$) as

$$\sigma_{mass\_balance} = \sqrt{\sigma_{flux}^2 + \sigma_{accum}^2} \qquad (6.3)$$

where $\sigma_{flux}$ and $\sigma_{accum}$ denote the errors of ice flux and surface accumulation, respectively.
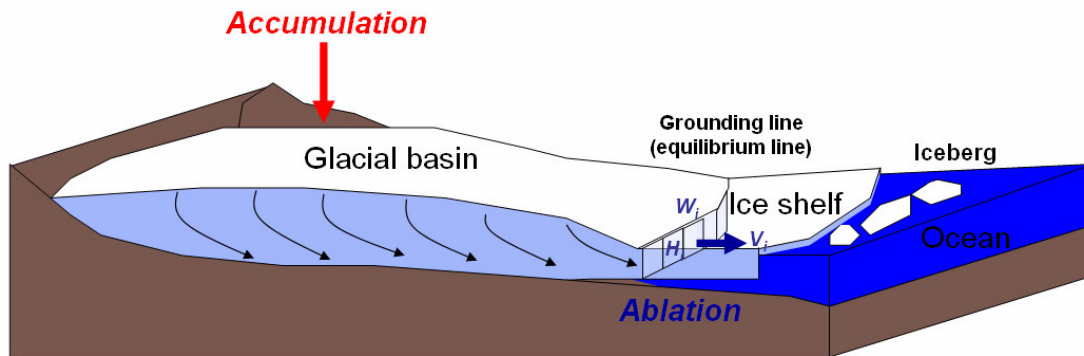


Figure 6.1 Schematic diagram showing concept of mass budget method and flux gate at grounding line.

**6.3.2. GIS based net mass balance**

A raster-based GIS system enables us to model the ice mass balance at each grid cell at the basin scale (Bindchadler *et al*. 1993). The net mass balance for any grid cell is calculated by summing the normal component of mass flux across each of the four vertical faces and adding the mass contributions from the top and bottom surfaces (Bindchadler et al., 1993):

$$N = \rho \left[ \sum_{\substack{vertical \\ faces}} Q_n + (A - B) W_x W_y \right] \tag{6.4}$$

where N is the net mass balance, $\rho$ is the density of ice (917 kg m$^{-3}$), $Q_n$ are the volume fluxes across each of the four vertical faces, $W_x$ and $W_y$ are the widths in the x and y directions, A is surface accumulation and B is basal melting (Figure 6.2). Ice-thickness and velocity values are specified at each grid point, while the vertical faces of each grid cell occur between grid points. Thus midpoint approximations are used to calculate the mass flux from the grids of ice thickness and ice velocity (Bindchadler *et al.* 1993):

$$Q_n \left( i \pm \frac{1}{2}, j \right) = \mp \frac{1}{4} \left[ H(i \pm 1, j) + H(i, j) \right] \cdot \left[ U_x(i \pm 1, j) + U_x(i, j) \right] W_y$$

$$Q_n \left( i, j \pm \frac{1}{2} \right) = \mp \frac{1}{4} \left[ H(i, j \pm 1) + H(i, j) \right] \cdot \left[ U_y(i, j \pm 1) + U_y(i, j) \right] W_x \tag{6.5}$$

where i and j are grid coordinates, H is the ice thickness, and $U_x$ and $U_y$ are the components of velocity in the x and y directions. The grid will be aligned the positive y-axis with the 180° meridian and the positive x-axis with 90°E. With this orientation, the velocity components are calculated from the velocity vector by the formulas (Bindchadler *et al.* 1993):

$$U_x(i,j) = \left|\vec{U}(i,j)\right| \sin\left[\theta(i,j) + \phi(i,j)\right]$$

$$U_y(i,j) = \left|\vec{U}(i,j)\right| \cos\left[\theta(i,j) + \phi(i,j)\right]$$

(6.6)

In addition, the net mass balance in terms of ice-equivalent thickening or thinning can be expressed by the following formula (Bindchadler *et al.* 1993):

$$\frac{dH}{dt} = \frac{N}{(W_x W_y \rho)}$$

(6.7)
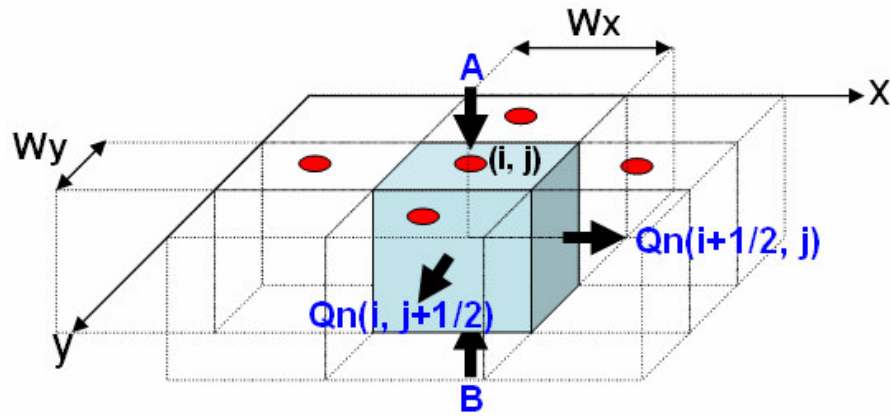


Figure 6.2 Diagram of scheme to compute net mass balance for a grid cell centered at grid point (i,j) (Bindchadler *et al.* 1993).

## 6.4. Sub-basin delineation

Flow lines and drainage basin are important concepts in glaciology. Basin delineation is one of the most important components in mass balance calculation, since mass input for the basin depends on the area of the basin. Ice flow is driven by gravity force from

surface and basal slopes (Paterson 1994). A flow line in glacier system is the surface projection of the path that an individual ice particle would take in moving through the system (Fricker *et al.* 2000). The tangent at any point along a flowline matches the direction of the velocity vector at the point. All the ice flowing through a section transverse are originated from the up-slope catchment area bounded by the two flowlines that pass through the end points of the transverse section. Flow lines can be used to delineate catchments.

All the currently available drainage basin boundaries and flow lines are generated from DEMs based on maximum surface slope. Because of local topographic variation, DEMs must be smoothed on an appropriate spatial scale. The smoothing scales ranges from 10 km to 35 km (Vaughan *et al.* 1999, Fricker *et al.* 2000, Liu *et al.* 1999), and loss of topographic detail is inevitable. The coarse spatial resolution from the smoothing limits detection of small ice streams, ice flow in flat surface topography and topographic variations because the cell size should be 10 times as large as the average ice thickness to satisfy the basic assumption of the ice flow direction from DEM (Paterson 1994). The flow direction information from SAR interferometry provides accurate ice flow direction. Since flow direction is based on arctangent of x and y directional surface movement, it is very sensitive to errors in surface movement. When the flow speed is high, the flow direction is reliable.

This study combines the flow direction from SAR interferometry for high velocity areas and the flow direction from surface DEM derived from ICESat laser altimetry data for low velocity but relatively high elevation areas. The ICESat laser

altimetry points are interpolated into 10 km grid and depressionless DEM is created using Arc/Info GRID function (Figure 6.3). The boundary of the Lambert Glacier–Amery Ice Shelf System is delineated using ICESat laser altimetry DEM (Figure 6.3).

The direction grid from SAR interferometry is clipped based on the velocity threshold of 10 m/year considering the error range of ice velocity (2 ~ 8 m/year). In addition, the manual delineation of clip area is carried out to remove outliers based on surface features since the direction grid has considerable errors in high elevation area. The flow line extraction from InSAR direction grid confronts a new problem of circular flow pattern in some areas. An algorithm is developed to force the glacier to flow into the nearest outlet. The extracted flow direction grid is converted into 8-directional grid and merged with DEM flow direction grid to extract sub basins using "WATERSHED" algorithm in Arc/Info GRID function (Figure 6.4).

Along the grounding line, eight major sub glacier systems are identified; Lambert Glacier, Mellor Glacier, Fisher Glacier, West tributary Glacier, East tributary Glacier, Charybdis Glacier area, West downstream glacier, and East downstream glacier (Figure 6.5). A transect line is placed along the grounding line for each sub glacier system as discharge gate to identify its corresponding catchment area. The output sub-basin contains errors, because its 8-directional characteristics can not adequately describe small variations in flow direction. The obvious errors, such as ice divides cutting through ice stream, have been manually corrected based on surface features overlaid with flow direction arrow.
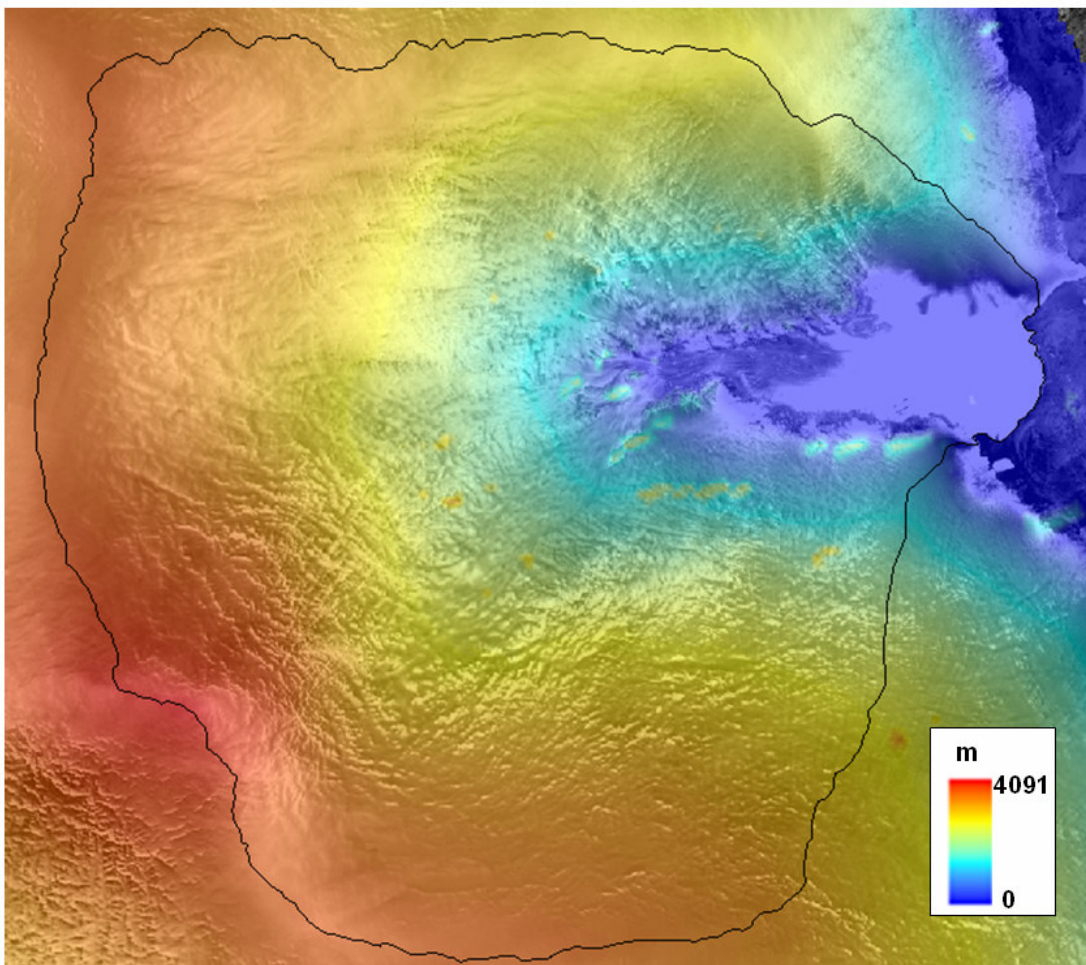
Figure 6.3 Digital Elevation Model draped on the SAR image mosaic over the Lambert

Glacier– Amery Ice Shelf system created from ICESat laser altimetry data.
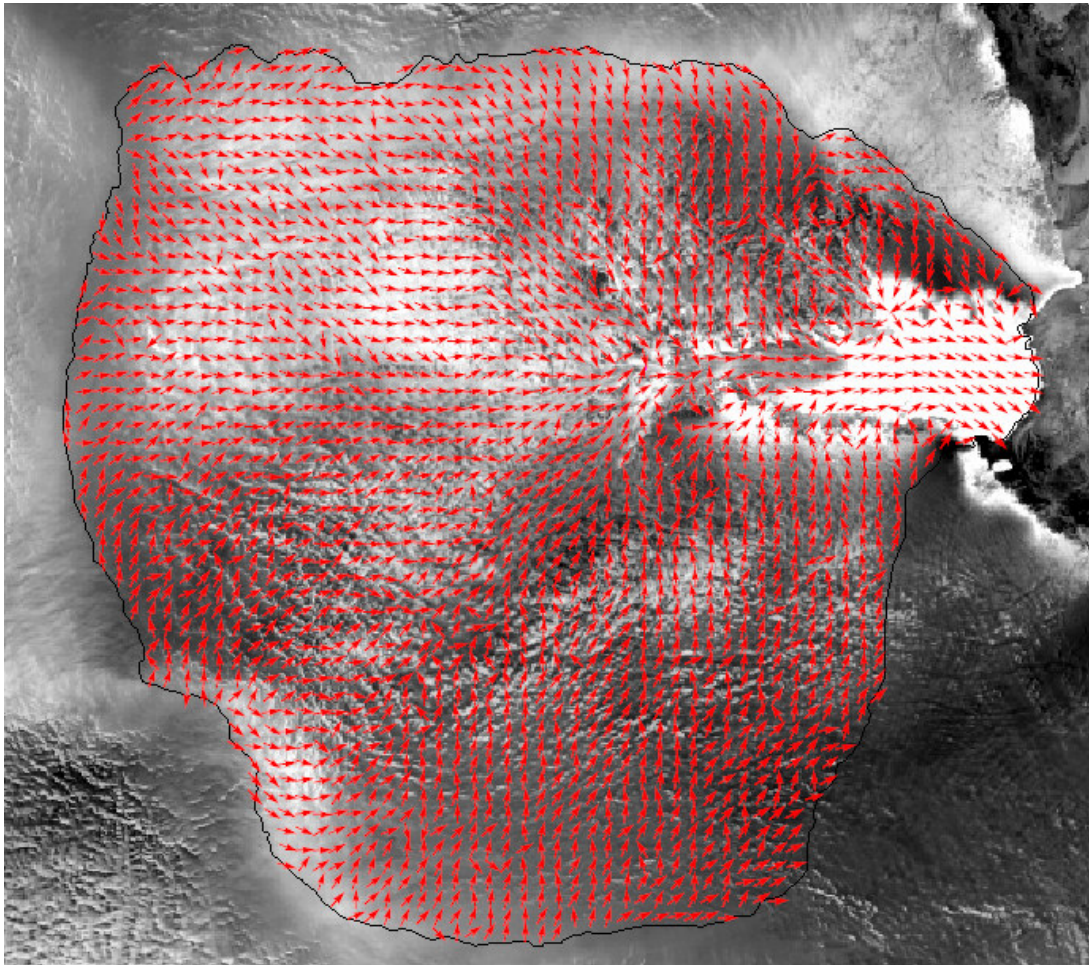
Figure 6.4 8-directional flow direction from combined InSAR and DEM flow direction grid.

As a result, eight major sub-basins and two small mountain areas that are not contributing ice mass are delineated (Figure 6.5). The drainage basin contributing ice mass to the Lambert Glacier– Amery Ice Shelf system is $1427 \times 10^3 \, km^2$ including the Amery Ice Shelf. The total area which the ice mass is passing the main grounding line (named T Lambert Glacier in this chapter) located at the confluence area of Lambert, Mellor, and Fisher glacier accounts for 66.62 % of the entire Lambert Glacier– Amery

Ice Shelf system. If the Amery Ice Shelf is excluded, this percent is increased to 69.67 %. Previous mass balance study did not consider the remaining 30.33 % of catchment area of the Amery Ice Shelf (Table 6.1). The catchment areas of the east tributary glacier and west tributary glacier accounts for 13.27 % and 6.54 % of the entire drainage basin of the Amery Ice Shelf.
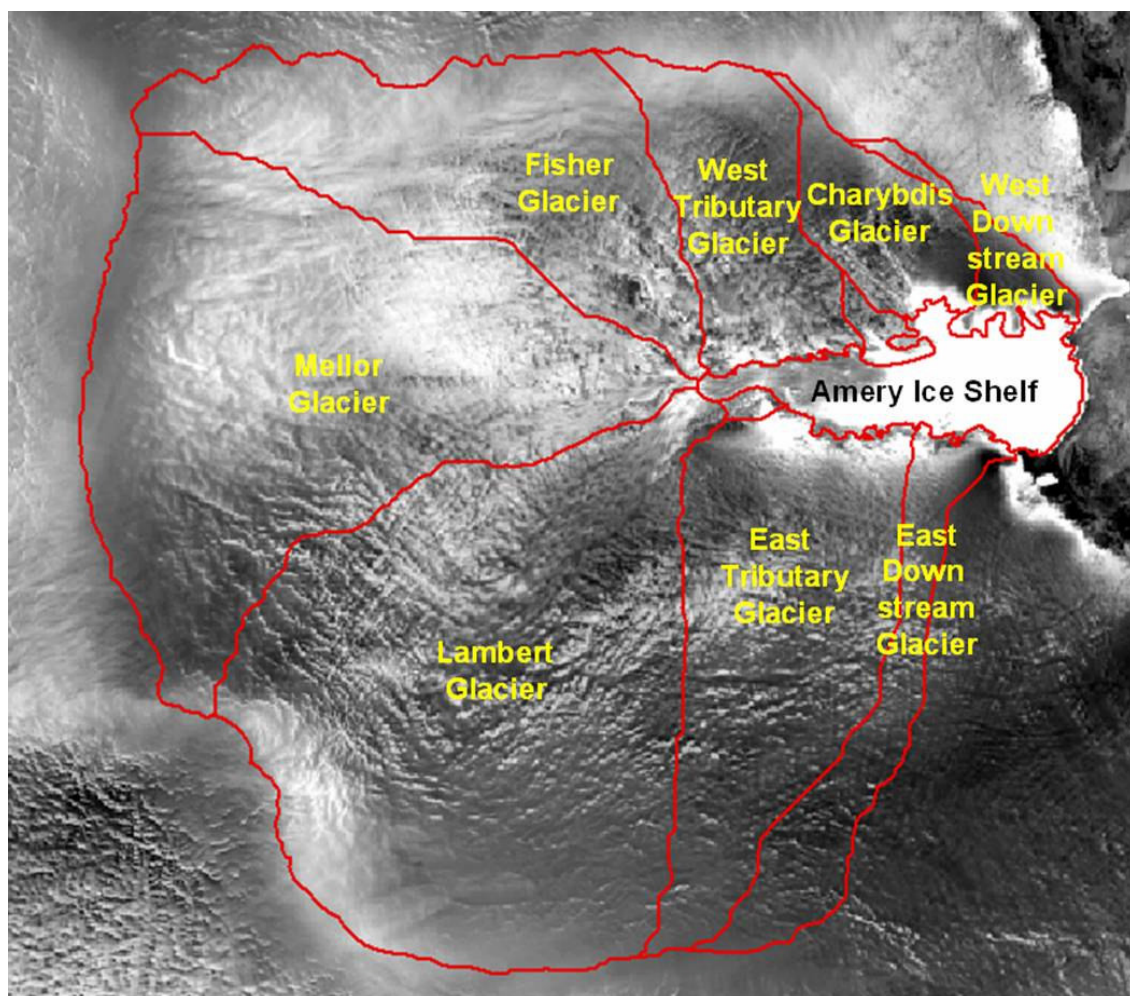


Figure 6.5 8 major sub-basins of the Lambert Glacier– Amery Ice Shelf system.

Table 6.1 Area of sub-basins and ice shelf of the Lambert Glacier– Amery Ice Shelf system.

| Sub Basin | Area (km$^2$) | Area (%) with Ice shelf | Area (%) without Ice shelf |
|---|---|---|---|
| T Lambert Glacier | 951363 | 66.62 | 69.67 |
| Lambert Glacier | 410440 | 28.74 | 30.06 |
| Mellor Glacier | 359668 | 25.19 | 26.34 |
| Fisher Glacier | 178420 | 12.49 | 13.07 |
| East Tributary Glacier | 181255 | 12.69 | 13.27 |
| West Tributary Glacier | 89325 | 6.26 | 6.54 |
| East Downstream | 67097 | 4.70 | 4.91 |
| Charybdis Glacier Area | 48138 | 3.37 | 3.53 |
| West Downstream | 21137 | 1.48 | 1.55 |
| Jetty Peninsula Area | 7228 | 0.51 | 0.53 |
| Mawson Escarpment Area | 2882 | 0.20 | 0.21 |
| Amery Ice Shelf | 62345 | 4.37 | |
| TOTAL | 1427935 | 100.00 | 100.00 |

## 6.5. Input data of mass balance calculations

Accumulation is considered as mass input in the mass balance calculation. In addition, mass flux calculation requires ice velocity, ice thickness information. This study uses InSAR derived surface velocity data as major source of ice velocity, and the published surface accumulation and ice thicknesses.

### 6.5.1. Surface accumulation data

The most recently published net surface accumulation rates were provided by Giovinetto and Zwally (2000) and Vaughan *et al.* (1999).

Giovinetto and Zwally (2000) created a contour map showing the spatial distribution of net mass accumulation for the Antarctic ice sheet based on 5365 grid points in 50 km spacing from visual interpolation of approximately 2000 in-situ measurements. Net surface mass balance map of Vaughan *et al.* (1999) in a 10 km resolution grid was derived from passive microwave satellite data with 1800 in-situ measurements. Although both studies used the same in-situ measurements, they show noticeable difference because of different interpolation schemes. The comparison shows that two data sets are coherent in continental scale, but different at regional scale (Giovinetto and Zwally 2000).

Since the selection of the accumulation rates is very critical in mass balance calculation, spatial resolution and accuracy should be considered in data selection depending on the scale of mass balance calculation. The stated error range of Vaughn *et al.* (1999) accumulation data is ±5 %. Giovineitto and Zwally (2000) compared the two accumulation data sets. They found that 40 % of the area shows more than 22 % difference between the two (1999). Rignot (2002) used average value between the two, and showed that there is standard deviation of ± 1 $km^3$ ice $a^{-1}$.

However, this study calculates the mass balance of sub-basins and pixel level GIS based mass balance calculation. The spatial resolution of 50 km (Giovinetto and Zwally 2000) is not appropriate for the purpose since only several point can determine

the accumulation if the sub-basin is small. Using average value between the two is not considered, since the accumulation can be biased and lose consistency with the location. Thus this study resampled 10 km accumulation grid from Vaughn *et al.* (1999) to 400 m for the consistency in mass balance and flux calculation using bilinear interpolation (Figure 6.6).
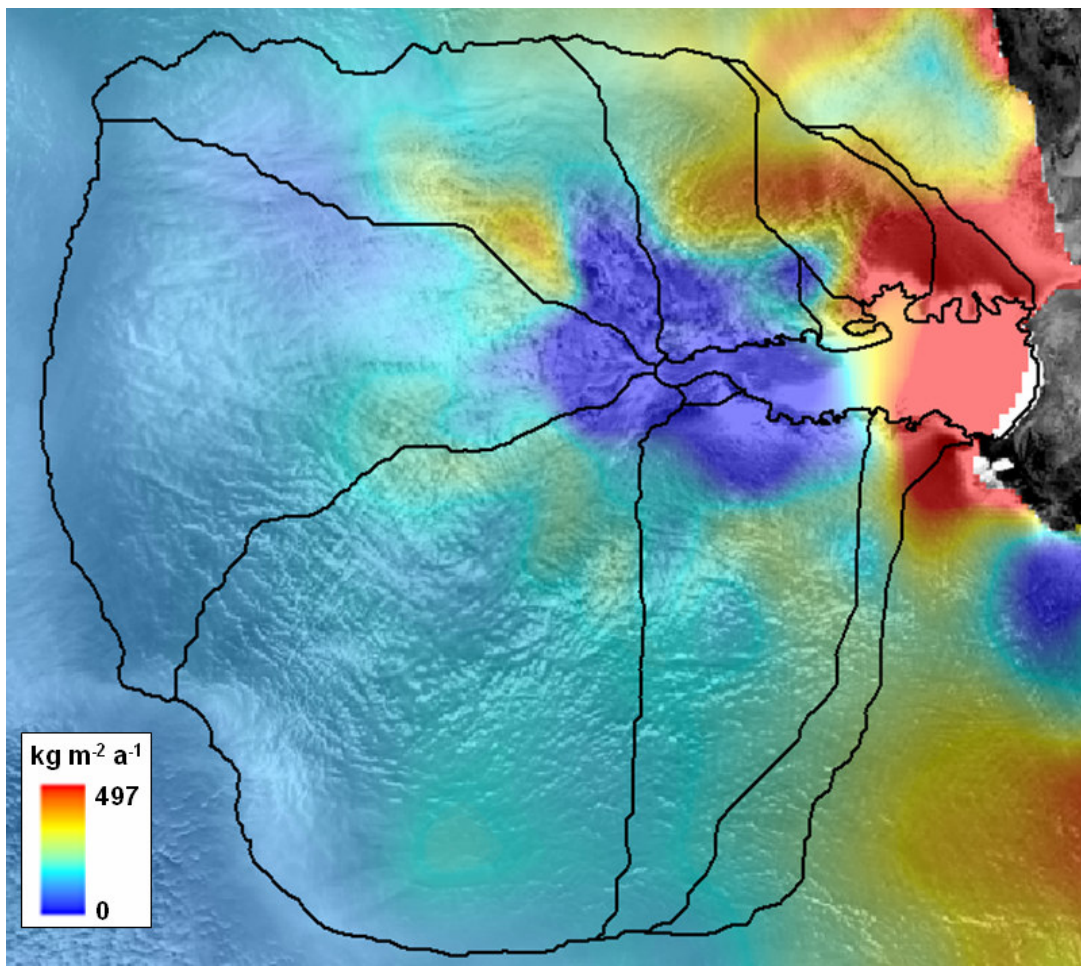


Figure 6.6 Resampled surface accumulation map draped on SAR image mosaic (Vaughn *et al.* 1999)

**6.5.2. Ice thickness**

The ice thickness data used in this study are obtained from the BEDMAP project (Lythe *et al.* 2001). The data are derived from more than 150 independents surveys, conducted by 15 nations, over the past 50 years. Compared to other parts of Antarctica, the Lambert Glacial Basin-Amery Ice Shelf system has the densest data coverage, where ground based Radar Echo Sounding and Airborne Radar Echo Sound data have 5 km to 10 km track-spacing. The thickness precision for these surveys ranges from 30 m to 100 m for the Lambert Glacial Basin and crossover analysis shows that around 58% of crossover errors are less than 20 m, 73% are less than 50 m, and 84% are less than 100 m. This indicates that the majority of crossover errors fall within typical navigational and measurement uncertainties (Lythe *et al.* 2001). The spatial resolution of ice thickness grid is 5 km. It is resampled to 400 m for this study using bilinear interpolation (Figure 6.7).
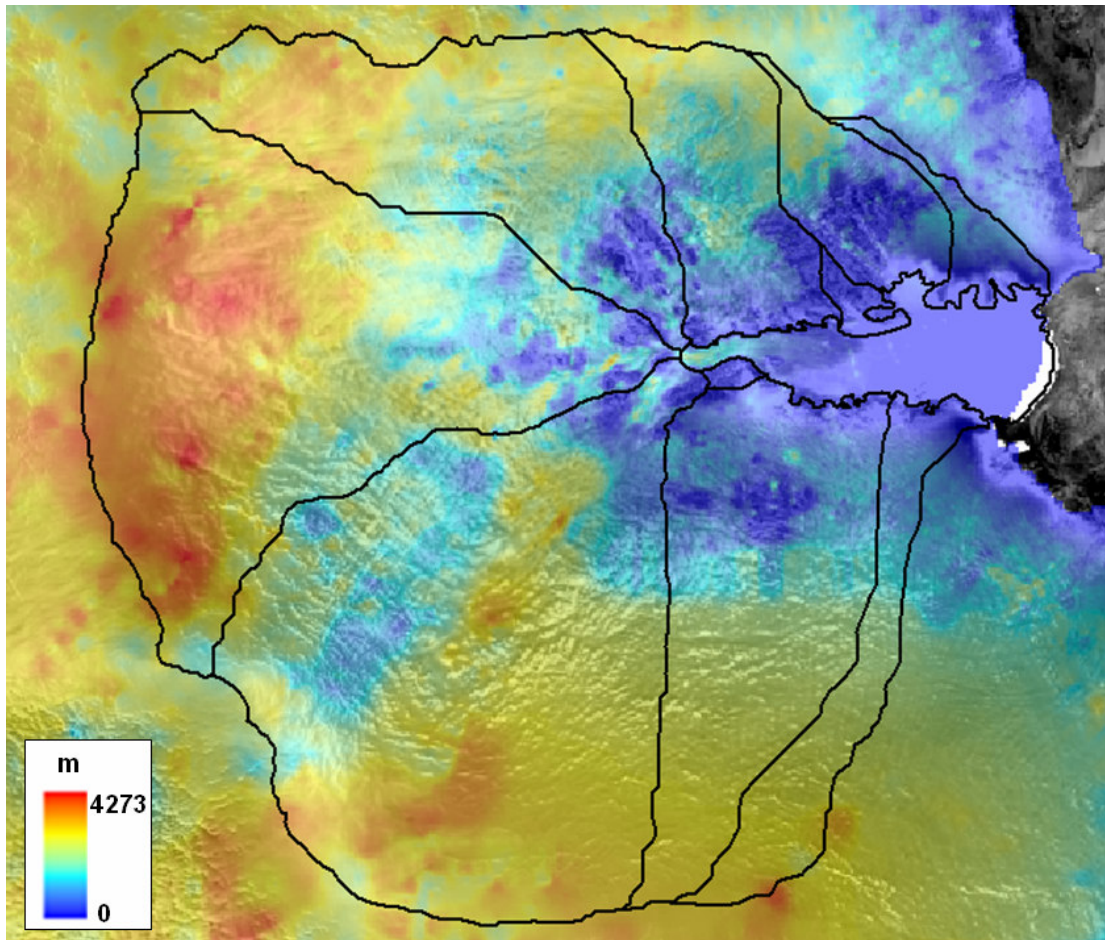
Figure 6.7 Resampled and interpolated ice thickness map of the Lambert Glacier–Amery Ice Shelf system draped on SAR image mosaic.

## 6.6. Sub-basin scale mass balance and basal melting

### 6.6.1. Flux gate placement

The mass budget method is used for sub-basin scale mass balance calculation. The mass budget method requires total accumulation of the sub-basin and the mass flux flowing out through the grounding line of the sub-basin. This study placed eight flux gates for each major ice stream: Lambert, Mellor, Fisher, East tributary, East downstream,

Charybdis, West tributary, and West downstream Glaciers (Figure 6.8). The flux gates are located along or near the grounding lines keeping the flux gate direction perpendicular to the flow direction. The flux gates of Lambert, Mellor, and Fisher Glaciers are located at the confluence area so that the flux total of Lambert, Mellor, and Fisher Glaciers can represent the ice flux for the Lambert Glacier Basin. The glacier below the confluence area is denoted by T Lambert Glacier, and its mass flux includes grounded ice of Lambert, Mellor, and Fisher Glaciers. The flux gate is placed discontinuously to cover only the actual outflux for W tributary, W down, and E tributary Glaciers.

Four cascading flux gates are placed in the Amery Ice Shelf to calculate basal melting of the ice shelf (Figure 6.8). The first gate is placed about 42 km down-stream from the front of T Lambert flux gate to monitor the basal melting of main grounding zone. The second gate is placed at the north end of the Jetty Peninsula to calculate basal melting of the middle section of the stream with the mass contributed by West and East tributary glaciers. The third flux gate is located at the mouth of ice stream from Charybdis Glacier merging into the Amery Ice Shelf for calculation of basal melting of Charybdis Glacier area grounding zone. Finally, the last flux gate is located about 20 km inside of Amery Ice Shelf Front due to limitations of surface accumulation and ice thickness data coverage in the region. This flux gate acts as basal melting detector of the downstream end of the Amery Ice Shelf.
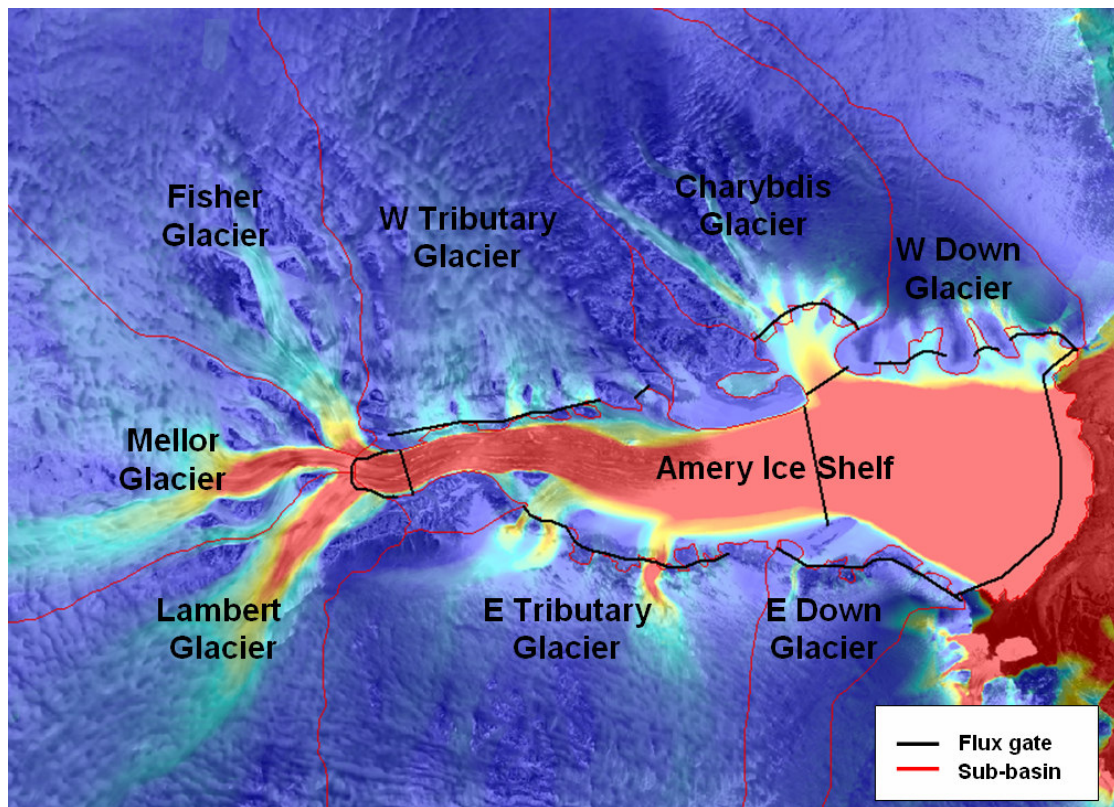
Figure 6.8 Flux gate locations for mass balance and ice shelf basal melting calculation overlaid on surface velocity field.

## 6.6.2. Surface Accumulation of sub-basins

The surface accumulation grid discussed in chapter 6.5 is used to calculate total mass input for each sub-basin. The catchment area for each flux gates located on Amery Ice Shelf is shown in Figure 6.9. The Mass flux is not calculated for the Mawson Escarpment area and the Jetty Peninsula bains, but the snow accumulation in these two small basins are included into mass balance calculation for the entire Amery Ice Shelf.

The total accumulation of eight major sub-basins is 90.54 ± 1.55 Gt/year. Since the accumulation increases towards the coast, accumulation is highest the northern sub-

basins. The total snow accumulation for the Lambert, Mellor, and Fisher glacier accounts for just 56.48 % of total accumulation, but comprises 69.67 % of the total area. Notably, Charybdis Glacier area and East down stream Glacier show relatively higher snow concentration accounting for 9 % and 7.88 % of total accumulation, despite only having 3.53 % and 4.91 % of basin areas, respectively. Tributary glaciers located near shore play important role in mass input of the system, and should not be ignored in mass balance calculation of the Lambert Glacier– Amery Ice Shelf system. The snow accumulation result is summarized in Table 6.2. The snow accumulation for the ice shelf area is included in the ice shelf basal melting calculation.

Table 6.2 Surface accumulation of sub-basins in the Lambert Glacier– Amery Ice Shelf system.

| Sub Basin | Accumulation (Gt/year) | Error (Gt/year) | Accumulation (%) |
|---|---|---|---|
| T Lambert | 51.138 | ± 1.263 | 56.48 |
| Lambert | 23.186 | ± 1.159 | 25.61 |
| Mellor | 17.073 | ± 0.854 | 18.86 |
| Fisher | 10.879 | ± 0.544 | 12.02 |
| W Tributary | 7.403 | ± 0.370 | 8.18 |
| Charybdis | 8.155 | ± 0.408 | 9.01 |
| W down | 5.693 | ± 0.285 | 6.29 |
| E tributary | 11.031 | ± 0.552 | 12.18 |
| E down | 7.124 | ± 0.356 | 7.87 |
| Total | 90.544 | ± 1.553 | 100.00 |
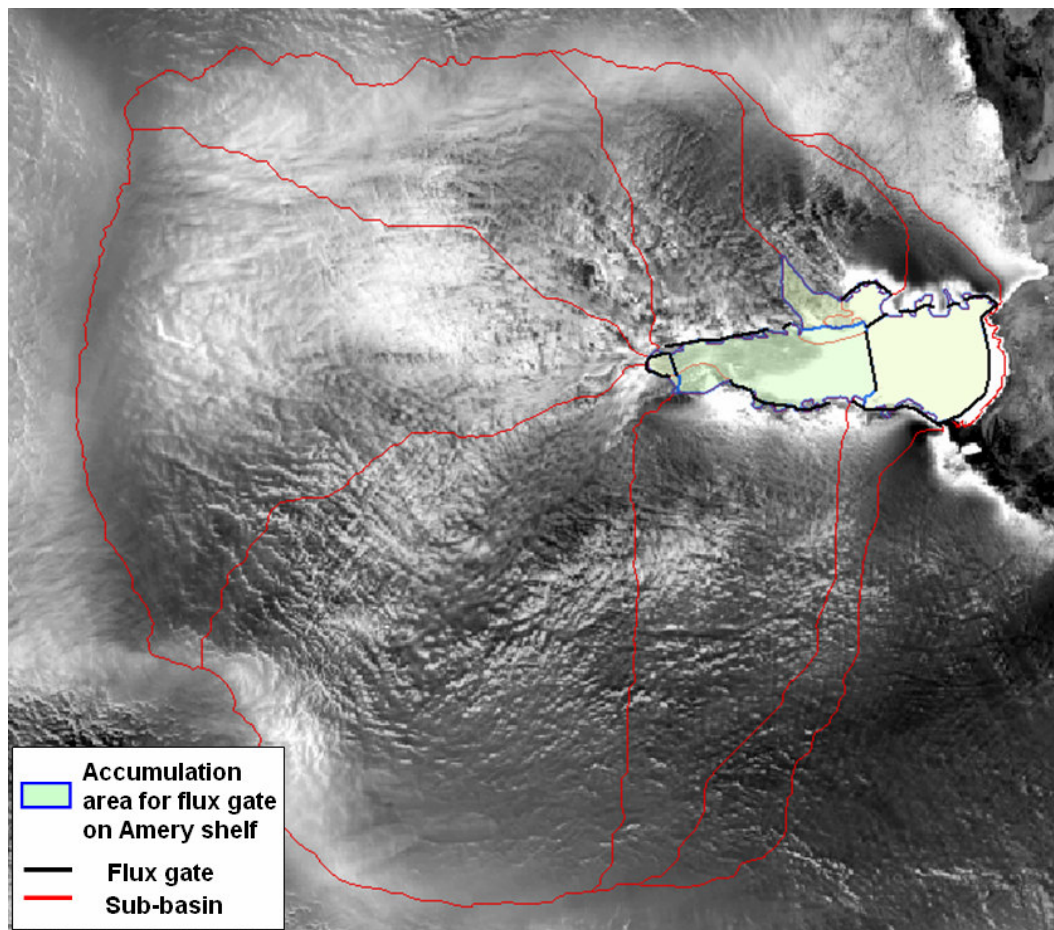
Figure 6.9 Boundary of accumulation area for sub-basins and basal melting flux gates.

**6.6.3. Ice mass flux of sub-basins in the Lambert Glacier– Amery Ice Shelf system**

The ice flux from each sub-basin is considered as mass output from the sub-system. Therefore, the total ice flux from eight sub-basins discharges into the Amery Ice Shelf and, eventually, contribute the mass into the ocean by basal melting and ice calving. The total ice flux discharged to Amery Ice Shelf from grounded ice is 95.64 ± 2.89 Gt/year (Table 6.3). The total ice flux from T Lambert Glacier makes up 60.81 % of total ice mass. Compare to its size, the ice flux contribution is less than its share of basin size. The general pattern of ice flux for each sub-basin is closely related to surface accumulation. High accumulation rate results in high ice flux contribution except for East down stream glacier (Table 6.3).

Table 6.3. Ice mass flux for sub-basins in the Lambert Glacier– Amery Ice Shelf system.

| Sub Basin | Flux (Gt/year) | Error (Gt/year) | Flux (%) |
|---|---|---|---|
| T Lambert | 58.769 | ± 2.329 | 61.45 |
| Lambert | 25.501 | ± 1.833 | 26.66 |
| Mellor | 22.595 | ± 1.100 | 23.63 |
| Fisher | 10.673 | ± 0.925 | 11.16 |
| W Tributary | 7.922 | ± 1.502 | 8.28 |
| Charybdis | 8.555 | ± 0.874 | 8.95 |
| W down | 4.894 | ± 0.726 | 5.12 |
| E tributary | 13.189 | ± 1.047 | 13.79 |
| E down | 2.309 | ± 0.419 | 2.41 |
| Total | 95.637 | ± 3.020 | 100.00 |

**6.6.4. Mass balance of sub-basins in the Lambert Glacier– Amery Ice Shelf system**

By comparing the total accumulation and total ice flux at the flux gate for each sub basin, the mass balance of each sub basin is calculated. The calculated mass imbalance can be converted into average ice thickness change rate by dividing the mass imbalance by the total area of each sub basin. The mass imbalance of eight sub basins provides the status of mass balance for the grounded ice of the Lambert Glacier– Amery Ice Shelf system.

The calculation reveals that the Lambert Glacier system has a slight negative imbalance of -5.09 ± 3.46 Gt ice $a^{-1}$ (Table 6.4). The total accumulation of the grounded ice of the system is 90.54 ± 1.55 Gt ice $a^{-1}$, and the total ice flux discharged into Amery Ice Shelf is calculated as 95.64 ± 3.02 Gt ice $a^{-1}$. The average ice thickness change rate is -0.0041 ± 0.003 m/year.

The T Lambert glacier has negative mass imbalance of -7.630 ± 2.65 Gt ice $a^{-1}$. The major reason for the T Lambert mass imbalance is Mellor glacier which has the mass imbalance of -5.52 ± 1.39 Gt ice $a^{-1}$. The Charybdis Glacier sub-basin loses the most ice mass and shows thickness change rate of -0.0091 ± 0.022 m/year. In general, most of the sub-basins have a negative mass imbalance, whereas Fisher and West down Glacier sub basins shows slight positive imbalances of 0.21 ± 1.07 Gt ice $a^{-1}$ and 0.80 ± 0.78 Gt ice $a^{-1}$, respectively. East down glacier has a relatively large positive imbalance number of 4.82 ± 0.55 Gt ice $a^{-1}$. The average thickness change rate shows the sub basins near coast are experiencing the apparent ice thickening because of high accumulation rate in coastal area and low ice flow velocities.

Table 6.4 Mass balance of eight major sub-basins and their average ice thickness change rate.

| Sub Basin | Accumulation (Gt /year) | Flux (Gt/year) | Mass Balance (Gt/year) | Area (km$^2$) | Average Thickness Change (m/year) |
|---|---|---|---|---|---|
| T Lambert | 51.14 ± 1.26 | 58.77 ± 2.33 | -7.63 ± 2.65 | 951363 | -0.0088 ± 0.003 |
| Lambert | 23.19 ± 1.16 | 25.50 ± 1.83 | -2.31 ± 2.17 | 410440 | -0.0062 ± 0.006 |
| Mellor | 17.07 ± 0.85 | 22.60 ± 1.10 | -5.52 ± 1.39 | 359668 | -0.0168 ± 0.004 |
| Fisher | 10.88 ± 0.54 | 10.67 ± 0.93 | 0.21 ± 1.07 | 178420 | 0.0013 ± 0.007 |
| W Tributary | 7.40 ± 0.37 | 7.92 ± 1.50 | -0.52 ± 1.55 | 89325 | -0.0064 ± 0.019 |
| Charybdis | 8.16 ± 0.41 | 8.56 ± 0.87 | -0.40 ± 0.96 | 48138 | -0.0091 ± 0.022 |
| W down | 5.69 ± 0.29 | 4.89 ± 0.73 | 0.80 ± 0.78 | 21137 | 0.0413 ± 0.040 |
| E tributary | 11.03 ± 0.55 | 13.19 ± 1.05 | -2.16 ± 1.18 | 181254 | -0.0130 ± 0.007 |
| E down | 7.12 ± 0.36 | 2.31 ± 0.42 | 4.82 ± 0.55 | 67097 | 0.0785 ± 0.009 |
| **Total** | **90.54 ± 1.55** | **95.64 ± 3.02** | **-5.09 ± 3.46** | **1355481** | **-0.0041 ± 0.003** |

### 6.6.5. Basal Melting of Amery Ice Shelf

The steady state basal melt rate of the ice shelves can be deduced by considering the flux difference between a flux gate at grounding line and the flux gate from downstream and accumulation between the two gates using a mass conservation equation (Rignot 2002). The difference in flux needs to be large enough compared to the precision in ice flux calculation. Flux gates should be placed near the boundary between the major ice-flow merging area for conveniently calculating input flux. The gate denoted "Basal 1" and "Basal 3" in Table 6.4 are used to calculate basal melting of T Lambert Glacier grounding zone and Charybdis Glacier grounding zone. The "Basal 2" and "Basal 4" are

the flux gates used to estimate basal melt rate of upstream and downstream of the Amery Ice Shelf which placed long distance apart.

The total basal melting in the grounding zone of T Lambert Glacier is estimated to be 21.64 ± 2.17 Gt ice $a^{-1}$, and the average melting rate is -19.19 ± 1.92 m/year for the grounding zone and upstream area of Amery Ice Shelf. Comparing the downstream and other grounding zones, the upstream experienced great basal melting accounting for about 30 % of total basal melting. The basal melting rate dramatically decreases to -0.85 ± 0.32 m/year as it moves to mid stream. The Charybdis Glacier area shows relatively small basal melting because of small input flux from tributary glaciers in Charybdis Glacier region. The result is summarized in Table 6.5.

Table 6.5 Basal melt rate of Amery Ice Shelf.

| Flux gate | Accumulation (Gt/year) | Flux input from upstream (Gt/year) | Flux down stream (Gt/year) | Total Basal Melting (Gt/year) | Area ($km^2$) | Average Basal Melting (m/year) |
|---|---|---|---|---|---|---|
| Basal 1 | 0.00003 | 58.77±1.83 | 37.13±1.15 | -21.64±2.17 | 1233 | -19.19±1.92 |
| Basal 2 | 1.31±0.07 | 58.24±2.17 | 18.09±1.70 | -41.46±2.75 | 25390 | -1.79±0.12 |
| Basal 3 | 1.18±0.06 | 8.56±0.87 | 6.994±0.57 | -2.74±1.05 | 3551 | -0.85±0.32 |
| Basal 4 | 8.77±0.44 | 32.29±1.98 | 16.35±3.11 | -24.72±3.71 | 28580 | -0.95±0.14 |

**6.7. GIS based net mass balance**

The raster based net mass calculation provides the micro-scale mass balance information by placing flux gates around the pixel boundary. The ice flux from upstream is taken as the mass input to the pixel, and the flux to downstream is regarded as output of the pixel. The ice flux difference is compared with surface accumulation to determine if the pixel is gaining the ice mass. By doing so, the ice thickening/thinning of the pixel can be inferred. The mass balance state of each sub basin can only provide the average ice thickening/thinning rate of the system. This pixel-based GIS method provides information of which part of the sub-basin makes positive or negative contribution to mass imbalance.

Although the ice thickening/thinning rate is different from the average ice thickening/thinning rate calculated by sub-basin mass balance calculation, the distribution of ice thickening/thinning rate shows valuable information about the ice mass distribution in the system. It shows that major negative imbalance is caused by ice thinning in downstream area where the velocity is increasing as the glaciers are discharged into the Amery Ice Shelf. The most of upstream region of glaciers and mountain area shows minimal ice thickening. Even the sub-basin is in negative imbalance, the Lambert and Mellor Glaciers have ice thickening in upstream regions, and it explains why the Mellor Glacier is the major contributor of negative mass imbalance as the ice thinning dominates for the most of the basin (Figure 6.10).

The ice thickening distribution of East and West downstream Glaciers explains the positive mass imbalance in sub-basin level. Especially, the distribution is consistent

with the West down stream glacier where the largest positive imbalance is estimated in mass budget method. The ice thinning and thickening in Amery Ice Shelf is not considered in result analysis since the basal melting is not incorporated in pixel level net mass balance calculation. However, it can emphasize the high ice thinning rate near main grounding line, and ice thinning rate decrease as it moves downstream.

The ice thickening/thinning grid shows consistent results with the result from the previous chapters. The ice thickening and thinning distribution is very similar to that of strain rate distribution where the extending flow creates the ice thinning and compressive flow creates ice thickening. In addition, this GIS based mass balance distribution shows the consistency with the balance velocity base mass imbalance map. Both of the mass imbalance maps identify the major ice stream as ice thinning contributor and the mountain and upstream area as ice thickening contributor. This result also explains the positive mass imbalance of high elevation area of the Lambert Glacier system (Fricker *et al.* 2000)

| m/year | |
|---|---|
| ⬛ red | 44.94 - 95.84 |
| ⬛ orange | 13.38 - 44.93 |
| ⬛ gold | 1.16 - 13.37 |
| ⬛ yellow | -1.90 - 1.15 |
| ⬛ light green | -6.99 - -1.91 |
| ⬛ teal | -19.21 - -7.00 |
| ⬛ cyan | -40.59 - -19.22 |
| ⬛ blue | -92.52 - -40.60 |
| ⬛ dark blue | -164.82 - -92.53 |
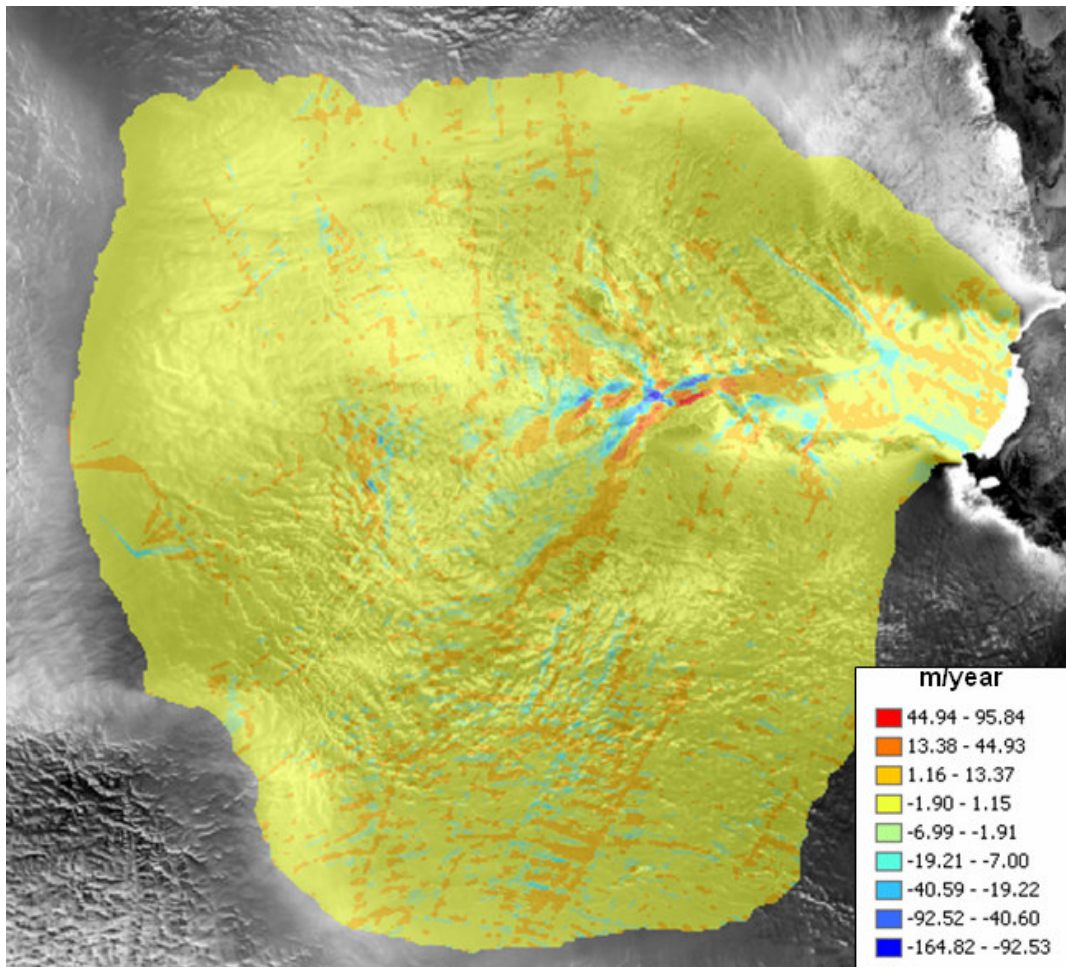
Figure 6.10 GIS based net mass balance of the Lambert Glacier – Amery Ice Shelf system draped on SAR image mosaic.

## 6.8 Result analysis

This study presents a detailed mass balance calculation for the Lambert glacier system using the most accurate data available for this area. This study calculated the mass balance for the entire Lambert Glacier – Amery Ice Shelf system. The Lambert, Fisher

and Mellor Glaciers account for 70 % of total area and 60 % of total accumulation in the Lambert Glacier – Amery Ice Shelf system.

This study utilized the flow direction from SAR interferometry which is superior in accuracy and spatial resolution whereas previous studies used DEM based basin delineation that has limitations in spatial resolution. Especially, the slight difference in flow direction in downstream results in huge difference in upstream area since the basin delineation algorithm follows the flow in a downstream to upstream direction. As a result, this study delineated smaller basin area of T-Lambert glacier compare to Rignot (2002).

The higher accuracy of surface velocities increased the reliability of the ice flux calculation. Rignot (2002) claimed that Lambert Glacier is balanced in balance since the output mass balance calculation is in the range of error. Considering the T-Lambert Glacier only, this study shows negative imbalance for the region. However the mass compensation from downstream glaciers and the increased error estimation by adding more glaciers in mass balance calculation for the Lambert Glacier – Amery Ice Shelf system makes the system is in the slightly negative imbalanced. The individual mass balance calculation shows clearer picture of the mass balance state of the Lambert Glacier – Amery Ice Shelf system. Five of eight major sub-basins are in the negative imbalance, and the remaining three show a positive imbalance. Summing up the total mass imbalance, the value of negative mass imbalance is greater than the two positive mass imbalances. Therefore, this study concludes the mass balance of the Lambert Glacier – Amery Ice Shelf system is losing the mass.

Both study deduced the high basal melting near the main grounding zone located in confluence area of Lambert, Mellor, and Fisher Glaciers. This study calculated the significant amount of basal melting contribution into the ocean with concentrated basal melting in the major grounding zone that accounts for 23.9 % of total basal melting in 2.2 % area of Amery Ice Shelf. The comparison between this study and Rignot (2002) is summarized in Table 6.6.

Table 6.6 Mass balance calculation comparison between this study and Rignot (2002).

| | Rignot (2002) | T-Lambert |
|---|---|---|
| Area ($km^2$) | 953670 | 951363 |
| Accumulation (Gt/year) | 50.45 ± 0.91 | 51.14 ± 1.26 |
| Ice Flux (Gt/year) | 52.56 ± 4.57 | 58.77 ± 2.33 |
| Mass Balance (Gt/year) | -2.1 ± 4.66 | -7.63 ± 2.65 |
| Total Basal Melting (Gt/year) | 26.6 ± 6.4 | 21.64 ± 2.17 |

Based on the results of mass balance and basal melting, ice mass contribution to sea level rise from Lambert Glacier – Amery Ice Shelf system and the glaciological interpretations can be assessed. The total ice mass contribution from the grounded ice in the system is 95.637 ± 2.89 Gt/year, which is equivalent to an increase of the global sea level by 0.24 mm/year. Although the significant amount of ice mass is discharged into the ocean, the net contribution of this glacial system to global sea level rise is negligible

considering the net mass balance of -5.094 ± 3.46 Gt/year. However, the result provides important information on global sea level ice in terms of net mass balance of Antarctica.

It has been believed that East Antarctica is accumulating the ice mass, with the West Antarctica has been the major source if the ice mass loss (Rignot and Thomas 2002). This study suggests that large portion of East Antarctica is not gaining the mass, but losing the mass. Based on the large mass loss in West Antarctica confirmed by the recent SAR interferometry study (Rignot and Thomas 2002), overall mass budget of Antarctica is believed to be negative.

The iceberg calving and basal melting of floating ice shelf could have profound influences on ocean circulation, climate and the dynamics of grounded glaciers (Rignot and Thomas 2002). The large amount of basal melting in this study (87.82 ± 3.78 Gt/year) demonstrates that basal melting rather than iceberg calving is the dominant term of mass attrition on floating ice which was speculated that the iceberg calving is the dominant term (Jacobs *et al.* 1992). Also, a large basal melting near grounding zone is computed from this study. It is caused by the temperature and salinity of seawater that comes into contact with ice in the region (Rignot and Jacobs 2002). The seawater profile of Arctic ocean shows that the temperature and salinity increase as the depth increase. The seawater is layered in the order of Ice-Ocean boundary layer and ocean mixed layer below the ice shelf (Holland and Jenkins 1999). Since the grounding zone is located at the deepest depth in seawater along the ice shelf, the bottom ice of grounding zone is experiencing the highest temperature and salinity gradient in the contact with sea water. If the ice thickness at grounding line is thick and velocity at grounding line is high, the

depth of bottom ice is increased and, therefore, the temperature and salinity gradient is enhanced (Rignot and Jacobs 2002). Considering ice thickness of 3000 ~ 4000 m in grounding zone, the seawater circulation in the bottom layer is enhanced and increases the driving stress and flow velocity. In addition to the seawater profile, the large amount of basal melting in the grounding zone is also probably caused by deeper ice draft compare to down stream ice, and it enhances the circulation of seawater caused by temperature of the water above the pressure melting point (Doake 1976, Lewis and Perkin 1986). Through the processes, the high rate of the basal melting in grounding zone is developed. This can reduce the ice shelf resistance to ice discharge, potentially causing the glacier to accelerate and the grounding zone to retreat to inland (Rignot and Jacobs 2002).

**CHAPTER VII**

**CONCLUSIONS**

This study calculated and analyzed the mass balance in detail for the entire Lambert Glacier – Amery Ice Shelf system. The analysis results have been helpful in improving our knowledge and understanding the glacial dynamic behaviors of the glacial system and its impacts on the global sea level and environment.

This research estimated that the Lambert Glacier – Amery Ice Shelf is contributing the total ice mass of 95.64 ± 2.89 Gt/year to the ocean, which is equivalent to an increase of the global sea level by 0.24 mm/year. Although the significant amount of ice mass is discharged into the ocean, the net contribution of this glacial system to global sea level rise is negligible, considering 90.54 ± 1.55 Gt/year of snow accumulation input to the system. This study concludes that the entire Lambert Glacier – Amery Ice Shelf system is overall balanced or with slight negative imbalance of -5.09 ± 3.46 Gt/year. This finding is consistent with a recent research conducted by Rignot (2002), who estimated a negative mass imbalance of -2.1 ± 4.66 $km^3$ ice $a^{-1}$ for the catchment area of the Lambert, Fisher, and Mellor glaciers.

Previously, many researchers believed that the interior of East Antarctica is accumulating the ice mass (Allison 1979, Bentley and Giovinetto 1991) and the West Antarctica is the major source of the ice mass loss of -48 ± 14 $km^3$ ice $a^{-1}$ (Rignot and Thomas 2002). However, this study suggests that large portion of East Antarctica is not gaining mass, in fact may be losing the mass. Considering the large mass loss in West

Antarctica confirmed by the recent SAR interferometry based research (Rignot and Thomas 2002), the author of this research believe that the overall mass budget in Antarctica is negative based on this research and the balanced mass balance of the other glaciers in East Antarctica from previous study (Rignot 2002). In other words, the Antarctic ice sheet as the whole is losing mass and thinning.

This study derived the most accurate, detailed mass balance budgets for the entire Lambert Glacier – Amery Ice Shelf system with the advanced remote sensing technology. For the first time, this research broke down the percentage contributions of eight major sub-glacial systems to the mass budget. It is concluded that the Lambert glacier, the Fisher Glacier and the Mellor glacier together contribute about 61 % of ice mass flux into the Amery Ice Shelf, and other five glacial systems makes the remaining 39%. Although similar research was conducted by others for the three main glaciers in the system, namely, the Lambert glacier, the Fisher glacier and Mellor glacier, this research represents the first accurate and reliable mass balance analysis for the tributary glaciers in the east and west sides of the Amery Ice Shelf. In particular, W Tributary, Charybdis and E Tributary sub-glacial systems make significant contribution to feed the Amery Ice Shelf, and each of these subglacial systems accounts for 8-13% of total ice mass influx into the Amery Ice Shelf. The complete coverage of velocity field derived from the Radarsat interferometric data is the primary reason why this research is able to fully and accurately examine the mass balance within the entire Lambert-Amery glacial system.

This study also reveals obvious regional variation in mass balance. Although the entire system is estimated to have a slight negative mass balance, three sub glacial systems, including the East Down Stream glacier, the West Down Stream glacier and the Fisher glacier, have net positive mass balance. The reason is that large parts of these glacial basins are either located near the coast with a relatively high snow accumulation rate or have relatively slow ice motion. For the five sub-glacial systems that have a negative mass balance, the imbalance magnitude also vary. The Mellor glacier and Lambert glacier have the largest negative imbalances. The total negative imbalance value of these two sub-glacier system is significantly larger than that of the entire Lambert-Amery glacial system, because part of the negative imbalance is compensated by other three sub-glacial systems with positive imbalance. In addition, GIS based net mass balance analysis shows mass balance variation within each sub-glacial system. It is common to each sub-glacial system that downstream areas have a larger magnitude of negative mass imbalance and show higher ice thinning rate, due to the increasing ice motion and decreasing snow accumulation. For those sub-glacial basins with an overall negative mass balance, considerable portions of the sub-basins show positive balance and ice thickening. The comparison of the balance velocity with the actual velocity indicates that all the glacier channels tend to have a negative balance, compared with the areas outside the edges of the main glacial channels.

The strain rate has been computed and analyzed for the entire Lambert-Amery basin. Shear margins of glacial channels and ice streams are clearly identified from the strain rate map. The range of lateral shear strain rate varies from -0.0621 to 0.0542 $a^{-1}$,

depending on the location. The computation results show that the major ice stream channels and their confluence zones are experiencing strong deformations. The strain rate variation is dominant in transverse direction, compared with the longitudinal direction of the glacial channels. The high strain rate in the shear margins has significant impacts on the internal properties of the glaciers. The strain heating within the shear margins can raise the temperature of the core of the shear margins, leading to significant horizontal temperature gradients out of the margins (Harrison *et al.* 1998). The strain rate varies along the longitudinal direction of the Amery Ice Self. Above or near the grounding zone, the velocities of the three main glaciers (the Lambert, the Mellor, and the Fisher) are increasing in the downstream direction, resulting in positive strain rate and extensive deformation. At the confluence zone and upper stretch of the ice shelf, the strain rate is positive, causing compressive deformation. This is confirmed by visually examining the SAR image and InSAR coherence image for this region. In the middle stretch of the ice shelf, not much velocity change is detected in the longitudinal direction, meaning not much longitudinal deformation. At the ice shelf front, significant negative strain rate values imply the extensive deformation. This may contribute to the development of longitudinal rifts and fractures, and hence influence iceberg calving process.

The iceberg calving and basal melting of floating ice shelf could have profound influences on ocean circulation, climate and the dynamics of tributary glaciers (Rignot and Thomas 2002). Some researchers speculated the iceberg calving is the dominant term of mass attrition on floating ice (Jacobs *et al.* 1992). The findings of this research

support an opposite view. The total basal melting is estimated to be 87.82 ± 3.78 Gt/year for the entire Amery Ice Shelf. Compared with the ice flux (16.35 ± 3.11 Gt/year) at ice shelf front, which represents the maximum amount possibly discharged by ice calving process into the ocean, the basal melting is apparent the dominant discharging process of the system. This research also suggests that the basal melting rate for the Amery Ice Shelf decreases rapidly from the grounding zone to the ice shelf front. The basal melting rate in the main grounding zone is about 20 times larger than the middle and front sections of the ice shelf. The large amount of basal melting in the grounding zone is probably caused by deeper ice draft compare to downstream ice and seawater temperature/salinity profile, and it enhances the circulation of seawater caused by temperature of the water above the pressure melting point (Doake 1976, Lewis and Perkin 1986). The basal melting has a strong influence on the stability of the ice shelf (Warner and Budd 1998, Huybrechts and deWolde 1999). Comparing the basal melting rate of the grounding line of the system to the other glaciers in East Antarctica, the basal melting rate of this system (21.64 ± 2.17 m/year) shows the similar characteristics with the neighboring glaciers showing ranges from 14 ± 4 m/year to 27 ± 7 m/year (Rignot and Jacobs 2002). The glaciers located in West Antarctica shows the similar trend of basal melting except about 30 % of the glaciers shows small amount of basal melting less than 11 m/year of basal melting at the grounding zone (Rignot and Jacobs 2002). This study confirms the characteristics of widespread rapid bottom melting in grounding zone of Antarctic ice sheet (Rignot and Jacobs 2002).

In support of the mass balance analysis and modeling, this study employed the state-of-the art remote sensing and GIS techniques. Two algorithms have been developed to enhance and improve the available software tools. One algorithm is designed to calibrate and merging velocity fields derived from individual InSAR frames. This algorithm relaxes the ground control point requirements and effectively reduces the velocity discrepancies between adjacent frames. The other algorithm is developed to compute the balance velocity. This new algorithm overcomes the limitations of the previous method in representing diagonal flux distribution for balanced flux calculation. The balance velocity field created from this method shows more consistent and reasonable pattern, compared to the real observations from the SAR interferometry technique.

To achieve accurate and reliable mass balance estimates, a great effort has been made to improve the quality of the input data and minimize the possible errors in data preparation and processing. The input velocity field derived from the Radarsat SAR interferometric data covers the entire Lambert-Amery basin with high measurement accuracy and spatial resolution. The grounding lines of the outlet glaciers are improved and updated based on the InSAR coherence image and vertical velocity field newly derived from InSAR processing. The basin boundaries of sub-glacial systems have been accurately delineated by using the ICESat Laser altimetry data and the InSAR derived ice flow direction information. Despite these improvements, the mass balance calculation in this study still has a certain level of uncertainty. The uncertainty is mainly due to our poor knowledge of the snow accumulation rate and ice thickness. The ice

thickness error explains about 60 % of the uncertainty in the mass flux calculation. The error in accumulation rate accounts for about 24 % of the uncertainty of the mass balance. To further improve the accuracy of the mass balance, the future research needs to focus on the improvements of the ice thickness and snow accumulation measurements. The repeat ICESat laser measurements promise more accurate accumulation measurements as the mission progresses (Zwally *et al.* 2002). The ice thickness data over the floating ice shelf can be enhanced by using a hydrostatic model with the ICESat laser altimeter derived surface elevation measurements (Zwally *et al.* 2002).

# REFERENCES

ALLISON, I., 1979, The mass budget of the Lambert Glacier drainage basin, Antarctica. *Journal of Glaciology*, **22**, pp. 223-235.

BENTLEY, C.R., 1987, Antarctic ice streams: a review. *Journal of Geophysical Research*, **92**, pp. 8843-8853

BENTLEY, C.R., and GIOVINETTO, M.B., 1991, Mass balance of Antarctica and sea level change. In *International Conference on the Role of Polar Regions in Global Change*, 11-15 June 1990, Geophysical Institute and Center for Global Change and Arctic System Research, University of Alaska, Fairbanks, II, Section E, pp. 481-488.

BINDCHADLER, R. (ed.) 1991, *West Antarctic Ice Sheet Initiative*. Vol II (NASA Conference Publication 3115).

BINCHADLER, R., VORNBERGER, and SHABTALE, 1993, The detailed net mass balance of the ice plain on Ice Stream B, Antarctica: a GIS approach. *Journal of Glaciology*, **133**, pp. 471-482.

BINDSCHADLER, R., and SCAMBOS, T., 1991, Satellite image derived velocity field of an Antarctic ice stream. *Science*, **252**, pp. 242-246.

BUDD, W.F., 1966, The dynamics of the Amery Ice Shelf. *Journal of Glaciology*, **6**, pp. 335-358.

BUDD, W.F., 1968, The longitudinal velocity profile of large ice masses. *Union de Geodesieand Geophysique Internationale*, 25 September – 7 October, 1967, Assemblie Generale de Berne (Berne, Switzerland).

BUDD, W.F. and ALLISON, I., 1975, An empirical scheme for estimating the dynamics of unmeasured glaciers. In *International Association of Hydrological Sciences*, Publication 104 (Symposium at Moscow 1971 – Snow and Ice in Mountainous Areas), pp. 246-256.

BUDD W.F. and CARTER D.B., 1971, An analysis of the relation between the surface and bedrock profiles of ice caps. *Journal of Glaciology*, **10**, pp. 197-209

BUDD, W.F., CORRY, M.J., and JACKA, T.H., 1982, Results from the Amery Ice Shelf Project. *Annals of Glaciology*, **3**, pp. 36-41

BUDD, W.F., COUTTS, B. and WARNER, R., 1998, Modelling the Antarctic and northern hemisphere ice-sheet changes with global climate through the glacial cycle. *Annals of Glaciology*, **27**, pp. 153-160

BUDD, W. F., JENSSEN, D. and RADOK, U. 1971, Derived Physical Characteristics of the Antarctic Ice Sheet. *ANARE Interim Reports, Ser A. Glaciology*. Publication No. 120

BUDD, W.F., and SMITH, I. N., 1985, The state of balance of the Antarctic ice sheet, glaciers, ice sheets, and sea level: effect of a 2 $CO$ -induces climatic change. Report of a Workshop held in Seattle, Washington, 13-15 September, 1984, Washington, DC, US Department of Energy, Office of Energy Research, pp. 172-177.

BUDD, W. F. and WARNER R. C., 1996, A computer scheme for rapid calculations of balance-flux distributions. *Annals of Glaciology*, **23**, pp. 21-27

CASASSA, G., and BRECHER, H.H., 1993, Relief and decay of flow stripes on Byrd Glacier. Antarctica. *Annals of Glaciology*, **17**, pp. 255-261.

COSTA-CABRAL, M.C., and STEPHEN, J.B., 1994, Digital elevation model networks (DEMON): A model of flow over hillshopes for computation of contributing and dispersal areas. *Water Resources Research*, **30**, pp. 1681-1692

DOAKE, C. S. M., 1976, Thermodynamics of the interaction between ice shelves and the sea. *Polar Rec.*, **18**, pp. 37– 41.

DREW., A.R., and WHILLANS, I.M., 1984, Measurements of surface deformation on the Greenland ice sheet by satellite tracking. *Annals of Glaciology*, **5**, pp. 51-55

FORSTER, R.R., JEZEK, K.C., SOHN, H., GRAY, A.L., and MATTER, K.E., 1998, Analysis of Glacier Flow Dynamics from Preliminary Radarsat InSAR Data of the Antarctic Mapping Mission. *BPRC Technical Report 98-02*, Byrd Polar Research Center, The Ohio State University, Columbus, Ohio

FREEEMAN, T. G., 1991, Calculating catchment area with divergent flow based on a regular grid,. *Comput. Geosci.*, **7**, pp. 413-422.

FRICKER, H.A., 1999, Applications of ERS satellite radar altimetry in the Lambert Glacier-Amery Ice Shelf system, East Antarctica. Ph.D. Dissertation, University of Tasmania, Hobart, Australia.

FRICKER, H.A., ALLISON, I., CRAVEN, M., HYLAND, G., RUDDELL, A., YOUNG, N., COLEMAN, R., KING, M., KREBS, K. and POPOV, S., 2002, Redefinition

of the Amery Ice Shelf, East Antarctica, grounding zone. *Journal of Geophysical Research*, **107**, ECV 1/1-1/9.

FRICKER, H.A., HYLAND, G., COLEMAN, R., and YOUNG, N.W., 2000, Digital Elevation Models for the Lambert Glacier - Amery Ice Shelf system, East Antarctica, from ERS-1 satellite radar altimetry. *Journal of Glaciology*, **46**, pp. 553-560

FRICKER, H.A., POPOV, S., ALLISON, I. and YOUNG, N.W., 2001, Distribution of marine ice at the base of the Amery Ice Shelf, East Antarctica, from satellite and airborne measurements. *Geophysical Research Letters*, **28**, pp. 2241-2244

FRICKER, H.A., WARNER, R., AND ALLISON, I., 2000, Mass balance of the Lambert Glacier – Amery Ice Shelf system, East Antarctica: a comparison of computed balance fluxes and measured fluxes. *Journal of Glaciology*, **46**, pp. 561-570

GIOVINETTO, M.B. AND BENTLEY, C.R., 1985, Surface balance in ice drainage systems of Antarctica. *Antarctic Journal of the U.S.*, **20**, pp. 6-13.

GIOVINETTO, M.B. and ZWALLY, H.J., 2000, Spatial distribution of net surface accumulation on the Antarctic ice sheet. *Annals of Glaciology*, **31**, pp. 171-178.

GOLDSTEIN, R.M., ENGELHARDT, H., KAMB, B., and FROLICH, R., 1993, Satellite radar interferometry for monitoring ice sheet motion: application to an Antarctic ice stream. *Science*, **262**, pp. 1525-1530.

GOLDSTEIN, R.M., ZEBKER, H.A., and WERNER, C.L., 1988, Satellite radar interferometry: two-dimensional phase unwrapping. *Radio Science*, **23**(4), pp. 713-720.

GRAY, A.L., JOUGHIN, I., TULACZYK, S., SPIKES, V. B., BINDSCHADLER, R., and JEZEK, K.C., 2005, Evidence for subglacial water transport in the West Antarctic Ice Sheet through three-dimensional satellite radar interferometry. *Geophysical Research Letter*, **32**, L03501.

GRAY, A.L., MATTER, K.E., VACHON, P.W., BINDSCHADLER, R., JEZEK, K.C., FORSTER, R., and CRAWFORD, J.P., 1998, InSAR results from the RAMP data: estimation of Glacier motion using a simple registration procedure. In *IGARSS'98*, **3**, July 1998, Seattle, WA pp. 1638-1640.

GRAY, A.L., SHORT, N., BINDCHADLER, R., JOUGHIN, I., PADMAN, L., VORNBERGER, P., and KHANANIAN, A., 2002, RADARSAT interferometry for Antarctic grounding-zone mapping. *Annals of Glaciology,* **34**, pp. 269-276.

GRAY, A.L., SHORT, N., MATTER, K.E., and JEZEK, K.C., 2001, Velocities and ice flux of the Filchner Ice Shelf and its tributaries determined from Speckle Tracking interferometry. *Canadian Journal of Remote Sensing*, **27**, pp. 193-206.

HAMBREY, M.J., and DOWDESWELL, J.A., 1994, Flow regime of the Lambert-Glacier-Amery Ice Shelf system, Antarctica: structural evidence from Landsat imagery. *Annals of Glaciology*, **20**, pp. 401-406

HARRISON, W.D., ECHELMEYER, K.A., and LARSEN, C.F., 1998, Measurement of temperature in a margin of Ice Stream B, Antarctica: implications for margin migration and lateral drag. *Journal of Glaciology*, **44**, pp. 615-724

HIGHAM, M., CRAVEN, M., RUDDELL, A., and ALLISON, I., 1997, Snow-accumulation distribution in the interior of the Lambert Glacier basin, Antarctica. *Annals of Glaciology*, **20**, pp. 43-47.

HOLLAND, D., AND JENKIN, A., 1999, Modeling thermodynamic ice-ocean interactions at the base of an ice shelf. *Journal of Physical Oceanography*, **29**, pp. 1787-1800.

HUYBRECHT, P., AND DE WOLDE, 1999, The dynamic response of the Greenland and Antarctic ice sheets to multiple-century climatic warming. *Journal of Climatology*, **12**, pp. 2169-2188.

INTERGOVERNMENTAL PANEL ON CLIMATE CHANGE, 2001, Climate change 2001; the scientific basis. (New York: Cambridge University Press) 881pp.

THE INTERNATIONAL COUNCIL FOR SCIENCE COMMITTEE ON ANTARCTIC RESEARCH, 2002, Antarctic Ice Sheet Mass Balance and Sea Level; brief report of a workshop. Scar Bulletin No. 146 (Science Committee on Antarctic Research, Annapolis, Maryland).

JACOBS, S.S., HELMER, H.H., DOAKE, C.S.M., JENKINS, A., FROLICH, R.M., 1992, Melting of ice shelves and the mass balance of Antarctica. *Journal of Glaciology*, **38**, pp. 375-387.

JEZEK, K.C., 1998, RADARSAT Antarctic Mapping Project. BPRC Technical Report No. 17, ISSN:0896-2472, BPRC, The Ohio State University, Columbus, Ohio.

JEZEK, K.C., 2002, RADARSAT-1 Antarctic Mapping Project: change detection and surface velocity campaign. *Annals of Glaciology*, **42**, pp. 564-575.

JEZEK, K.C., 2003, Observing the Antarctic Ice Sheet using the RADARSAT-1 Synthetic Aperture Radar. *Polar Geography*, **27**, pp. 197-209

JOUGHIN, I., 2002, Ice-sheet velocity mapping: a combined interferometric and speckle-tracking approach. *Annals of Glaciology*, **34**, pp. 195-201.

JOUGHIN, I.R., FAHNESTOCK, M.A. and BAMBER, J.L., 2000, Ice flow in the northeast Greenland ice stream. *Annals of Glaciology*, **31**, pp. 141 – 146.

JOUGHIN, I., GRAY, L., BINDSCHADLER, R., PRICE, S., MORSE, D., HULBE, C., MATTAR, K., and WERNER, C., 1999, Tributaries of West Antarctic Ice Streams revealed by Radardsat interferometry. *Science*, **286**, pp. 283-286.

JOUGHIN, I., KWOK, R. and FAHNESTOCK, M., 1996, Estimation of ice-sheet motion using satellite radar interferometry: method and error analysis with application to Humboldt Glacier, Greenland. *Journal of Glaciology*, **42**, pp. 564-575.

JOUGHIN, I., KWOK, R. and FAHNESTOCK, M., 1998, Interferometric estimation of three dimensional ice-flow using ascending and descending passes. *IEEE Trans. Geoscience and Remote Sensing*, **36**, pp. 25-37.

JOUGHIN, I., WINEBRENNER, D., FAHNESTOCK, M., KWOK, R. and FRABILL, W., 1996, Measurement of ice-sheet topography using satellite-radar interferometry. *Journal Glaciology*, **42**, pp. 10-22.

KWOK, R. and FAHNESTOCK, M., 1996, Ice sheet motion and topography from radar interferometry. *IEEE Transactions on Geoscience and Remote Sensing*, **34**, pp. 189-199.

LEA, N. J., 1993, An aspect-driven kinematic routing algorithm, Overland flow: hydraulics and erosion mechanics. *Parsons and Abrahams*, pp. 393-408.

LEWIS, E.L., and PERKIN, R. G., 1986, Ice pumps and their rates. *Journal of Geophysical Research*, **91**, pp. 756– 762.

LINGLE, C.S., LEE, L., ZWALLY, H.J., and SEISS, T.C., 1994, Recent elevation increase on Lambert Glacier, Antarctica, from orbit cross-over analysis of satellite-radar altimetry. *Annals of Glaciology*, **20**, pp. 26-32.

LIU, H., JEZEK, K., and LI, B., 1999, Development of Antarctic digital elevation model by integrating cartographic and remotely sensed data: A GIS-based approach. *Journal of Geophysical Research*, **104**, pp. 199-23,213.

LYTHE, M.B., VAUGHAN, D.G. and the BEDMAP CONSORTIUM., 2000, BEDMAP - bed topography of the Antarctic. 1:10,000,000 scale map. BAS (Misc) 9. Cambridge, British Antarctic Survey.

LYTHE, M.B., VAUGHAN, D.G., and BEDMAP CONSORTIUM, 2001, BEDMAP: a new ice thickness and subglacial topographic model of Antarctica. *Journal of Geophysical Research*, **106**, pp. 11335-11352.

MACAYAEAL, D.R., 1985, Optimal measurement of ice-sheet deformation from surface-marker arrays. *Journal of Glaciology*, **31**, pp. 54-59

MANSON, R., COLEMAN, R., MORGAN, P.J. and KING, M.A., 2000, Ice Velocities of the Lambert Glacier from static GPS observations. *Earth, Planets and Space*, **52**, pp. 1031-1036

McINTYRE, N.F, 1985. A re-assessment of the mass balance of the Lambert Glacier drainage basin, Antarctica. *Journal of Glaciology*, **31**, pp. 34-38.

MERCER, J., 1978, West Antarctic ice sheet and CO2 greenhouse effect: a threat to disaster. *Nature*, **271**, pp. 321-325.

MIKHAIL, E.D. and ACKERMANN, F.E., 1976, *Observations and Least-squares* (New York: Dun-Donnelley).

MIKHAIL, E.M., BETHEL, J.B., MCGLONE, J.C., 2001, *Introduction to Modern Photogrammetry,* 479p (New York: John Wiley & Sons, Inc.).

MOHR, J.J., REEH, N., AND MADSEN, S.N., 1998, Three-dimensional glacial flow and surface elevation measured with radar interferometry, *Nature*, **391**, pp. 273-276.

MORGAN, V.I. and BUDD, W.F., 1975, Radio-echo sounding of the Lambert Glacier basin. *Journal of Glaciology*, **15**, pp. 103-111.

NYE, J.F., 1952, The mechanics of glacier flow. *Journal of Glaciology*, **2**, 82-93

NYE, J.F., 1959, A method of determining the strain-rate tensor at the surface of a glacier. *Journal of Glaciology*, **3**, pp. 409-419

O'CALLAGHAN, JOHN, F., 1984, The extraction of drainage networks from digital elevation data. *Computer Vision, Graphics, and Image Processing*, **28**, pp. 323-344.

PATERSON, W.S.B., 1994. *The physics of glaciers*, Third edition, 480p. (Tarry Town, N.Y: Pergamon Press).

PATTYN, F. and DERAUW, D., 2002, Ice-dynamic conditions of Shirase Glacier, Antarctica, inferred from ERS-SAR interferometry. *Journal of Glaciology*, **48**, pp. 559-565.

PRESS, W.H., TEUKOLSKY, S.A., VETTERLING, W. T., and FLANNERY, B.P., 1992, *Numerical Recipes in C: the Art of Scientific Computing*, Second Edition (New York: Cambridge University Press).

QUINN, P., BEVEN K., CHEVALIER, P., and PALANCHON, O., 1991, The prediction of hillslope flow paths for distributed hydrological modeling using digital terrain models. *Hydrological Processes*, **5**, pp. 59-79

RADOK, U., JENSSEN, D., and McINNES, B., 1987, On the surging potential of polar ice streams, Antarctic surges – a clear and present danger?, Washington, D.C., U.S. Department of Energy (DOE/ER/60197-H1).

RIGNOT, E., 1996, Tidal motion, ice velocity and melt rate of Petermann Gletscher, Greenland, measured by SAR interferometry. *Journal of Glaciology*, **42**, pp. 476-485.

RIGNOT, E., 2002, Mass balance of East Antarctic glaciers and ice shelves from satellite data. *Annals of Glaciology*, **34**, pp. 217-227.

RIGNOT, E., GOGINENI, S., JOUGHIN, I., and KRABILL, W., 2001, Contribution to the glaciology of northern Greenland from satellite radarinterferometry. *Journal of Geophysical Research*, **106**, pp. 34,007-34,020.

RIGNOT, E., and JACOBS, S., 2002, Rapid bottom melting widespread near Antarctic ice sheet grounding lines. *Science*, **296**, pp. 2020-2023

RIGNOT, E. and THOMAS, R.H., 2002, Mass balance of polar ice sheets. *Science*, **297**, pp. 1502-1506

RITTER, D. F., KOCHEL, R.C., and J.R. MILLER, 1995, *Process Geomorphology,* 3$^{rd}$ edition. 543pp. ((Dubuque, Iowa: Wm. C. Brown Publishers)

ROBIN, G. DE Q., 1983, Coastal sites, Antarctica. Secn 4.4 In *The Climatic Record in Polar Ice Sheets*, Robin G. de Q. (ed.), 1998-100, (New York: Cambridge University Press).

ROTT, H., SKVARCA, P. and NAGLER, T., 1996, Rapid collapse of the Northern Larsen Ice Shelf, Antarctica. *Science*, **271**, pp. 788-792.

SCAMBOS, T.A., and BINDSCHADLER, R., 1993, Complex ice stream flow revealed by sequential satellite imagery. *Annals of Glaciology*, **17**, pp. 177-182.

SCAMBOS, T.A., DUTKIEWICZ, M.J., WILSON, J.C., AND BINDSCHADLER, R., 1992, Application of image cross-correlation to the measurement of glacier velocity using satellite image data. *Remote Sensing of Environment,* **42**, pp. 177-186.

SMITH, I. N. and BUDD, W. F., 1981, The derivation of past climate changes from observed changes of glaciers. In *International Association of Hydrological Science*, Publication 131 (Symposium at Canberra 1979 – Sea Level, Ice and Climatic Change), pp. 31-52.

STEPHENSON, S. N., 1984, Glacier flexure and the position of grounding lines: measurements by tiltmeter of Rutford Ice Stream, Antarctica. *Annals of Glaciology*, **5**, pp. 165–169.

SWITHINBANK, C., CHIN, T.J., WILLIAMS, R.S.J., and FERRIGNO, J. G., 1988, Anatctica. Satellite image atlas of glaceirs of the world, R. S. J. Williams and J.G. Ferrigno (eds.), (Washington, U.S. Geological Survey) 278 pp.

TABORTON, D.G. 1997, A new method for the determination of flow directions and upslope areas in grid digital elevation models. *Water Resources Research*, **33**, pp. 309-319.

TAYLOR J.R., 1997, *An Introduction to Error Analysis* (2nd edition): (Sausalito CA: University Science Books) 327 p.

THOMAS, R.H., MACAYEAL, D.R., EILERS, D.H., and GAYLORD, D.R., 1984, Glaciological studies on the Ross Ice Shelf, Antarctica, 1972-1978. *The Ross Ice Shelf: Glaciology and Geophysics Antarctic Research Series*, **42**, pp. 21-53, AGU.

VAUGHAN, D.G., BAMBER, J.L., GIOVINETTO, M., RUSSELL, J., COOPER, A.P., 1999, Reassessment of net surface mass balance in Antarctica. *Journal of Climate*, **12**, pp. 933-946.

WARNER, R. C., and BUDD, W. F., 1998, Modelling the long term response of the Antarctic ice sheet to global warming. *Annals of Glaciology*, **27**, pp. 161– 168.

WEERTMAN, J., 1974, Stability of the junction of an ice sheet and an ice shelf. *Journal of Glaciology*, **13**, pp. 3-11.

WINGHAM D.J., RIDOUT, A.J., SCHARROO, R., ARTHERN, R.J., SHUN, C.K., 1998, Antarctic elevation change from 1992 to 1996. *Science*, **282**, pp. 456-458.

WONG, A.P., BINDOFF, N.L., FORBES, 1998, Ocean-ice shelf interaction and possible bottom water formation in Prydz Bay, Antarctica. *Antarctic Research Series - Ocean, Ice and Atmosphere: Interactions at the Antarctic Continental Margin*, **75,** pp. 173-187

YOUNG, N. and HYLAND, G., 2002, Velocity and strain rates derived from InSAR analysis over the Amery Ice Shelf, East Antarctica. *Annals of Glaciology*, **34**, pp. 228-234.

ZHAO, Z., 2001, Surface velocities of the East Antarctic Ice Streams from Radarsat-1 interferometric Synthetic Aperture Radar Data. Ph.D. Dissertation, The Ohio State University, Columbus, Ohio.

ZUMBERGE, J.H., GIOVINETTO, M., KEHLE, R., and REID, J., 1960, Deformation of the Ross Ice Shelf near the Bay of Whales, Antarctica. *Glaciological Report Series* (New York), No. 3.

ZWALLY, H.J., SCHUTZ, B., ABDALATI, W., ABSHIRE, J., BENTLEY, C., BRENNER, A., BUFTON, J., DEZIO, J., HANCOCK, D.,HARDING, D., HERRING, T., MINSTER, B., QUINN, K., PALM, S., SPINHIRNE, J., THOMAS, R., 2002, ICESats laser measurements of polar ice, atmosphere, ocean. *Journal of Geodynamics*, **34**, pp. 405–445.

ZWALLY, H.J., SCHUTZ, R., BENTLEY, C., BUFTON, J., HERRING, T., MINSTER, J., SPINHIRNE, J., and THOMAS, R., 2003, *GLAS/ICESat L2 Antarctic and Greenland Ice Sheet Altimetry Data V001*. Boulder, CO: National Snow and Ice Data Center. Digital media.

**VITA**

Name:            Jaehyung Yu

Address:         Department of Geosciences, Texas A&M University – Kingsville
                 Kingsville, TX 78363

Email Address:   jaehyungyu@hotmail.com

Education:       Ph.D., Geography, Texas A&M University, College Station, 2005

                 M.S., Geology, Chungnam National University, S. Korea, 1999

                 B.S., Geology, Chungnam National University, S. Korea, 1997

Experience:      2005-  Assistant Professor
                     Department of Geosciences, Texas A&M University - Kingsville

                 2001-2005, Research Assistant
                     Knowledge Engineering Laboratory, Texas A&M University

                 2002, Research Assistant
                     Department of Geography, Texas A&M University

                 2003, Research Assistant
                     Department of Geography, Texas A&M University

                 2000-2001, Teaching Assistant
                     Department of Geology, Texas A&M University